CONTRACTOR REPORT

SAND90—7008
Unlimited Release
UC—721

Mineralogy of the Culebra Dolomite Member of the Rustler Formation

Terry Sewards, Michael L. Williams, Klaus Keil
Department of Geology and Institute of Meteoritics
University of New Mexico
Albuquerque, NM 87131

Prepared by Sandia National Laboratories Albuquerque, New Mexico 87185 and Livermore, California 94550 for the United States Department of Energy under Contract DE-AC04-76DP00789

Printed March 1991

Issued by Sandia National Laboratories, operated for the United States Department of Energy by Sandia Corporation.

Available to DOE and DOE contractors from
Office of Scientific and Technical Information
PO Box 62
Oak Ridge, TN 37831

Prices available from (615) 576-8401, FTS 626-8401

Available to the public from
National Technical Information Service
US Department of Commerce
5285 Port Royal Rd
Springfield, VA 22161

NTIS price codes
Printed copy: A07
Microfiche copy: A01

SAND--90-7008

SAND90-7008
Unlimited Release
Printed March 1991

DE91 014327

MINERALOGY OF THE CULEBRA DOLOMITE MEMBER OF THE RUSTLER FORMATION*

Terry Sewards, Michael L. Williams, and Klaus Keil

Department of Geology and Institute of Meteoritics,
University of New Mexico, Albuquerque, NM 87131

ABSTRACT

This report characterizes the mineralogy of the Culebra Member of the Rustler Formation based on studies of samples from cores of eight boreholes surrounding the WIPP repository. This investigation had three main goals: (1) to obtain accurate modal compositions of all the samples selected; (2) to investigate both the lateral and vertical variation of the mineralogy of the Culebra unit; and, (3) to characterize water-bearing fracture surfaces in particular detail.

The Culebra Dolomite member of the Rustler Formation is mineralogically and texturally heterogeneous, both vertically and horizontally. Although the predominant mineral is dolomite, important constituents of the formation are clay, quartz, gypsum, and calcite. Trace minerals include halite, phyllosilicates of metamorphic origin, feldspar, and pyrite.

The origin of the dolomite is presumed to be the result of early stage dolomitization of chemically sedimented calcite, which was deposited in shallow waters; algal mats probably formed what is now interstitial organic matter, which is mixed with clay. The dolomite content of the samples averages 80%.

Clay is the second most abundant mineral present and is concentrated along textural features, particularly the surfaces of fractures and vugs, thus making its presence of particular import to the characterization of hydrological transport within the formation. Clay abundances range from less than 1.0% to nearly 60% of the bulk samples.

The clay mineral assemblage includes corrensite (ordered mixed-layer chlorite/smectite), illite, serpentine, and chlorite. Corrensite is the dominant clay mineral, usually constituting about 50% of the clay assemblage;

*The work described in this report was performed for Sandia National Laboratories under Contract No. 01-6328.

illite is the next most abundant constituent, and serpentine and chlorite are relatively minor components. Because of its high cation exchange capacity (CEC), the presence of corrensite is of particular importance as it can be an effective sorbent of radionuclides.

Gypsum is present largely as a vein and vug filling cement; it is probably almost entirely of secondary origin.

Calcite is only present in measurable quantities in the WIPP-29 core, where it is a major component of the top part of the core. It is interpreted to be of secondary origin, produced by dedolomitization of dolomite by calcium-rich waters of meteoric origin.

ACKNOWLEDGMENT

Dr. D. G. Brookins of the University of New Mexico reviewed this report and provided invaluable assistance in preparing materials used in the text, figures, and tables.

The authors also acknowledge the contributions made by several scientists from Sandia National Laboratories. C. L. Stein provided guidance in the initial stages of this work and assisted the authors in the collection of the samples examined in this report. The detailed critical reviews of early versions of this manuscript by S. J. Lambert and K. L. Robinson led to significant improvements in the report. Additional reviews by J. Krumhansl were also helpful. M. D. Siegel was responsible for the preparation of final draft of the report and coordinated technical and management reviews.

CONTENTS

FIGURES

TABLES

I. INTRODUCTION

This report characterizes the mineralogy of the Culebra Member of the Rustler Formation based on studies of samples from cores of eight boreholes surrounding the Waste Isolation Pilot Plant (WIPP) repository. The Culebra Dolomite is characterized by a high fracture porosity (Ferrall and Gibbons, 1979) and is considered to be the most probable conduit of radionuclides to the accessible environment in the event of a low-pressure breach in the repository. This investigation had three main goals: (1) to obtain accurate modal composites of all the samples selected; (2) to investigate both the lateral and vertical variation of the mineralogy of the Culebra unit; and, (3) to characterize water-bearing fracture surfaces in particular detail.

Instrumental methods used include x-ray diffraction (XRD) analysis, x-ray fluorescence (XRF) spectroscopic analysis, electron microprobe elemental (EMX) analysis, analytical electron microscopy (AEM) and optical microscopy.

II. SITE GEOLOGY

The WIPP site is situated about 25 miles east of Carlsbad (Figure II-1) in southeastern New Mexico. It lies in the northern part of the Delaware Basin, which is ringed by the Capitan Limestone Reef Complex. The Upper Permian (Ochoan) Rustler Formation is a sequence of evaporite and clastic rock units overlying the Salado Formation (Figure II-2), which is composed mainly of thick halite beds into which the WIPP repository has been excavated.

The Rustler Formation is composed of five major members (Figure II-3): the Lower Member, which consists mainly of mud/siltstones and beds of halite and anhydrite; the Culebra Dolomite; the Tamarisk Member (anhydrite, gypsum, and mud/siltstones); the Magenta Dolomite, and the Forty-niner Member, which is predominantly anhydrite and gypsum. The Culebra Dolomite appears to be an aquifer with fracture permeability providing the dominant flow mechanism (Ferrall and Gibbons, 1979).

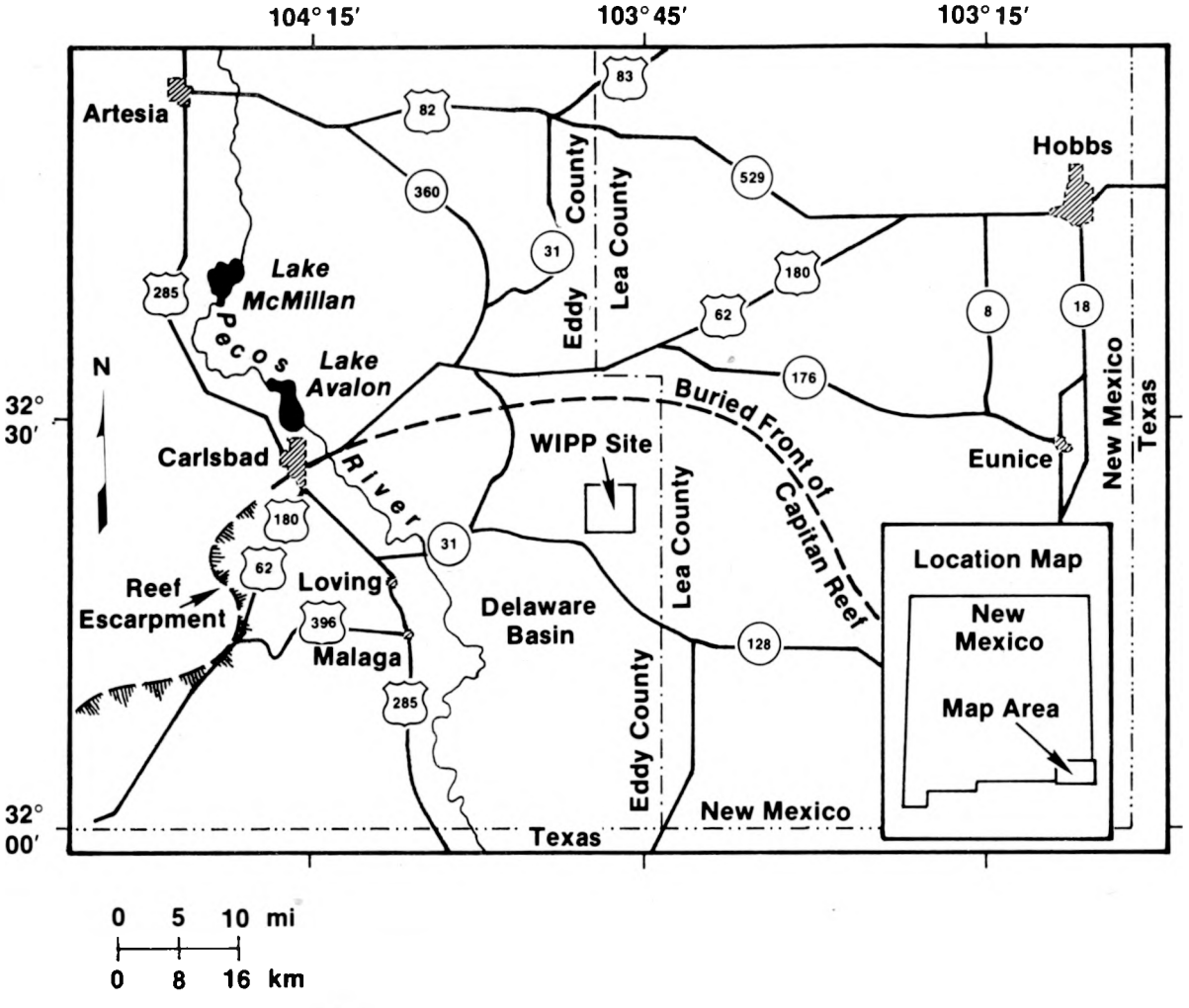

TRI-6342-528-0

Figure II-1. Regional Setting, Northern Delaware Basin, Southeastern New Mexico.

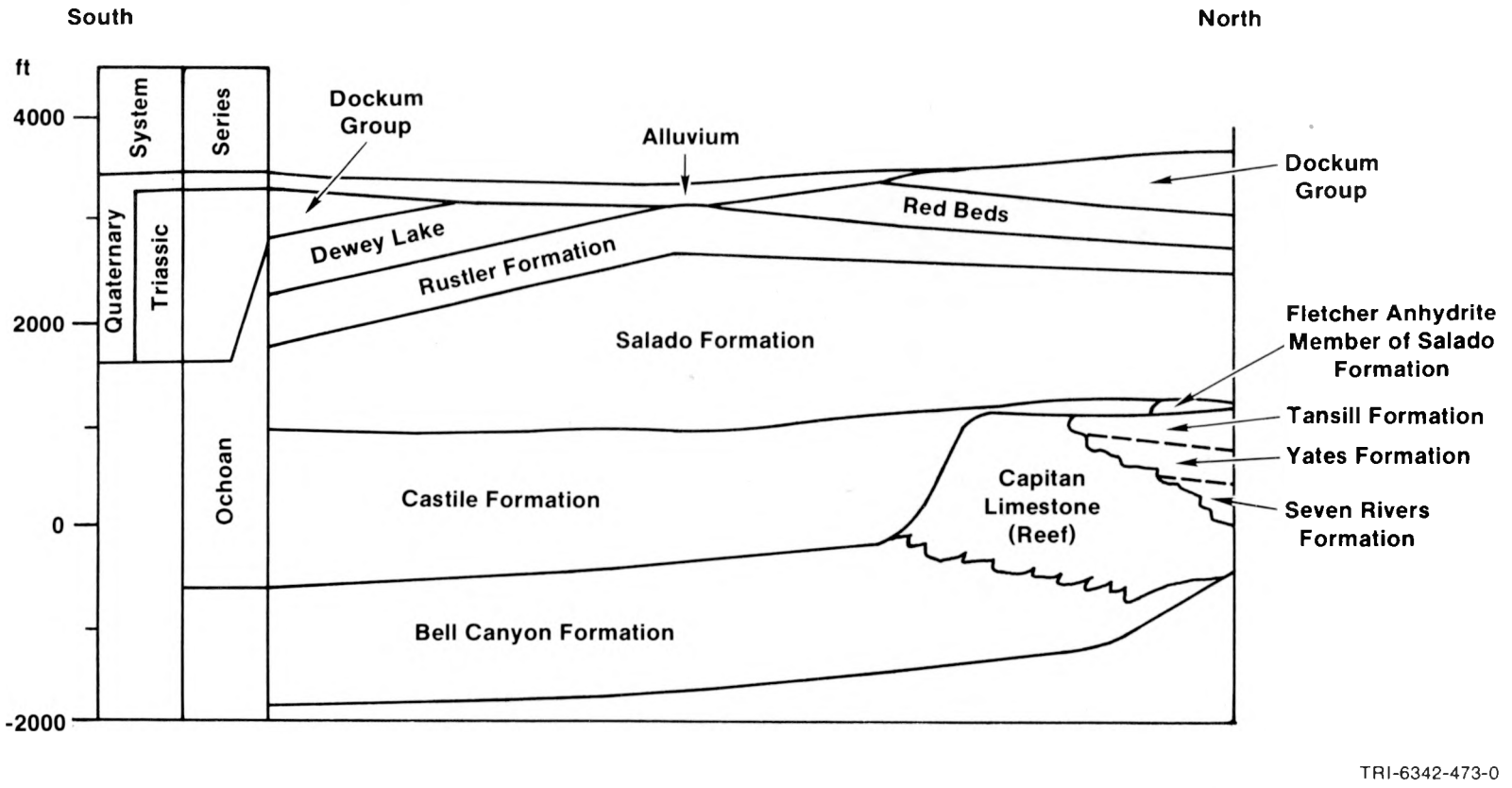

Figure II-2. Generalized North-South Cross Section, Delaware Basin, Southeastern New Mexico.

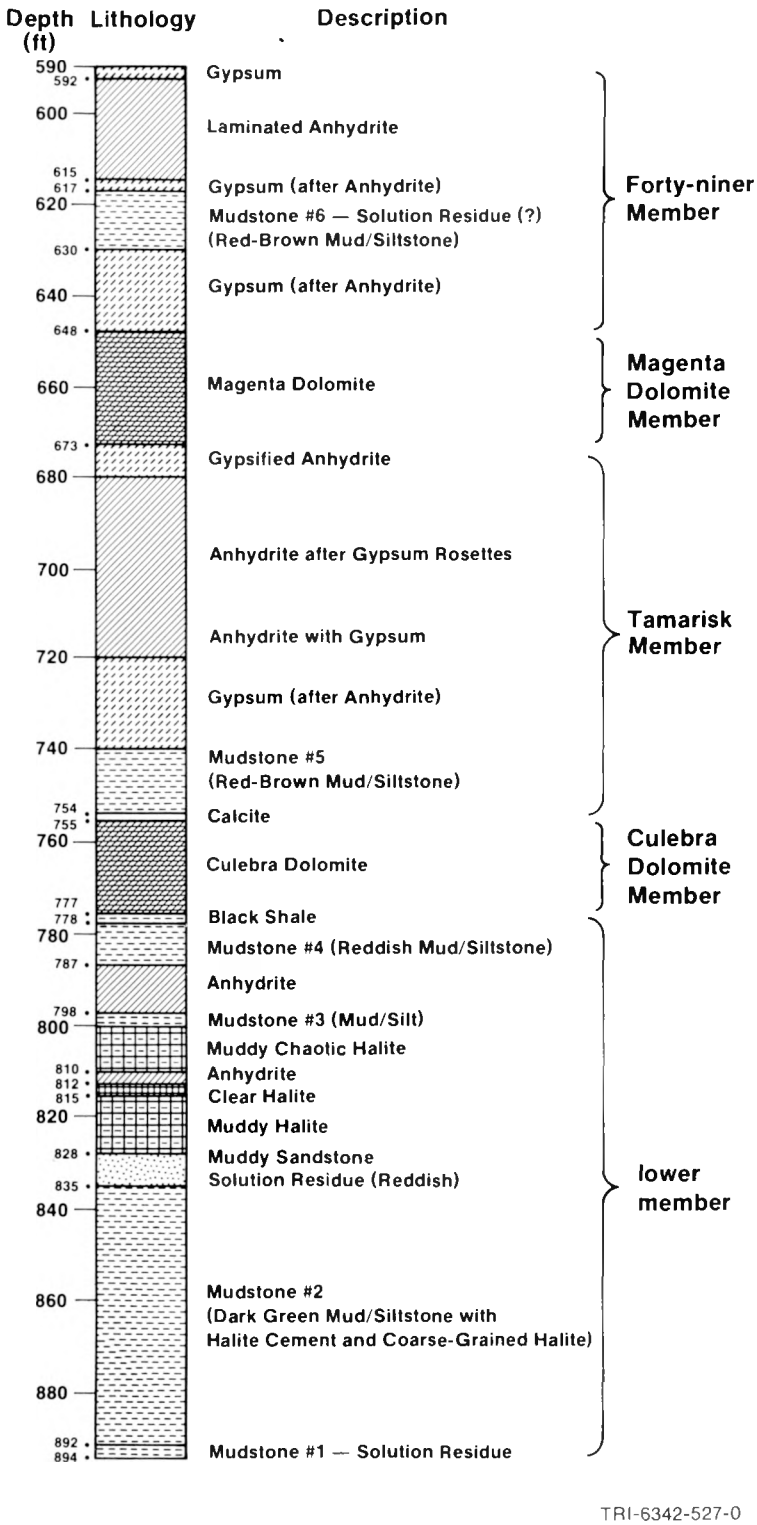

Figure II-3. Lithologic Log of the WIPP-19 Core, Rustler Formation.

III. SAMPLE CHARACTERIZATION

Core Locations and Sample Depths

Rock samples used in this study were taken from cores of eight different boreholes in the vicinity of the WIPP site: H-6B, H-7C, H-10B, H-11, WIPP-12, WIPP-25, WIPP-26, and WIPP-29 (Figure III-1). Sample depths for each core are shown in Table III-1, which also includes the upper and lower depths of the Culebra Formation and the altitude at the top of the core, included for reference.

Core samples for this study consisted of 116 portions of the eight cores mentioned above. Sample length ranged from 3 to 8 cm and were either 1/4, 1/3, 1/2, or 2/3 sections of the core. Core diameters were either 3" or 4".

Selection Criteria

Samples were chosen by visual inspection to provide three different types of information. First, maximum coverage of the Culebra section was attempted; in some cases, however, cores were incomplete, allowing only partial coverage of the dolomite unit. Second, lithologic boundaries such as contacts between dolomite and mudstone, dolomite and gypsum, etc. were sampled. Third, textural features, such as fractures, vugs, and clay seams were sampled in order to allow analysis of potential water-bearing surfaces.

Table III-1. Core Sample Depths

H6B Core Altitude: 3350' Culebra: Top: 604' Bottom: 627'		H7C Core Altitude: 3175' Culebra: Top: 237' Bottom: 273.5'		H10B Core Altitude: 3650' Culebra: Top: 1360' Bottom: 1387'		H11 Core Altitude: 3410' Culebra: Top: 731' Bottom: 760'	
Sample ID	Mean Depth	Sample ID	Mean Depth	Sample ID	Mean Depth	Sample ID	Mean Depth
H6B-1	614	H7C-1	237.10	H10B-1	1370.30	H11-1	731.00
H6B-2	616	H7C-2	238.30	H10B-2	1372.30	H11-2	732.50
H6B-3	631	H7C-3	242.55	H10B-3	1373.20	H11-3	736.00
H6B-4	637	H7C-4	252.50	H10B-4	1374.40	H11-4	736.50
H6B-5a	640	H7C-5	253.10	H10B-5	1375.60	H11-5	737.50
H6B-5b	640	H7C-6	254.60	H10B-6	1379.40		
		H7C-7	256.00	H10B-7	1381.25		
		H7C-8	260.15	H10B-8	1381.95		
		H7C-9	264.70	H10B-9	1383.25		
		H7C-10	266.70	H10B-10	1385.90		
		H7C-11	268.00	H10B-11	1388.90		
		H7C-12	271.60	H10B-12	1389.40		
		H7C-13	273.10	H10B-13	1392.80		
				H10B-14	1395.25		
				H10B-15	1396.25		
				H10B-16	1397.25		
				H10B-17	1398.20		
				H10B-18	1398.95		

Table III-1. Core Sample Depths (Continued)

WIPP-12 Core Altitude: 3475' Culebra: Top: 822' Bottom: 846.8'		WIPP-25 Core Altitude: 3200' Culebra: Top: 447' Bottom: 472'		WIPP-26 Core Altitude: 3140' Culebra: Top: 186' Bottom: 209'		WIPP-29 Core Altitude: 2965' Culebra: Top: 12' Bottom: 42'	
Sample ID	Mean Depth	Sample ID	Mean Depth	Sample ID	Mean Depth	Sample ID	Mean Depth
W12-1	828.40	W25-1	446.90	W26-1	188.00	W29-1	8.5
W12-2	830.50	W25-2	447.30	W26-2	188.70	W29-2	9.7
W12-3	831.40	W25-3	447.40	W26-3	189.90	W29-3	13.0
W12-4	832.00	W25-4	450.00	W26-4	190.95	W29-4	13.5
W12-5	833.70	W25-5	450.50	W26-5	192.40	W29-5	18.1
W12-6	834.50	W25-6	451.50	W26-6	193.20	W29-6	19.25
W12-7	835.10	W25-7	452.00	W26-7	194.50	W29-7	20.20
W12-8	836.20	W25-8	453.95	W26-8	198.00	W29-8	21.55
W12-9	836.70	W25-9	456.00			W29-9	22.40
W12-10	837.00	W25-10	459.00			W29-10	23.55
W12-11	837.70	W25-11	462.00			W29-11	24.50
W12-12	838.60	W25-12	470.00			W29-12	26.00
W12-13	839.30	W25-13	473.10			W29-13	27.50
W12-14	839.80	W25-14	473.95			W29-14	29.30
W12-15	840.60	W25-15	475.40			W29-15	31.15
W12-16	842.20	W25-16	477.20			W29-16	32.00
W12-17	842.40	W25-17	478.50			W29-17	32.55
		W25-18	479.90			W29-18	43.60
		W25-19	483.40				
		W25-20	483.90				
		W25-21	485.95				
		W25-22	490.60				

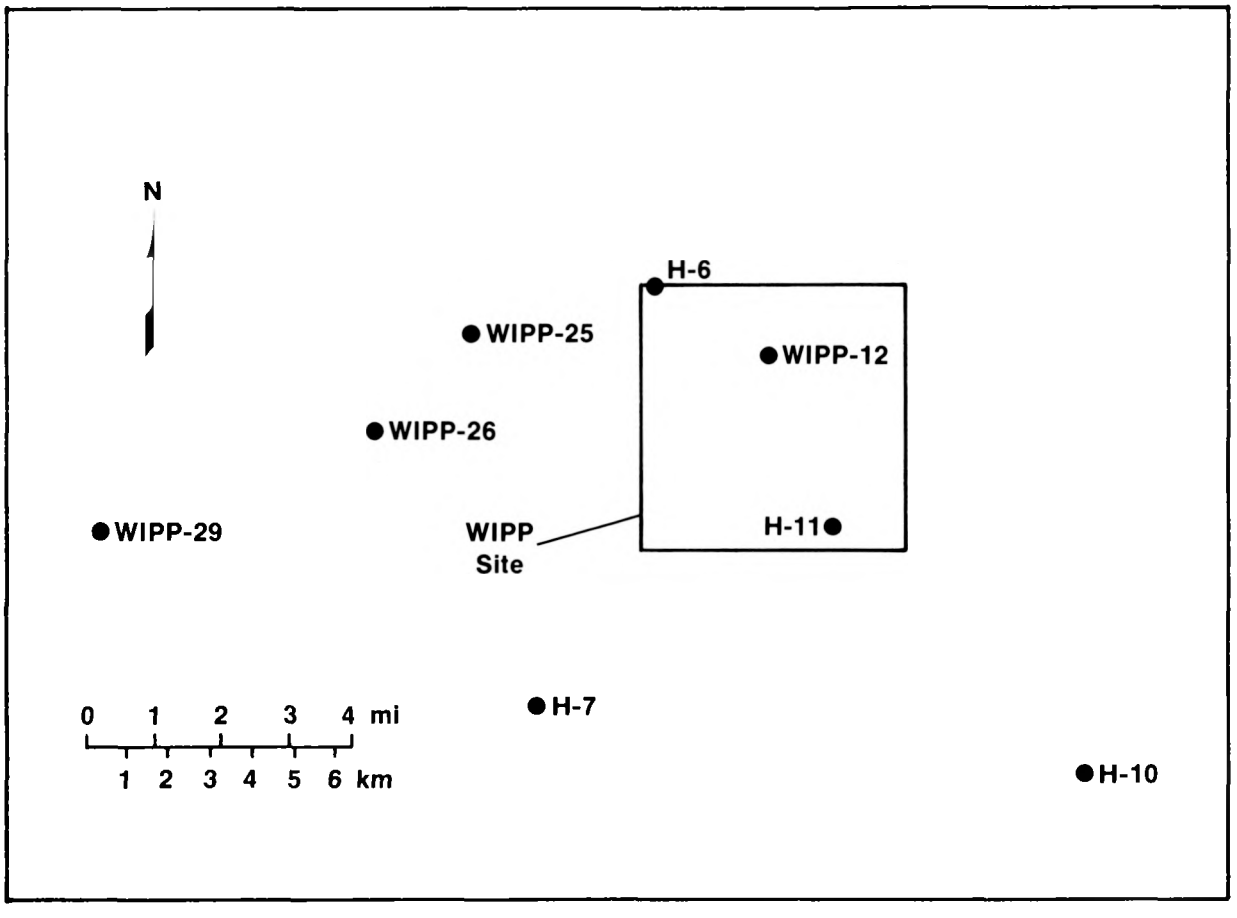

TRI-6342-587-0

Figure III-1. Core Locations

IV. WHOLE ROCK COMPOSITIONAL DATA

Of the 106 samples, XRF was performed on 101 samples for 8 constituent oxides: SiO_2, Al_2O_3, CaO, MgO, FeO, Na_2O, K_2O, and SO_3. Appendix A includes a detailed description of the analytical methods used. The complete set of compositional data is listed in Tables IV-1 through IV-7.

Table IV-1. H6B Core XRF Compositional Data

Sample ID	Depth	SiO_2	Al_2O_3	CaO	MgO	FeO	Na_2O	K_2O	SO_3	Total
H6B-1	614.00	6.74	1.36	23.44	17.34	0.39	0.09	0.60	0.16	50.12
H6B-2	616.00	5.12	0.99	27.14	18.05	0.35	0.09	0.44	0.14	52.33
H6B-3	631.00	51.03	12.58	2.09	19.21	0.68	0.93	1.19	0.00	87.71
H6B-4	637.00	4.30	0.74	27.90	16.19	0.31	0.06	0.25	0.19	49.95
H6B-5a	639.00	2.51	0.41	22.93	1.48	0.14	0.04	0.01	n.a.	27.51
H6B-5b	640.00	9.48	1.58	20.79	6.13	0.29	0.06	0.13	n.a.	38.47

Table IV-2. H7C Core XRF Compositional Data

Sample ID	Depth	SiO_2	Al_2O_3	CaO	FeO	Na_2O	MgO	SO_3	Total
H7C-1	237.10	0.25	0.05	26.99	0.16	0.07	9.79	12.62	49.95
H7C-2	238.30	0.50	0.10	28.91	0.18	0.08	15.27	0.23	45.27
H7C-3	242.55	0.41	0.09	28.96	0.21	0.07	15.92	0.07	45.73
H7C-4	252.50	0.26	0.06	28.60	0.18	0.05	16.05	0.12	45.31
H7C-5	253.10	0.90	0.17	28.43	0.22	0.08	14.52	0.12	44.43
H7C-6	254.60	2.36	0.49	28.14	0.24	0.06	16.17	0.08	47.54
H7C-7	256.00	2.37	0.49	27.96	0.23	0.05	16.19	0.07	47.37
H7C-8	260.15	2.85	0.59	28.35	0.24	0.05	18.26	0.08	50.41
H7C-9	264.70	6.43	1.33	25.93	0.43	0.06	15.67	0.07	49.92
H7C-10	266.70	4.40	0.87	26.99	0.34	0.06	15.53	0.07	48.25
H7C-11	268.00	2.82	0.51	27.87	0.29	0.02	14.78	0.06	46.36
H7C-12	271.60	2.61	0.52	27.85	0.26	0.02	14.91	0.05	46.23
H7C-13	273.10	1.54	0.31	28.35	0.22	0.00	13.77	0.08	44.27

Table IV-3. H10B Core XRF Compositional Data

Sample ID	Depth	SiO_2	Al_2O_3	CaO	MgO	FeO	Na_2O	SO_3	Total	
H10-1	1370.30	9.38	1.92	22.29	13.57	0.54	0.19	0.94	6.73	55.55
H10-2	1372.30	2.23	0.40	26.91	15.77	0.27	0.28	0.22	0.40	46.48
H10-3	1373.20	0.75	0.16	27.95	15.72	0.20	0.22	0.08	2.66	47.73
H10-4	1374.40	1.60	0.29	27.31	15.30	0.30	0.15	0.18	1.87	47.00
H10-5	1375.60	1.39	0.27	27.80	17.29	0.23	0.23	0.12	0.21	47.54
H10-6	1379.40	2.40	0.47	27.53	17.85	0.24	0.15	0.20	0.18	49.02
H10-7	1381.25	2.64	0.52	26.22	13.09	0.21	0.09	0.22	10.33	53.31
H10-8	1381.95	4.65	0.99	25.79	15.90	0.31	0.20	0.42	2.92	51.18
H10-9	1383.25	1.73	0.34	27.73	15.95	0.22	0.13	0.13	3.29	49.52
H10-10	1385.90	2.46	0.47	27.52	16.48	0.25	0.14	0.17	2.94	50.42
H10-11	1388.90	2.11	0.38	27.90	18.00	0.23	0.15	0.16	2.01	50.95
H10-12	1389.40	1.89	0.32	27.45	16.67	0.25	0.12	0.14	1.59	48.44
H10-13	1392.80	1.18	0.22	28.17	16.20	0.22	0.13	0.07	3.85	50.04
H10-14	1395.25	1.28	0.21	27.95	15.84	0.21	0.10	0.06	4.98	50.62
H10-15	1396.25	1.71	0.29	26.37	12.53	0.20	0.12	0.07	11.25	52.55
H10-16	1397.25	9.86	1.90	22.52	16.94	0.49	0.28	0.61	1.79	54.38
H10-17	1398.20	2.13	0.36	27.16	14.59	0.22	0.11	0.10	7.14	51.80

Table IV-4. H11 Core XRF Compositional Data

Sample ID	Depth	SiO_2	Al_2O_3	CaO	MgO	FeO	Na_2O	K_2O	SO_3	Total
H11-1	731.00	5.46	1.03	25.50	19.24	0.37	0.55	0.39	3.75	56.29
H11-2	732.50	2.88	0.53	27.48	20.27	0.27	0.38	0.24	0.77	52.81
H11-3	736.00	4.33	0.86	26.25	19.48	0.31	0.61	0.28	1.23	53.34
H11-4	736.50	3.97	0.75	27.20	20.43	0.28	0.28	0.29	1.21	54.41
H11-5	737.50	5.91	1.16	26.28	20.48	0.35	0.28	0.44	0.34	55.24
W12-1	828.40	4.72	0.90	27.80	20.87	0.30	0.00	0.36	0.17	55.1211
W12-2	830.50	3.89	0.72	28.22	20.82	0.23	0.09	0.25	0.00	54.2247
W12-3	831.40	1.93	0.31	29.41	22.27	0.24	0.01	0.10	0.82	55.0872
W12-4	832.00	1.65	0.29	29.22	22.62	0.24	0.13	0.10	0.25	54.5020
W12-5	833.70	1.72	0.29	28.77	20.03	0.24	0.01	0.10	6.04	57.2006
W12-6	834.50	1.65	0.28	29.14	21.45	0.22	0.00	0.10	1.88	54.7179
W12-7	835.10	1.44	0.23	29.14	20.97	0.22	0.00	0.08	1.84	53.9293
W12-8	836.20	1.55	0.26	29.39	21.08	0.22	0.10	0.09	3.30	55.9728
W12-9	836.70	1.34	0.21	29.32	21.32	0.22	0.10	0.07	2.35	54.9349
W12-10a	837.00	1.29	0.22	29.31	20.93	0.21	0.07	0.07	2.73	54.8401
W12-10b	837.20	1.10	0.17	29.28	20.97	0.21	0.07	0.07	3.11	54.9683
W12-11	837.70	2.22	0.38	28.89	22.13	0.25	0.15	0.15	0.39	54.5495
W12-12	838.60	1.62	0.27	29.27	21.20	0.26	0.13	0.10	0.38	53.2253
W12-13	839.30	1.33	0.22	29.07	20.97	0.26	0.14	0.08	0.96	53.0177
W12-14	839.80	1.35	0.23	29.16	20.97	0.25	0.12	0.09	0.53	52.6965
W12-15	840.60	1.99	0.36	28.69	22.18	0.26	0.15	0.16	0.73	54.5264
W12-16	842.20	16.10	3.23	19.74	21.90	0.87	0.28	0.94	0.40	63.4461
W12-17	842.40	2.30	0.42	28.52	21.95	0.27	0.15	0.17	0.56	54.3515

Table IV-5. WIPP-25 XRF Compositional Data

Sample ID	Depth	SiO_2	Al_2O_3	CaO	MgO	FeO	Na_2O	K_2O	SO_3	Total
W25-1	446.90	21.44	2.74	19.00	13.11	0.89	3.89	1.03	1.79	63.89
W25-2	447.30	3.17	0.52	27.21	17.26	0.23	0.15	0.29	0.15	48.97
W25-3	447.40	48.79	8.80	6.60	6.51	2.05	1.66	4.60	1.41	80.41
W25-4	450.00	5.45	1.04	25.85	17.38	0.31	0.14	0.55	0.11	50.84
W25-5	450.50	4.24	0.80	26.33	17.04	0.26	0.22	0.40	0.19	49.48
W25-6	451.50	5.71	1.08	26.03	18.32	0.33	0.08	0.56	0.15	52.25
W25-7	452.00	5.66	1.07	25.94	17.74	0.32	0.09	0.56	0.09	51.47
W25-8	453.95	5.89	1.12	26.28	17.46	0.36	0.11	0.54	0.10	51.85
W25-9	456.00	4.08	0.78	25.09	15.67	0.27	0.69	0.29	0.15	47.01
W25-10	459.00	2.64	0.49	27.20	16.42	0.24	0.29	0.18	0.11	47.56
W25-11	462.00	2.22	0.41	27.68	17.96	0.32	0.16	0.13	0.09	48.97
W25-12	470.00	1.63	0.29	28.00	17.50	0.25	0.19	0.10	0.08	48.04
W25-13	473.10	49.06	9.82	0.88	11.26	2.06	1.10	2.38	0.21	76.76
W25-14	473.95	48.07	8.78	1.90	9.77	3.23	0.85	1.95	3.31	77.85
W25-19	483.40	0.15	0.03	29.11	0.13	0.10	0.03	0.00	38.56	68.10
W25-20	483.90	0.88	0.09	30.25	0.46	0.11	0.05	0.00	35.47	67.30
W25-21	485.95	0.24	0.05	29.39	0.16	0.10	0.03	0.00	38.87	68.84
W25-22	490.60	1.49	0.32	29.16	0.83	0.16	0.04	0.02	36.38	68.39

Table IV-6. WIPP-26 XRF Compositional Data

Sample ID	Depth	SiO_2	Al_2O_3	CaO	MgO	FeO	Na_2O	K_2O	SO_3	Total
W26-1	188.00	5.80	1.12	25.80	14.69	0.59	0.14	0.64	0.06	48.86
W26-2	188.70	4.67	0.91	26.85	15.63	0.36	0.09	0.43	0.07	49.02
W26-3	189.90	7.57	1.50	25.14	0.02	0.54	0.08	0.74	0.11	35.70
W26-4	190.95	4.93	0.95	26.82	15.64	0.38	0.06	0.44	0.06	49.28
W26-5	192.40	7.97	1.62	25.05	15.20	0.58	0.08	0.73	0.07	51.31
W26-6	193.20	6.64	1.21	25.91	15.29	0.43	0.12	0.51	0.04	50.16
W26-7	194.50	2.71	0.47	27.81	16.48	0.31	0.11	0.21	0.05	48.16
W26-8	198.00	0.96	0.17	28.75	17.56	0.25	0.12	0.06	0.04	47.90

Table IV-7. WIPP-29 XRF Compositional Data

Sample ID	Depth	SiO_2	Al_2O_3	CaO	FeO	Na_2O	K_2O	MgO	SO_3	Total
W29-1	8.50	1.03	0.17	33.78	0.17	0.08	0.08	12.32	0.16	47.79
W29-2	9.70	1.76	0.32	29.71	0.20	0.09	0.17	17.10	0.09	49.44
W29-3	13.00	0.64	0.12	32.86	0.15	0.15	0.08	12.93	0.14	47.08
W29-4	13.50	1.28	0.24	35.44	0.17	0.18	0.15	11.51	0.30	49.28
W29-5	18.10	2.28	0.42	28.00	0.21	0.23	0.31	17.43	0.12	49.00
W29-6	19.25	2.52	0.47	36.52	0.20	0.09	0.34	7.90	0.12	48.16
W29-7	20.20	3.36	0.60	29.98	0.24	0.13	0.37	14.67	0.10	49.45
W29-8	21.55	4.62	0.93	26.66	0.38	0.10	0.52	17.98	0.04	51.23
W29-9	22.40	5.28	1.05	26.40	0.52	0.12	0.61	16.99	0.12	51.08
W29-10	23.55	8.41	1.62	23.70	0.55	0.26	0.90	16.50	0.17	52.11
W29-11	24.50	4.31	0.80	26.76	0.37	0.13	0.45	18.02	0.06	50.91
W29-12	26.00	2.76	0.53	27.66	0.27	0.12	0.31	17.53	0.07	49.26
W29-13	27.50	3.88	0.70	27.07	0.29	0.18	0.42	17.26	0.26	50.06
W29-14	29.30	2.34	0.28	27.41	0.25	0.19	0.34	17.50	0.14	48.45
W29-15	31.15	1.50	0.28	27.89	0.20	0.22	0.26	17.54	0.13	48.02
W29-16	32.00	3.50	0.63	26.36	0.35	0.21	0.45	18.23	0.17	49.91
W29-17	32.55	1.95	0.35	27.70	0.26	0.20	0.25	17.79	0.11	48.61

V. WHOLE ROCK MINERALOGICAL DATA

X-Ray Diffraction Analysis

Whole rock aliquots of the 106 samples used in this study were analyzed by XRD. Analytical methods are described in Appendix A. Minerals identified are dolomite, calcite, gypsum, anhydrite, halite, quartz, and clay. The results of these analyses are listed in Tables V-1 through V-8. Figures V-1 through V-4 show typical diffractograms from selected samples, illustrating the presence of dolomite, calcite, gypsum, halite, quartz, and clay. Figure V-1 for sample WIPP-12 #4 is a very typical diffractogram: the sample contains dolomite and quartz, the presence of traces of clay is inferred from XRF, and petrographic data. All samples containing quartz also contain clay. Figure V-2 for sample WIPP-25 #1 shows the presence of dolomite, halite, gypsum, quartz, and clay; in this sample, the clay peaks are discernible, particularly a broad peak at d=4.526A. XRD for clay rich sample WIPP-12 #16 (Figure V-3) also shows the presence of dolomite, halite, and quartz, but in this case the clay peaks for corrensite, illite, and serpentine are clearly discernible. Finally, the XRD pattern for sample WIPP-29 #1 (Figure V-4) indicates the presence of calcite in addition to dolomite and quartz.

Quantitative Mineralogical Analysis

Mineral modes for the 101 samples, which were analyzed by XRF spectroscopy for the constituent oxides, were calculated based on the compositional data and the mineral identification tables listed in the previous section. The method of calculation is described in Appendix B. The results of these calculations are included in Tables V-9 through V-16.

Plots of the abundances of the major minerals in each core versus depth in the Culebra section are shown in Figures V-5 through V-29.

Table V-1. H6B Core X-Ray Diffraction Mineral ID Chart

Sample ID	Depth	Clay	Quartz	Dolomite	Gypsum	Anhydrite	Halite
H6B-1	614	X	X	XXX		tr	X
H6B-2	616	X	X	XXX			X
H6B-3	631	XX	XX			X	X
H6B-4	637	X	X	XXX			
H6B-5a	640	tr	X		XXX		
H6B-5b	640	X	X	X	XXX		

tr = trace
X = present
XX = abundant
XXX = very abundant

Table V-2. H7C Core X-Ray Diffraction Mineral ID Chart

Sample ID	Depth	Clay	Quartz	Dolomite	Calcite	Gypsum	Halite
H7C-1	237.10	tr	tr	XXX		XX	
H7C-2	238.30	tr	tr	XXX			XX
H7C-3	242.55	tr	tr	XXX			XX
H7C-4	252.50	tr	X	XXX			
H7C-5	253.10	tr	X	XXX			
H7C-6	254.60	tr	X	XXX			
H7C-7	256.00	tr	X	XXX			
H7C-8	260.15	tr	X	XXX			
H7C-9	264.70	tr	X	XXX			
H7C-10	266.70	tr	X	XXX			
H7C-11	268.00	tr	X	XXX			
H7C-12	271.60	tr	X	XXX			
H7C-13	273.10	tr	X	XXX			

Table V-3. H10B Core X-Ray Diffraction Mineral ID Chart

Sample ID	Depth	Clay	Quartz	Dolomite	Calcite	Gypsum	Halite
H10B-1	1370.30	X	X	XXX		XX	X
H10B-2	1372.30	tr	X	XXX			X
H10B-3	1373.20	tr	X	XXX		X	X
H10B-4	1374.40	tr	X	XXX		X	X
H10B-5	1375.60	tr	X	XXX			X
H10B-6	1379.40	tr	X	XXX			X
H10B-7	1381.25	tr	X	XXX		XX	X
H10B-8	1381.95	tr	X	XXX		X	X
H10B-9	1383.25	tr	X	XXX		X	X
H10B-10	1385.90	tr	tr	XXX		X	tr
H10B-11	1388.90	tr	X	XXX		X	X
H10B-12	1389.40	tr	X	XXX		tr	X
H10B-13	1392.80	tr	tr	XXX		X	tr
H10B-14	1395.25	tr	X	XXX		X	tr
H10B-15	1396.25	tr	X	XXX		XX	X
H10B-16	1397.25	X	X	XXX		X	X
H10B-17	1398.20	tr	X	XXX		XX	X
H10B-18	1398.95	XXX	XX	tr			tr

Table V-4. H11 Core XRF Compositional Data

Sample ID	Depth	SiO_2	Al_2O_3	CaO	MgO	FeO	Na_2O	K_2O	SO_3	Total
H11-1	731.00	5.46	1.03	25.50	19.24	0.37	0.55	0.39	3.75	56.29
H11-2	732.50	2.88	0.53	27.48	20.27	0.27	0.38	0.24	0.77	52.81
H11-3	736.00	4.33	0.86	26.25	19.48	0.31	0.61	0.28	1.23	53.34
H11-4	736.50	3.97	0.75	27.20	20.43	0.28	0.28	0.29	1.21	54.41
H11-5	737.50	5.91	1.16	26.28	20.48	0.35	0.28	0.44	0.34	55.24

Table V-5. WIPP-12 Core X-Ray Diffraction Mineral ID Chart

Sample ID	Depth	Clay	Quartz	Dolomite	Calcite	Gypsum	Halite
W12-1	828.40	tr	X	XXX			
W12-2	830.50	tr	X	XXX			tr
W12-3	831.40	tr	X	XXX		X	
W12-4	832.00	tr	X	XXX			
W12-5	833.70	tr	X	XXX		X	
W12-6	834.50	X	X	XXX		X	
W12-7	835.10	tr	X	XXX		X	tr
W12-8	836.20	tr	X	XXX		X	
W12-9	836.70	tr	X	XXX		X	
W12-10	837.00	tr	X	XXX		X	
W12-11	837.70	tr	X	XXX			tr
W12-12	838.60	tr	X	XXX			tr
W12-13	839.30	tr	X	XXX		X	tr
W12-14	839.80	tr	X	XXX		tr	tr
W12-15	840.60	tr	X	XXX			tr
W12-16	842.20	X	X	XX			X
W12-17	842.40	tr	X	XXX		X	X

Table V-6. WIPP-25 X-Ray Diffraction Mineral ID Chart

Sample ID	Depth	Clay	Quartz	Dolomite	Calcite	Gypsum	Halite
W25-1	446.90	X	X	XXX		X	XX
W25-2	447.30	tr	X	XXX			X
W25-3	447.40	XXX	XX	XX			XX
W25-4	450.00	tr	X	XXX			tr
W25-5	450.50	X	X	XXX			X
W25-6	451.50	tr	X	XXX			tr
W25-7	452.00	tr	X	XXX			tr
W25-8	453.95	X	X	XXX			tr
W25-9	456.00	X	X	XXX			X
W25-10	459.00	tr	X	XXX			X
W25-11	462.00	tr	X	XXX			X
W25-12	470.00	X	X	XXX			X
W25-13	473.10	XXX	XX	X			
W25-14	473.95	XXX	XX	X			
W25-15	475.40	XXX	XX				
W25-16	477.20	XXX	XX		X		
W25-17	478.50	XXX	XX		X	X	
W25-18	479.90	XXX	XX			X	
W25-19	483.40	tr	tr			XXX	
W25-20	483.90	tr	tr		X	XXX	
W25-21	485.95	tr	tr			XXX	
W25-22	490.60	tr	X			XXX	

Table V-7. WIPP-26 Core X-Ray Diffraction Mineral ID Chart

Sample ID	Depth	Clay	Quartz	Dolomite	Calcite	Gypsum	Halite
W26-1	188.00	tr	X	XXX			X
W26-2	188.70	tr	X	XXX			
W26-3	189.90	tr	X	XXX			tr
W26-4	190.95	tr	X	XXX			
W26-5	192.40	tr	X	XXX			
W26-6	193.20	tr	X	XXX			
W26-7	194.50	tr	X	XXX			X
W26-8	198.00	tr	X	XXX			tr

Table V-8. WIPP-29 Core X-Ray Diffraction Mineral ID Chart

Sample ID	Depth	Clay	Quartz	Dolomite	Calcite	Gypsum	Halite
W29-1	8.50	tr	X	XXX	XX		
W29-2	9.70	tr	X	XXX	X		X
W29-3	13.00	tr	tr	XXX	X		X
W29-4	13.50	tr	X	XXX	XX		X
W29-5	18.10	tr	X	XXX	X		X
W29-6	19.25	tr	X	XXX	XX		X
W29-7	20.20	X	X	XXX	X		X
W29-8	21.55	tr	X	XXX			X
W29-9	22.40	tr	X	XXX	X		X
W29-10	23.55	X	X	XXX			X
W29-11	24.50	tr	X	XXX			X
W29-12	26.00	X	X	XXX			X
W29-13	27.50	X	X	XXX	X		X
W29-14	29.30	X	X	XXX			X
W29-15	31.15	tr	X	XXX			X
W29-16	32.00	tr	X	XXX			X
W29-17	32.55	tr	X	XXX			X
W29-18	43.60	XXX	XX	tr			

Table V-9. H6B Core Quantitative Mineral Analysis

Sample ID	Depth	Clay	Quartz	Dolomite	Gypsum	Anhydrite	Halite	Total
H6B-1	614.00	9.07	2.57	77.09	0.00	0.39	0.00	88.73
H6B-2	616.00	6.61	2.08	89.28	0.00		0.00	97.98
H6B-3	631.00	83.86	12.46	0.00	0.00	n.a.	1.18	97.49
H6B-4	637.00	4.96	2.02	91.78	0.00		0.00	98.76
H6B-5a	640.00	2.72	1.26	0.00	70.33		0.00	74.31
H6B-5b	640.00	10.56	4.63	6.69	63.78		0.00	85.65

Table V-10. H7C Core Quantitative Mineral Analysis

Sample ID	Depth	Clay	Quartz	Dolomite	Gypsum	Halite	Total
H7C-1	237.10	0.36	0.09	59.68	27.15	0.00	87.28
H7C-2	238.30	0.68	0.19	95.09	0.00	0.10	96.06
H7C-3	242.55	0.61	0.13	95.25	0.00	0.09	96.08
H7C-4	252.50	0.37	0.09	94.08	0.00	0.00	94.53
H7C-5	253.10	1.10	0.39	93.53	0.00	0.00	95.02
H7C-6	254.60	3.24	0.88	92.58	0.00	0.00	96.69
H7C-7	256.00	3.29	0.86	91.98	0.00	0.00	96.12
H7C-8	260.15	3.92	1.05	93.25	0.00	0.00	98.22
H7C-9	264.70	8.87	2.35	85.29	0.00	0.00	96.51
H7C-10	266.70	5.77	1.75	88.80	0.00	0.00	96.31
H7C-11	268.00	3.43	1.24	91.68	0.00	0.00	96.35
H7C-12	271.60	3.49	1.01	91.60	0.00	0.00	96.10
H7C-13	273.10	2.08	0.58	93.25	0.00	0.00	95.91

Table V-11. H10B Core Quantitative Mineral Analysis

Sample ID	Depth	Clay	Quartz	Dolomite	Calcite	Gypsum	Halite	Total
H10-1	1370.30	12.77	3.51	61.32	0.00	14.48	0.23	92.31
H10-2	1372.30	2.66	1.00	80.90	0.00	0.00	0.35	84.91
H10-3	1373.20	1.05	0.27	81.88	0.00	5.71	0.27	89.19
H10-4	1374.40	1.91	0.73	79.04	0.00	4.03	0.19	85.89
H10-5	1375.60	1.81	0.56	89.59	0.00	0.00	0.29	92.25
H10-6	1379.40	3.12	0.97	91.51	0.00	0.00	0.19	95.78
H10-7	1381.25	3.46	1.05	66.16	0.00	22.22	0.11	93.00
H10-8	1381.95	6.61	1.61	78.47	0.00	6.27	0.25	93.22
H10-9	1383.25	2.29	0.68	82.14	0.00	7.07	0.17	92.35
H10-10	1385.90	3.10	1.03	84.29	0.00	6.32	0.17	94.92
H10-11	1388.90	2.56	0.93	92.74	0.00	4.33	0.19	100.75
H10-12	1389.40	2.15	0.91	86.04	0.00	3.43	0.15	92.68
H10-13	1392.80	1.47	0.50	84.08	0.00	8.29	0.16	94.50
H10-14	1395.25	1.42	0.62	82.23	0.00	10.70	0.13	95.11
H10-15	1396.25	1.96	0.80	64.41	0.00	24.19	0.16	91.52
H10-16	1397.25	12.65	4.04	79.19	0.00	3.84	0.35	100.07
H10-17	1398.20	2.40	1.03	74.87	0.00	15.35	0.14	93.79

Table V-12. H11 Core Quantitative Mineral Analysis

Sample ID	Depth	Clay	Quartz	Dolomite	Gypsum	Anhydrite	Halite	Total
H11-1	731.00	6.89	2.29	75.26	0.00	6.37	0.70	91.50
H11-2	732.50	3.54	1.25	90.39	0.00	0.00	0.48	95.66
H11-3	736.00	5.71	1.71	83.50	0.00	2.09	0.77	93.78
H11-4	736.50	4.99	1.67	86.67	2.60	0.00	0.35	96.29
H11-5	737.50	7.75	2.35	85.67	0.73	0.00	0.35	96.85

Table V-13. WIPP-12 Core Quantitative Mineral Analysis

Sample ID	Depth	Clay	Quartz	Dolomite	Gypsum	Halite	Total
W12-1	828.40	5.99	1.96	91.46	0.00	0.00	99.41
W12-2	830.50	4.83	1.67	92.83	0.00	0.18	99.50
W12-3	831.40	2.07	0.97	94.85	1.77	0.00	99.66
W12-4	832.00	1.93	0.76	96.12	0.00	0.00	98.82
W12-5	833.70	1.96	0.82	80.70	12.99	0.00	96.48
W12-6	834.50	1.84	0.80	91.51	4.04	0.00	98.19
W12-7	835.10	1.55	0.73	91.61	3.96	0.00	97.85
W12-8	836.20	1.72	0.75	89.07	7.09	0.00	98.63
W12-9	836.70	1.42	0.68	91.03	5.06	0.00	98.19
W12-10a	837.00	1.50	0.60	90.11	5.88	0.00	98.08
W12-10b	837.20	1.13	0.58	89.15	6.69	0.00	97.55
W12-11	837.70	2.50	1.07	95.02	0.00	0.29	98.88
W12-12	838.60	1.82	0.78	96.29	0.00	0.24	99.13
W12-13	839.30	1.46	0.66	95.62	0.00	0.26	97.99
W12-14	839.80	1.50	0.66	95.94	0.00	0.22	98.32
W12-15	840.60	2.39	0.89	94.39	0.00	0.29	97.96
W12-16	842.20	21.52	6.20	64.92	0.00	0.53	93.17
W12-17	842.40	2.78	1.02	93.83	0.00	0.29	97.93

Table V-14. WIPP-25 Core Quantitative Mineral Analysis

Sample ID	Depth	Clay	Quartz	Dolomite	Gypsum	Halite	Total
W25-1	446.90	18.29	13.02	59.14	3.85	4.92	99.23
W25-2	447.30	3.47	1.57	90.71	0.00	0.18	95.93
W25-3	447.40	58.64	21.81	21.99	0.00	2.10	104.54
W25-4	450.00	6.94	2.26	86.17	0.00	0.17	95.54
W25-5	450.50	5.31	1.79	87.78	0.00	0.27	95.16
W25-6	451.50	7.17	2.41	86.75	0.00	0.10	96.44
W25-7	452.00	7.15	2.37	86.45	0.00	0.12	96.09
W25-8	453.95	7.46	2.46	87.59	0.00	0.13	97.65
W25-9	456.00	5.20	1.68	83.62	0.00	0.87	91.37
W25-10	459.00	3.30	1.12	90.65	0.00	0.37	95.44
W25-11	462.00	2.72	0.97	92.27	0.00	0.21	96.17
W25-12	470.00	1.93	0.74	93.33	0.00	0.23	96.24
W25-13	473.10	65.46	18.94	2.93	0.00	0.00	87.34
W25-14	473.95	58.52	21.15	6.33	0.00	0.00	86.00
W25-19	483.40	0.19	0.06	0.00	82.92	0.00	83.16
W25-20	483.90	0.59	0.60	0.00	76.29	0.00	77.48
W25-21	485.95	0.31	0.10	0.00	83.59	0.00	84.00
W25-22	490.60	2.12	0.52	0.00	78.23	0.00	80.87

Table V-15. WIPP-26 Core Quantitative Mineral Analysis

Sample ID	Depth	Clay	Quartz	Dolomite	Halite	Total
W26-1	188.00	7.49	2.36	85.99	0.18	96.02
W26-2	188.70	6.05	1.89	89.51	0.00	97.45
W26-3	189.90	9.98	2.98	83.81	0.10	96.87
W26-4	190.95	6.36	2.00	89.41	0.00	97.77
W26-5	192.40	10.82	2.99	83.51	0.00	97.33
W26-6	193.20	8.10	2.92	86.37	0.00	97.38
W26-7	194.50	3.16	1.25	92.69	0.14	97.25
W26-8	198.00	1.11	0.45	95.82	0.15	97.52

Table V-16. WIPP-29 Core Quantitative Mineral Analysis

Sample ID	Depth	Clay	Quartz	Dolomite	Calcite	Gypsum	Halite
W29-1	8.50	1.11	0.52	63.97	26.05	0.00	0.00
W29-2	9.70	2.13	0.79	88.32	5.74	0.00	0.12
W29-3	13.00	0.79	0.28	67.43	22.55	0.00	0.19
W29-4	13.50	1.59	0.56	59.33	31.51	0.00	0.23
W29-5	18.10	2.80	1.00	89.53	2.03	0.00	0.29
W29-6	19.25	3.11	1.08	39.13	44.25	0.00	0.12
W29-7	20.20	3.97	1.54	74.06	13.86	0.00	0.17
W29-8	21.55	6.17	1.78	89.76	0.00	0.00	0.13
W29-9	22.40	7.00	2.06	83.87	2.22	0.00	0.15
W29-10	23.55	10.77	3.46	78.33	0.00	0.00	0.33
W29-11	24.50	5.36	1.84	90.60	0.00	0.00	0.17
W29-12	26.00	3.52	1.14	89.46	0.00	0.00	0.15
W29-13	27.50	4.67	1.73	87.17	1.63	0.00	0.23
W29-14	29.30	1.88	1.47	90.64	0.00	0.00	0.24
W29-15	31.15	1.88	0.63	90.81	0.00	0.00	0.27
W29-16	32.00	4.21	1.57	92.64	0.00	0.00	0.26
W29-17	32.55	2.36	0.87	91.76	0.00	0.00	0.25

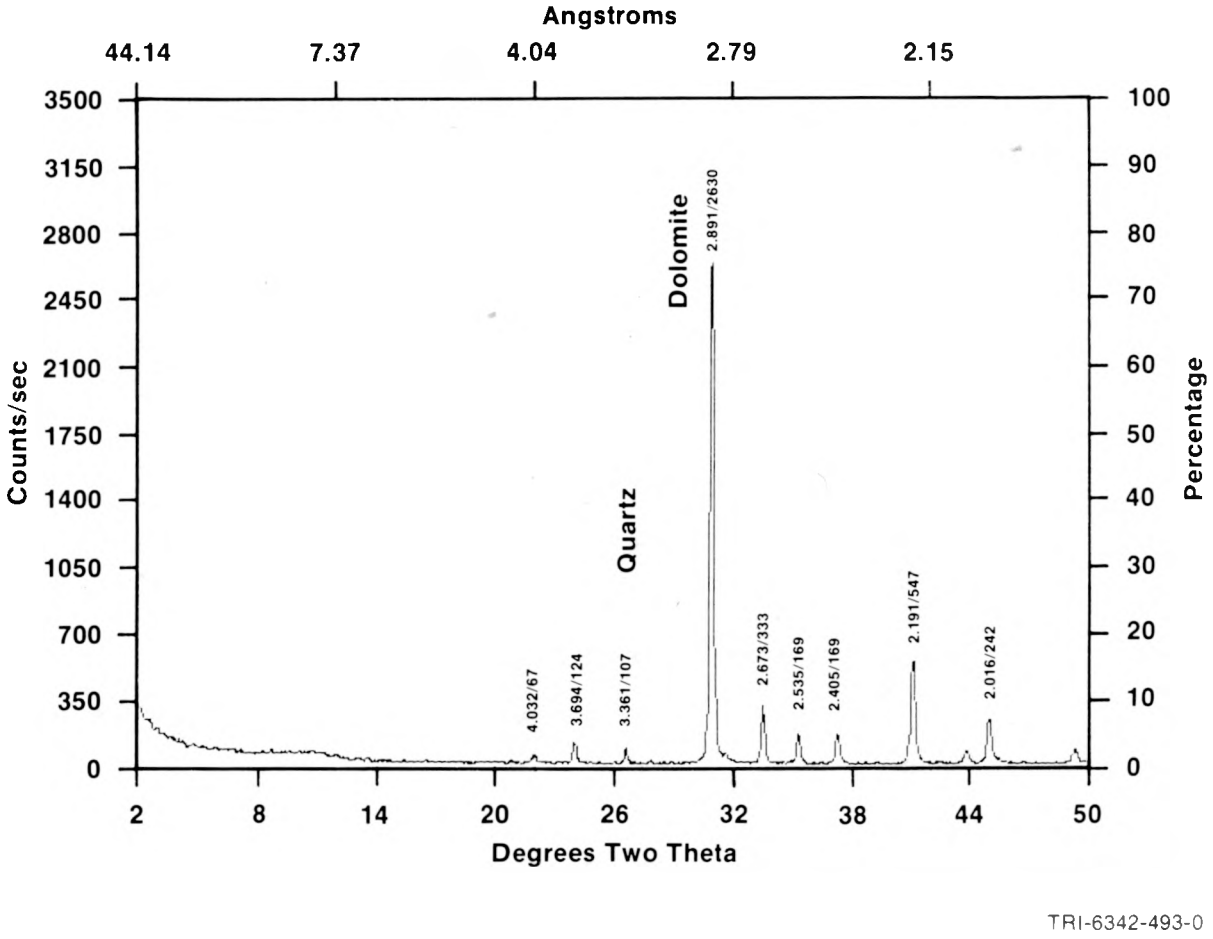

Figure V-1. X-Ray Diffractogram for Sample WIPP-12-4. Peaks represent angstroms/counts per seconds.

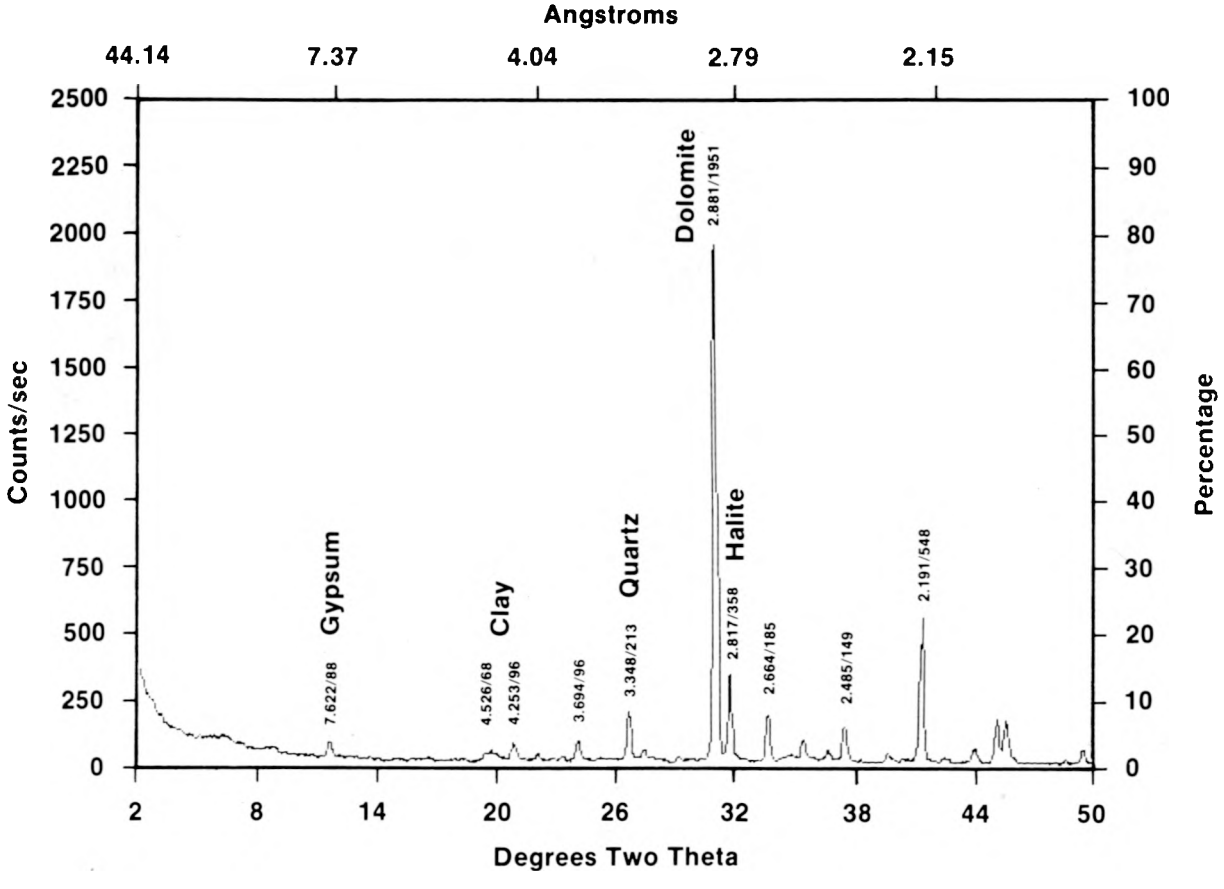

Figure V-2. X-Ray Diffractogram for Sample WIPP-25-1. Peaks represent angstroms/counts per seconds.

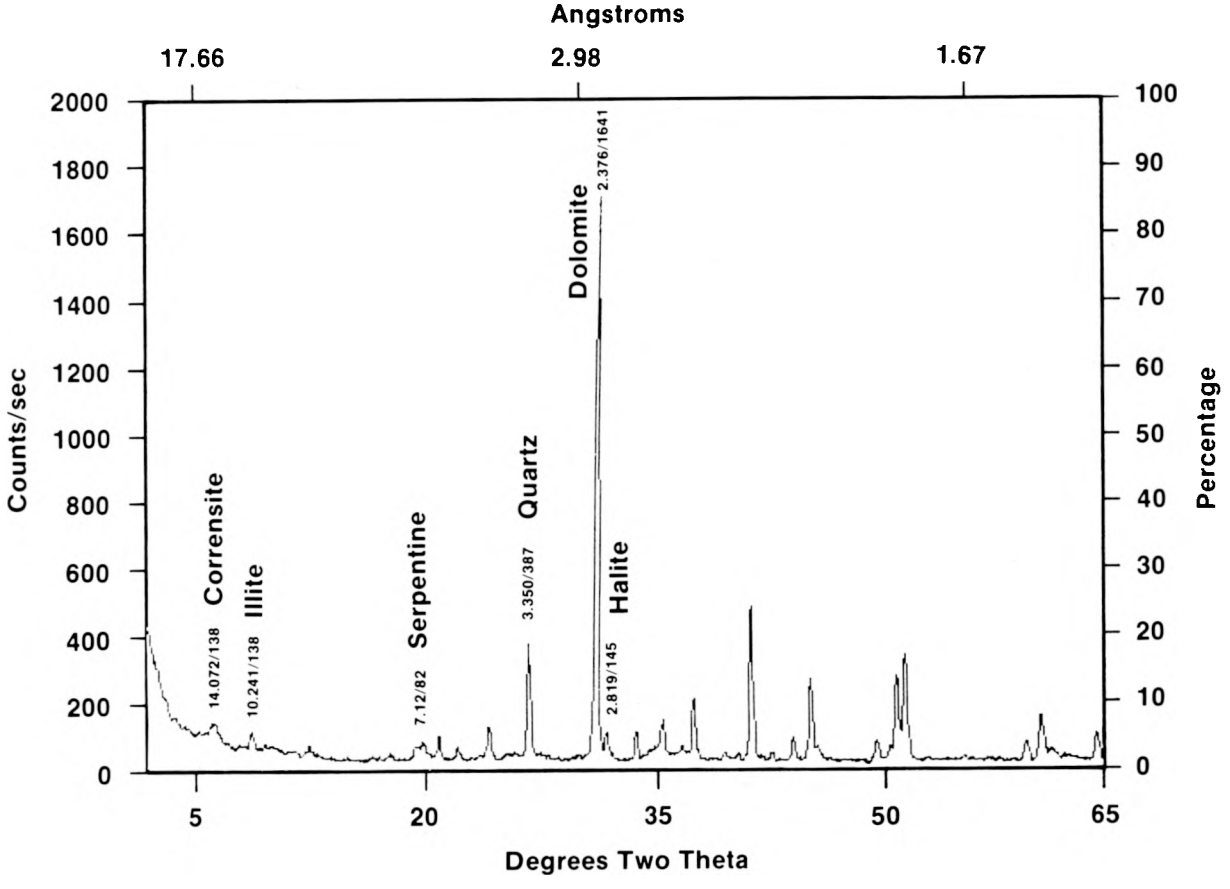

Figure V-3. X-Ray Diffractogram for Sample WIPP-12-16. Peaks represent angstroms/counts per seconds.

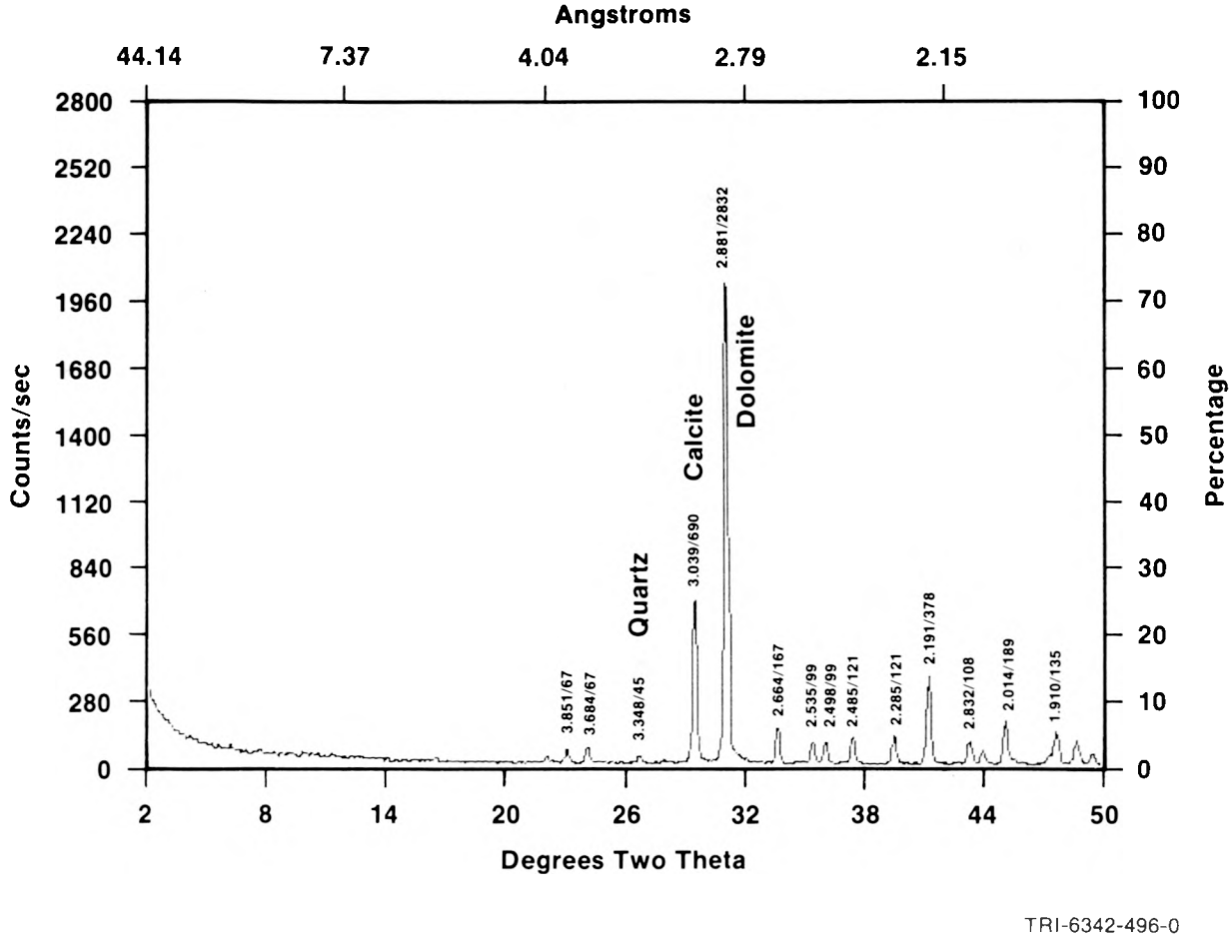

Figure V-4. X-Ray Diffractogram for Sample WIPP-29-1. Peaks represent angstroms/counts per seconds.

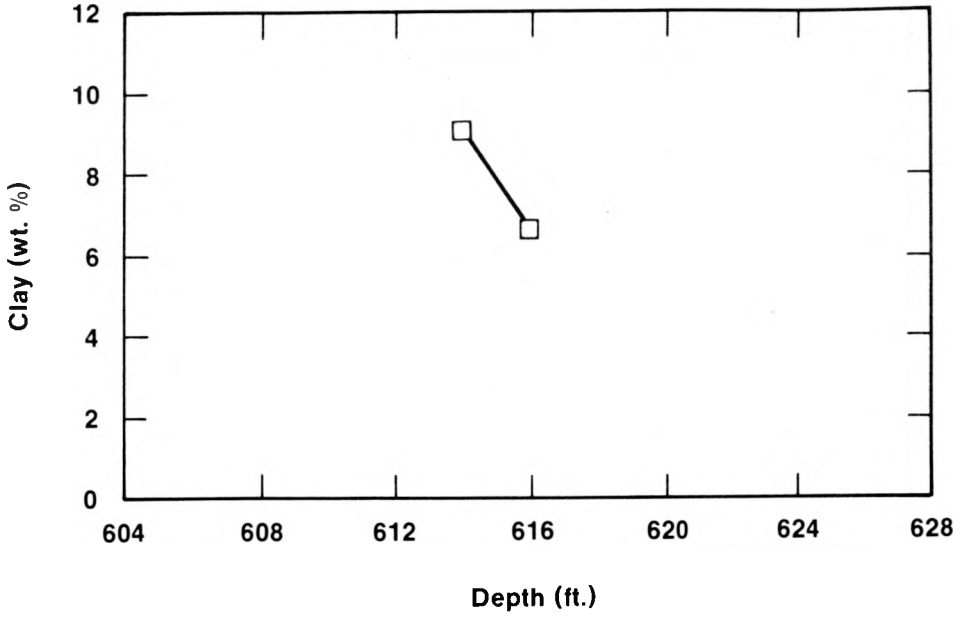

Figure V-5. H6B Core: Clay vs. Depth.

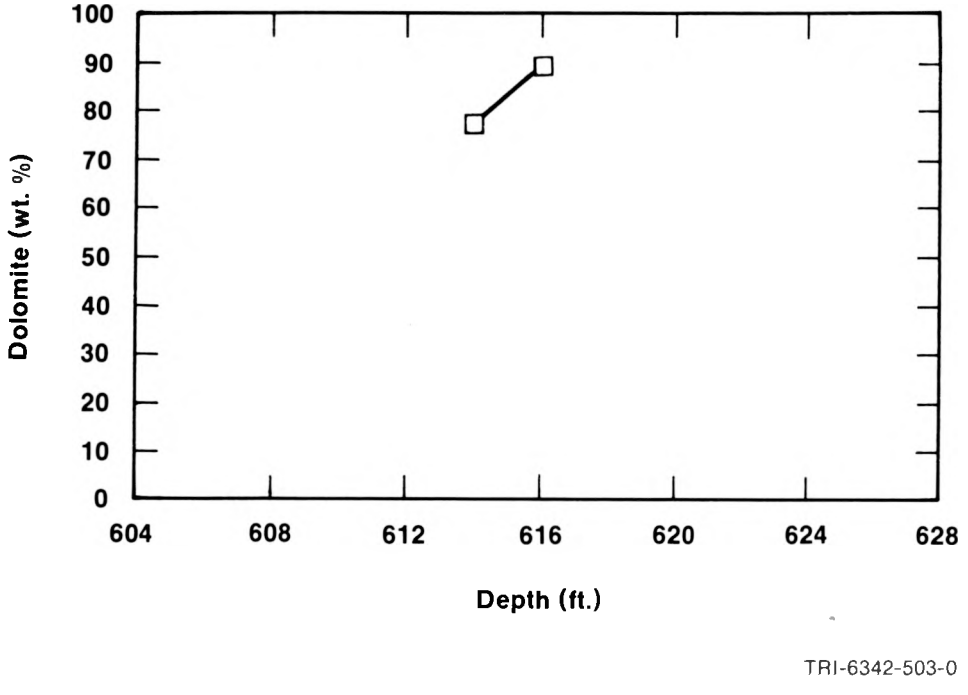

Figure V-6. H6B Core: Dolomite vs. Depth.

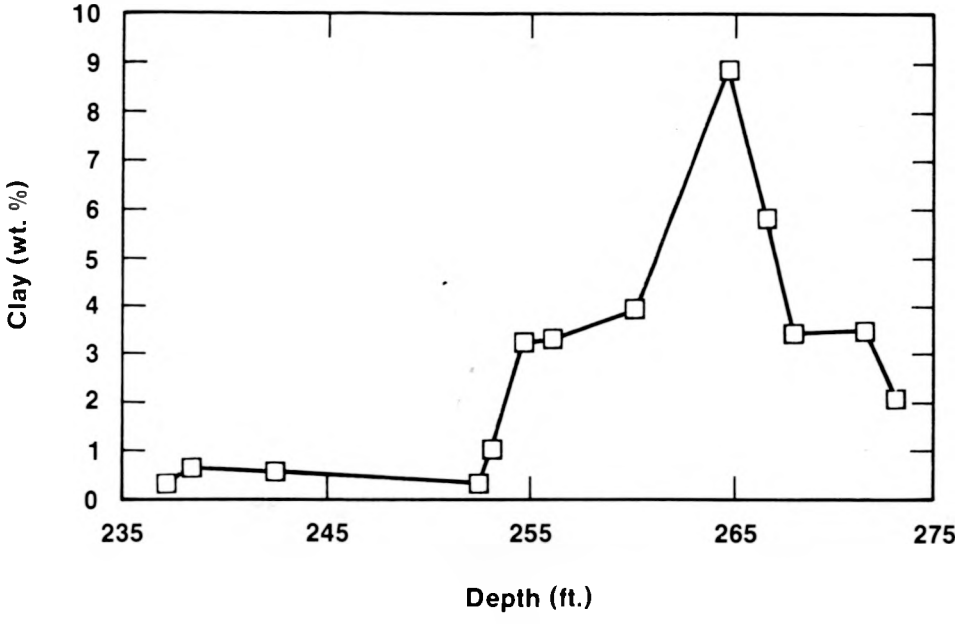

TRI-6342-510-0

Figure V-7. H7 Core: Clay vs. Depth.

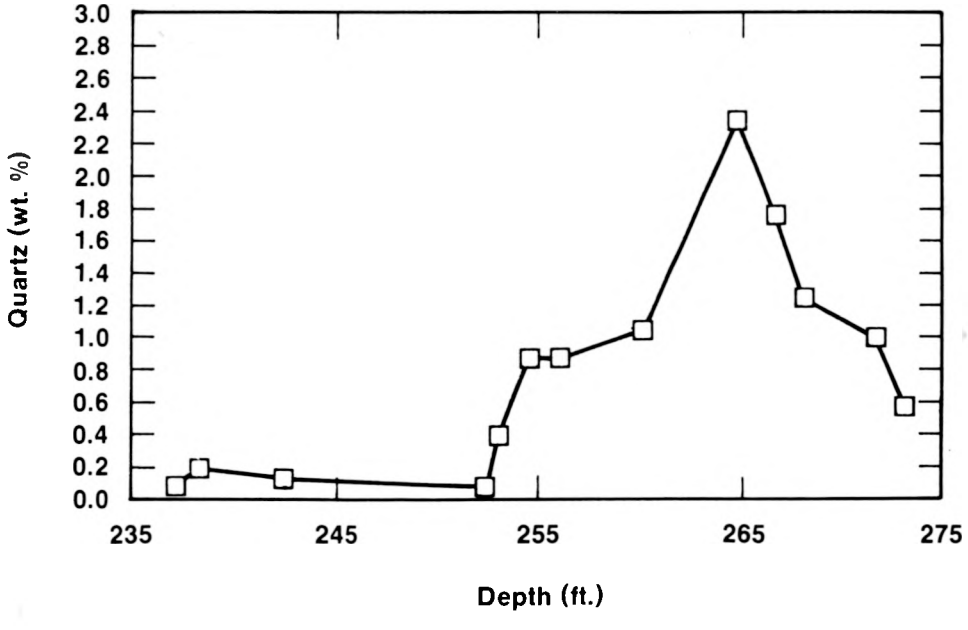

TRI-6342-511-0

Figure V-8. H7 Core: Quartz vs. Depth.

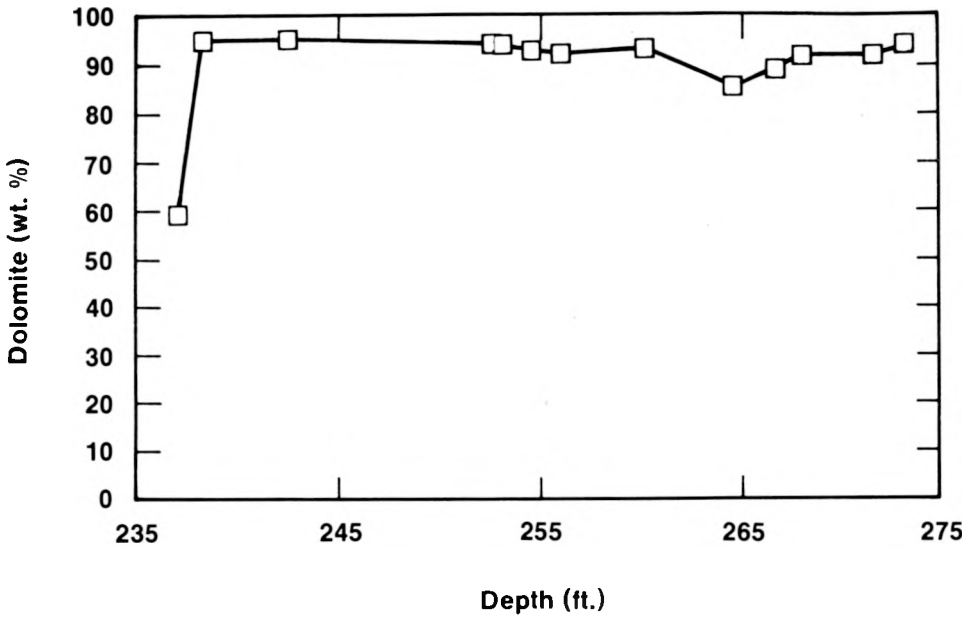

Figure V-9. H7 Core: Dolomite vs. Depth.

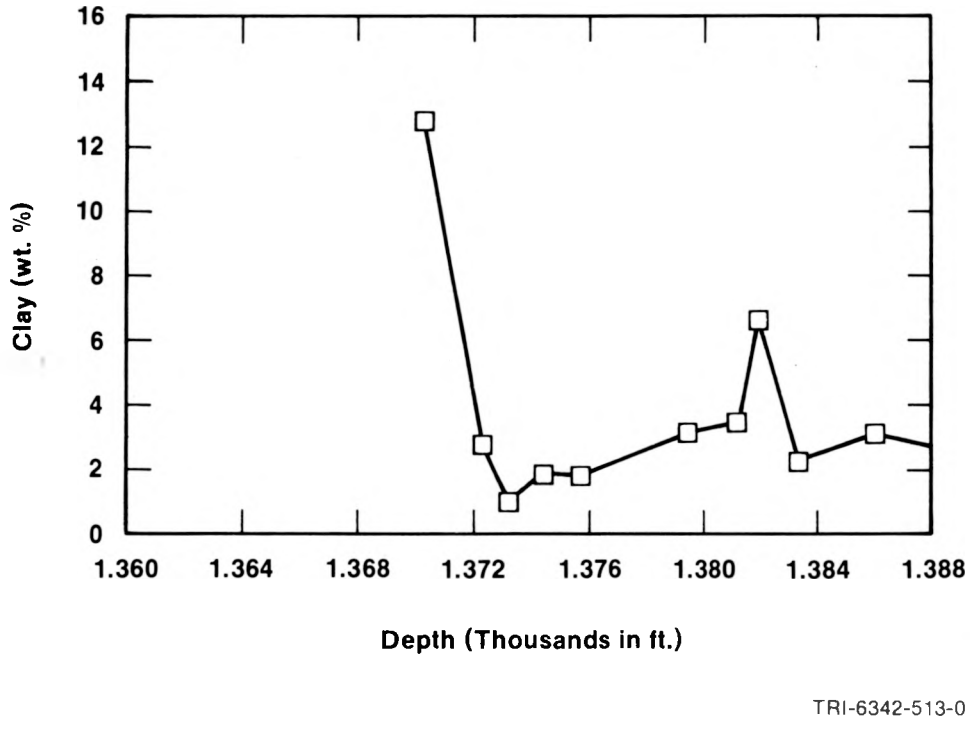

Figure V-10. H10 Core: Clay vs. Depth.

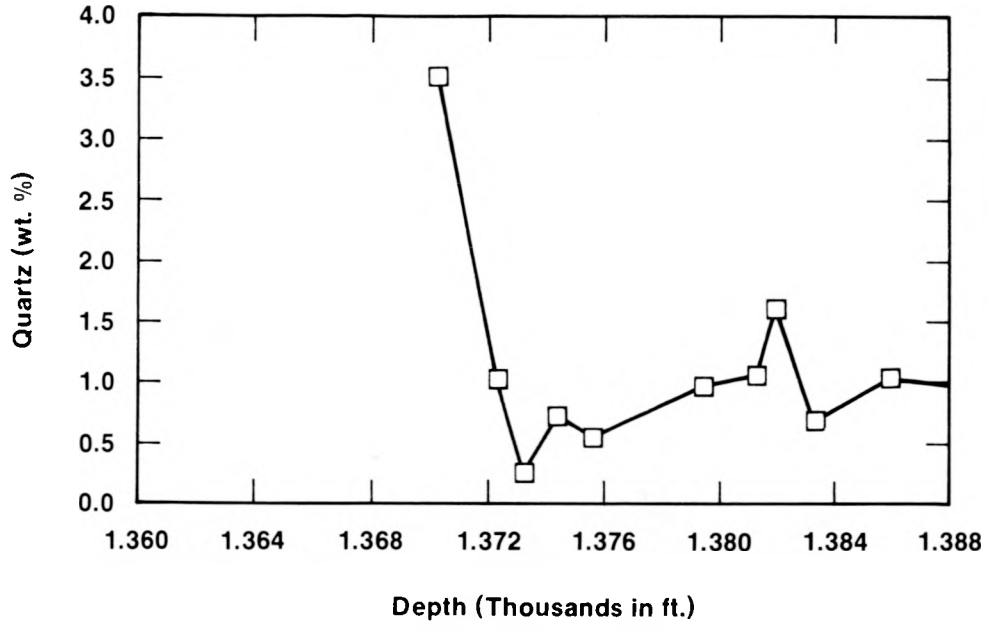

TRI-6342-514-0

Figure V-11. H10 Core: Quartz vs. Depth.

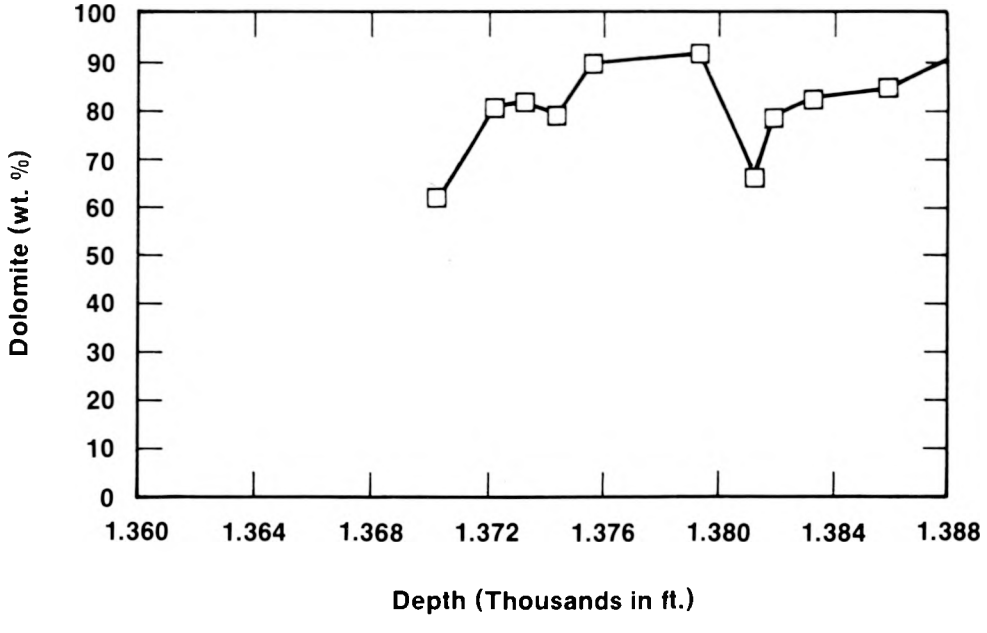

TRI-6342-515-0

Figure V-12. H10 Core: Dolomite vs. Depth.

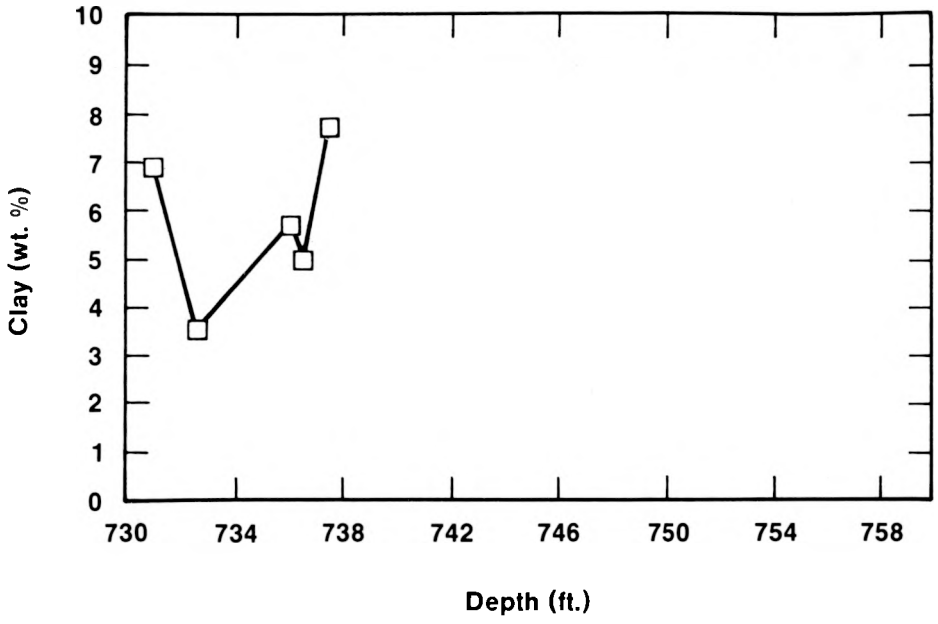

Figure V-13. H11 Core: Clay vs. Depth.

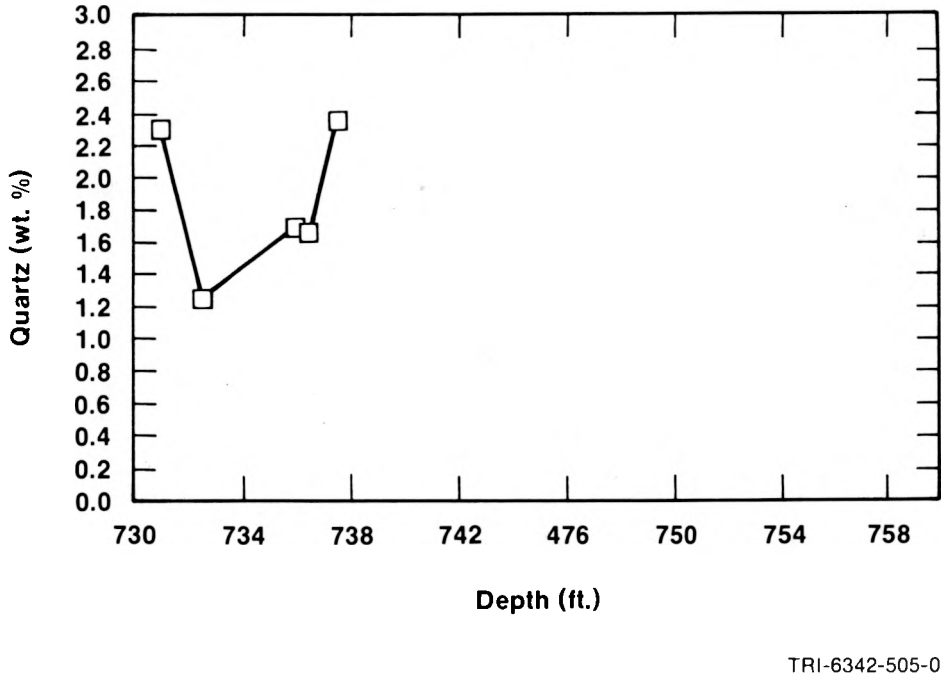

Figure V-14. H11 Core: Quartz vs. Depth.

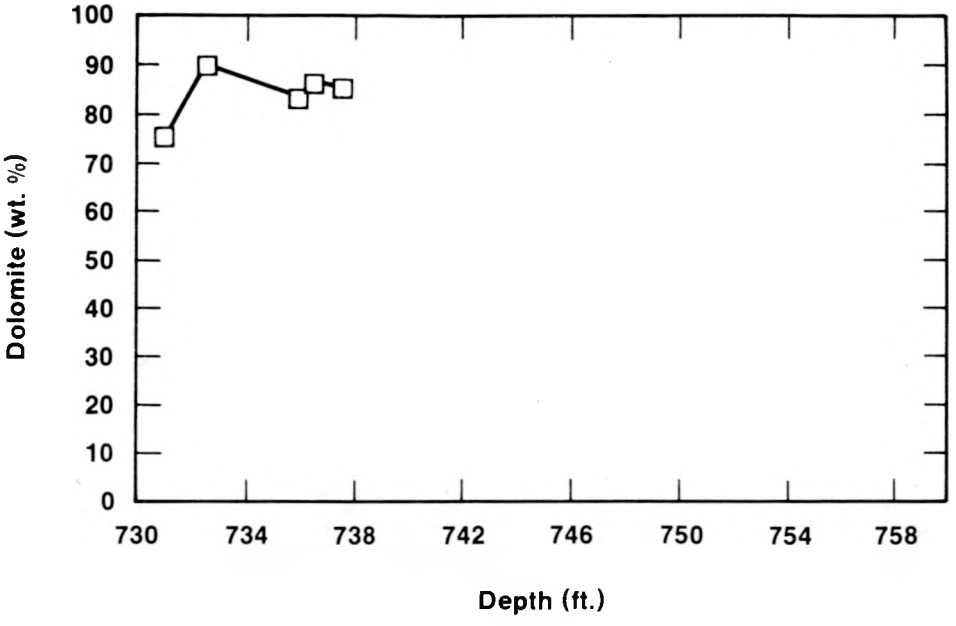

TRI-6342-506-0

Figure V-15. H11 Core: Dolomite vs. Depth.

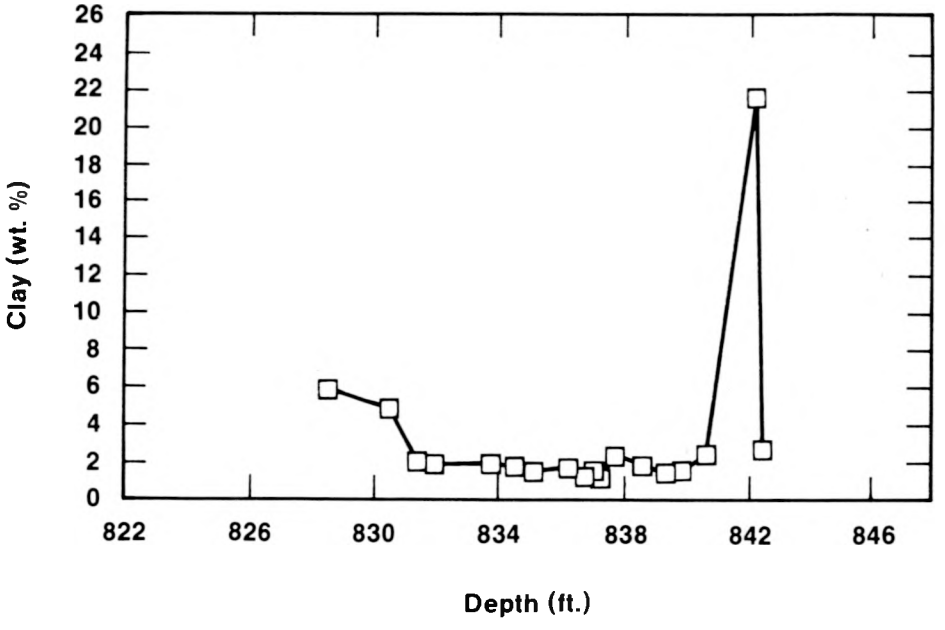

TRI-6342-516-0

Figure V-16. WIPP-12 Core: Clay vs. Depth.

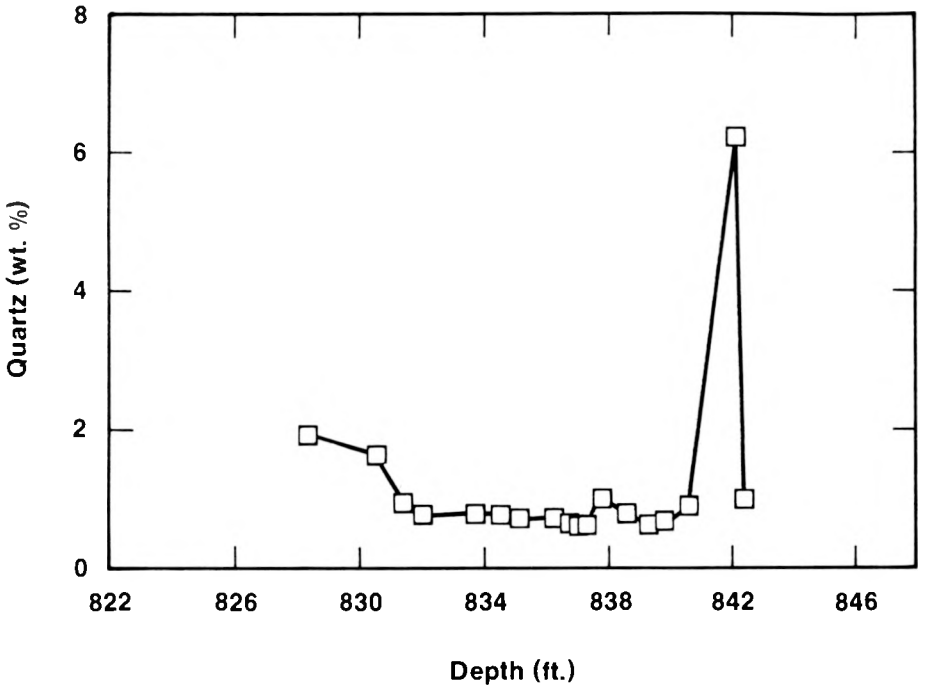

Figure V-17. WIPP-12 Core: Quartz vs. Depth.

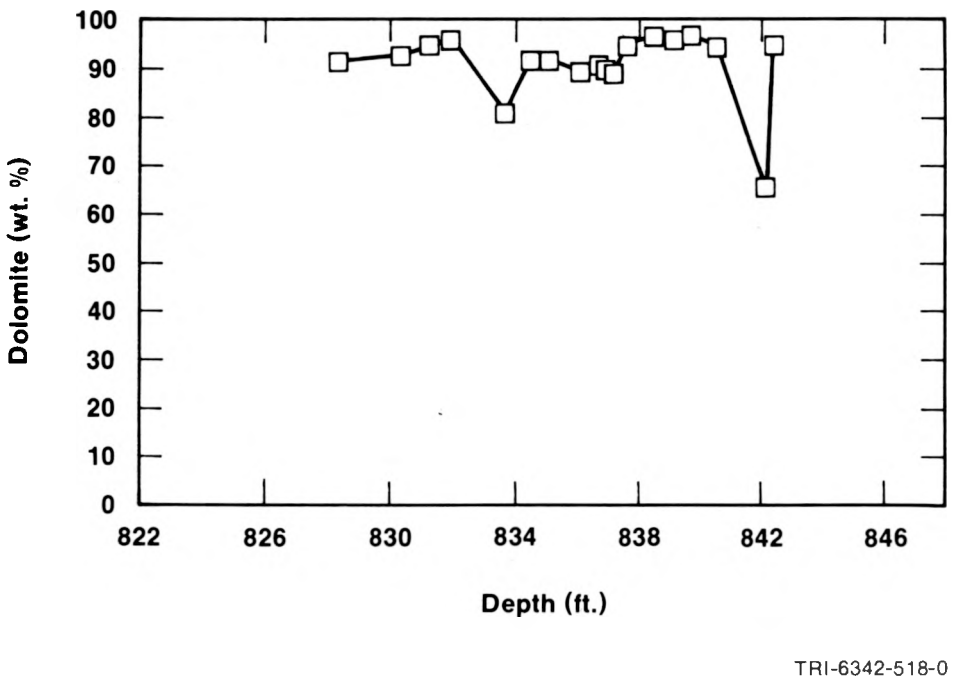

Figure V-18. WIPP-12 Core: Dolomite vs. Depth.

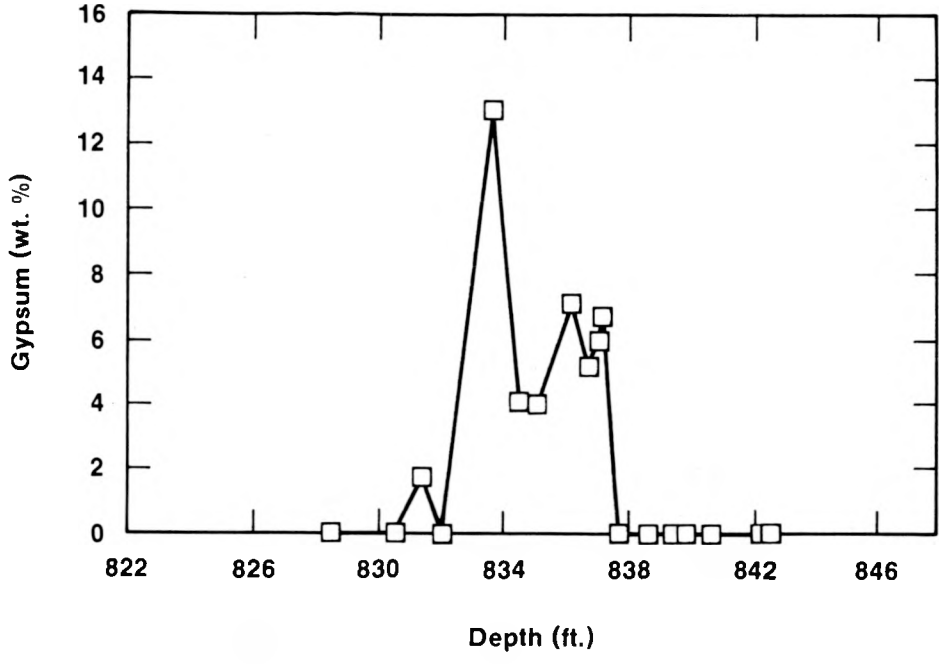

TRI-6342-519-0

Figure V-19. WIPP-12 Core: Gypsum vs. Depth.

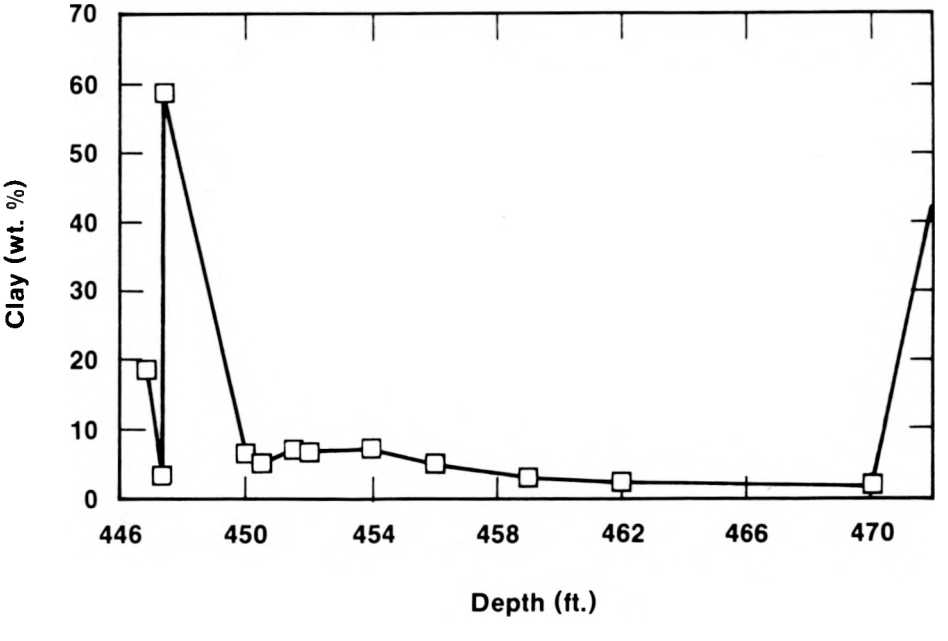

TRI-6342-520-0

Figure V-20. WIPP-25 Core: Clay vs. Depth.

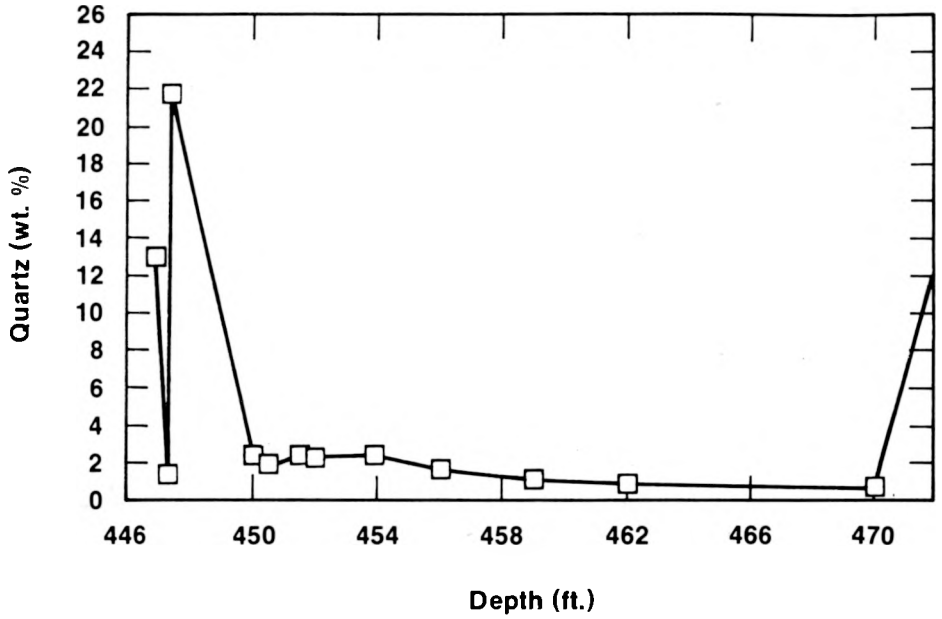

Figure V-21. WIPP-25 Core: Quartz vs. Depth.

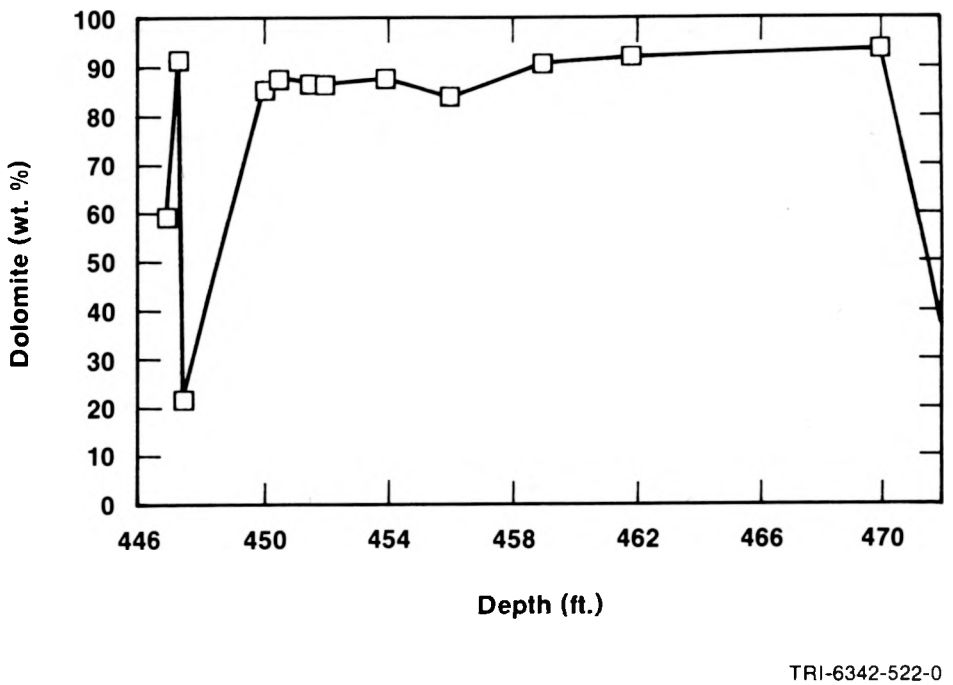

Figure V-22. WIPP-25 Core: Dolomite vs. Depth.

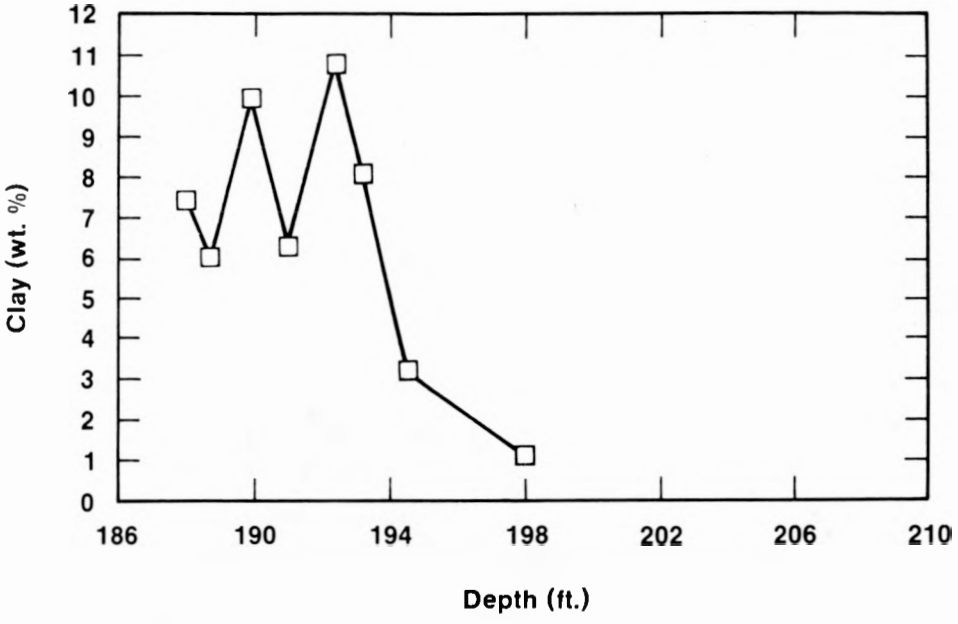

Figure V-23. WIPP-26 Core: Clay vs. Depth.

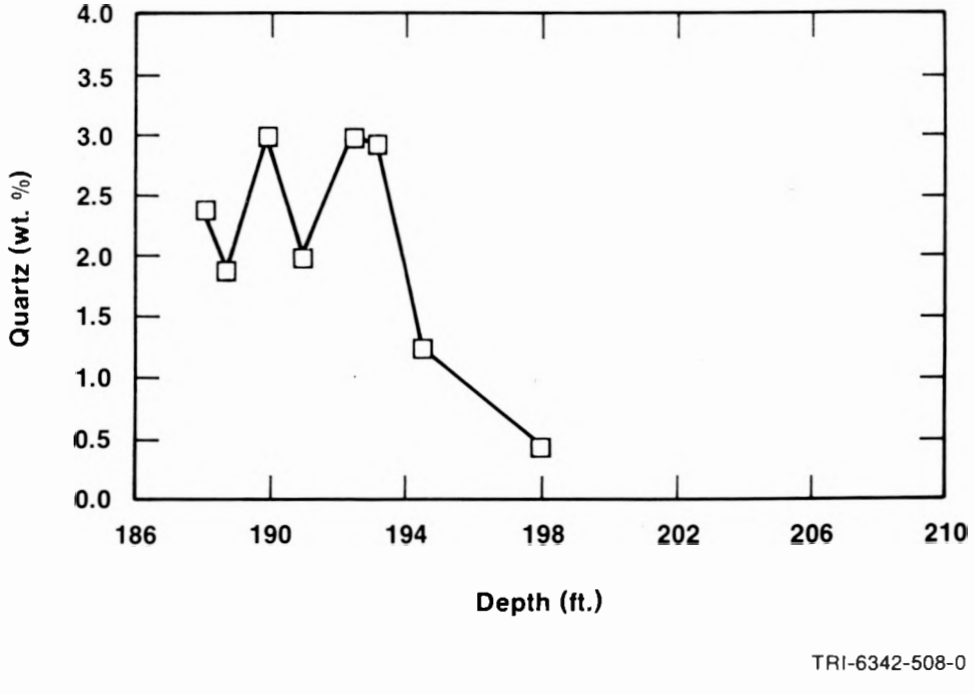

Figure V-24. WIPP-26 Core: Quartz vs. Depth.

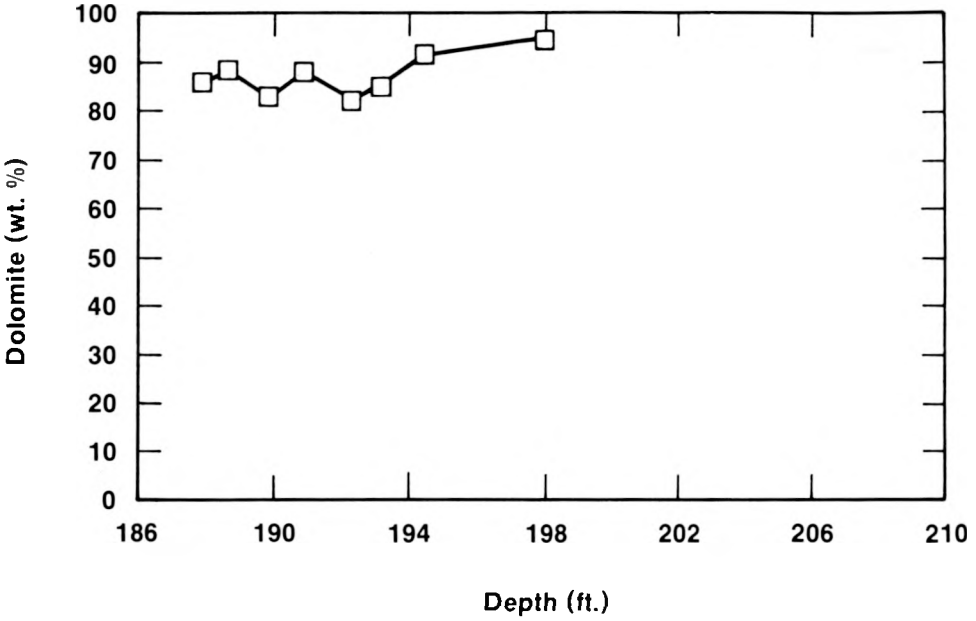

Figure V-25. WIPP-26 Core: Dolomite vs. Depth.

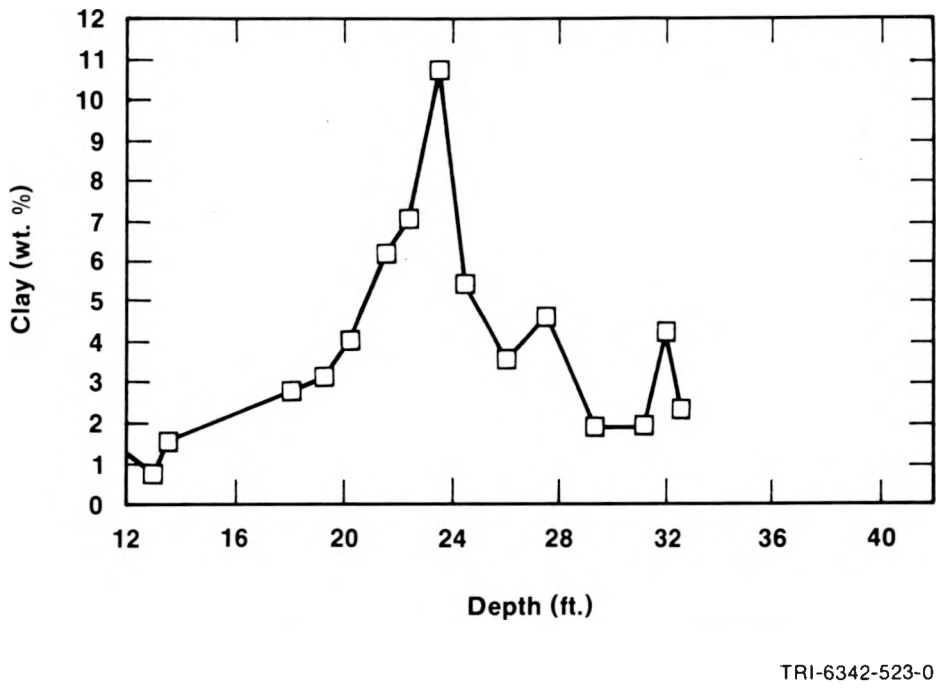

Figure V-26. WIPP-29 Core: Clay vs. Depth.

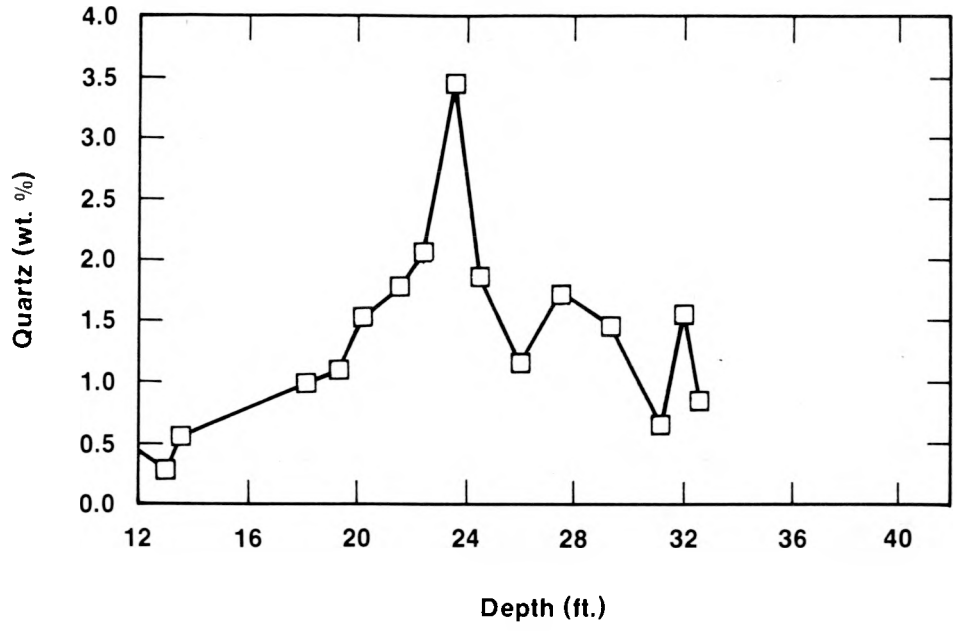

TRI-6342-524-0

Figure V-27. WIPP-29 Core: Quartz vs. Depth.

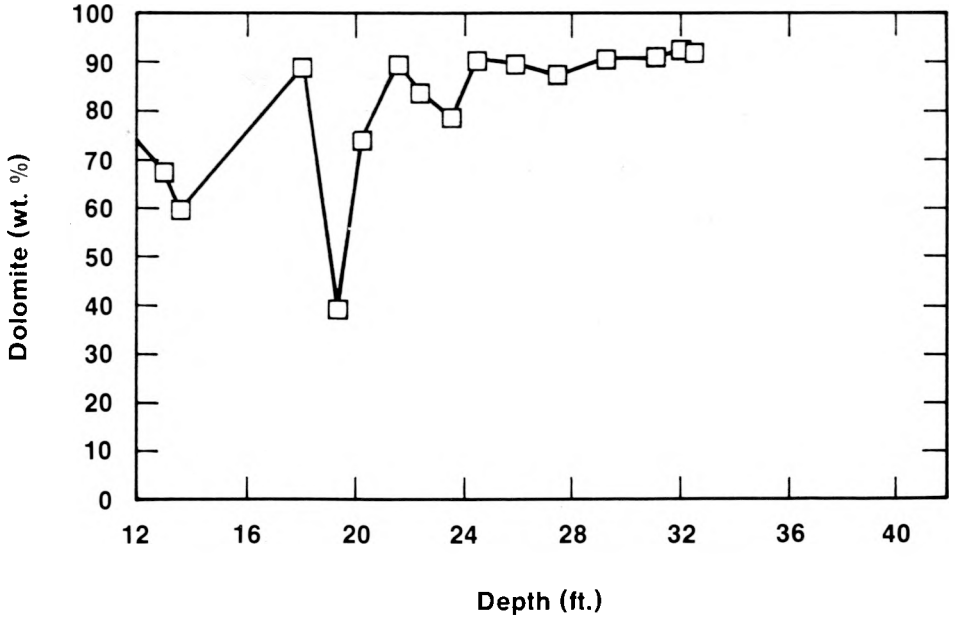

TRI-6342-525-0

Figure V-28. WIPP-29 Core: Dolomite vs. Depth.

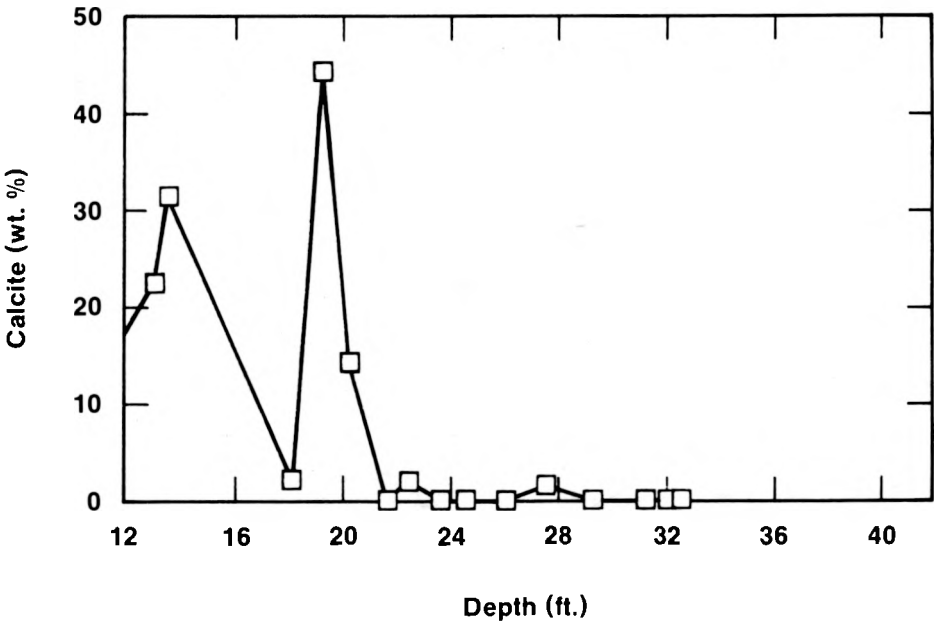

Figure V-29. WIPP-29 Core: Calcite vs. Depth.

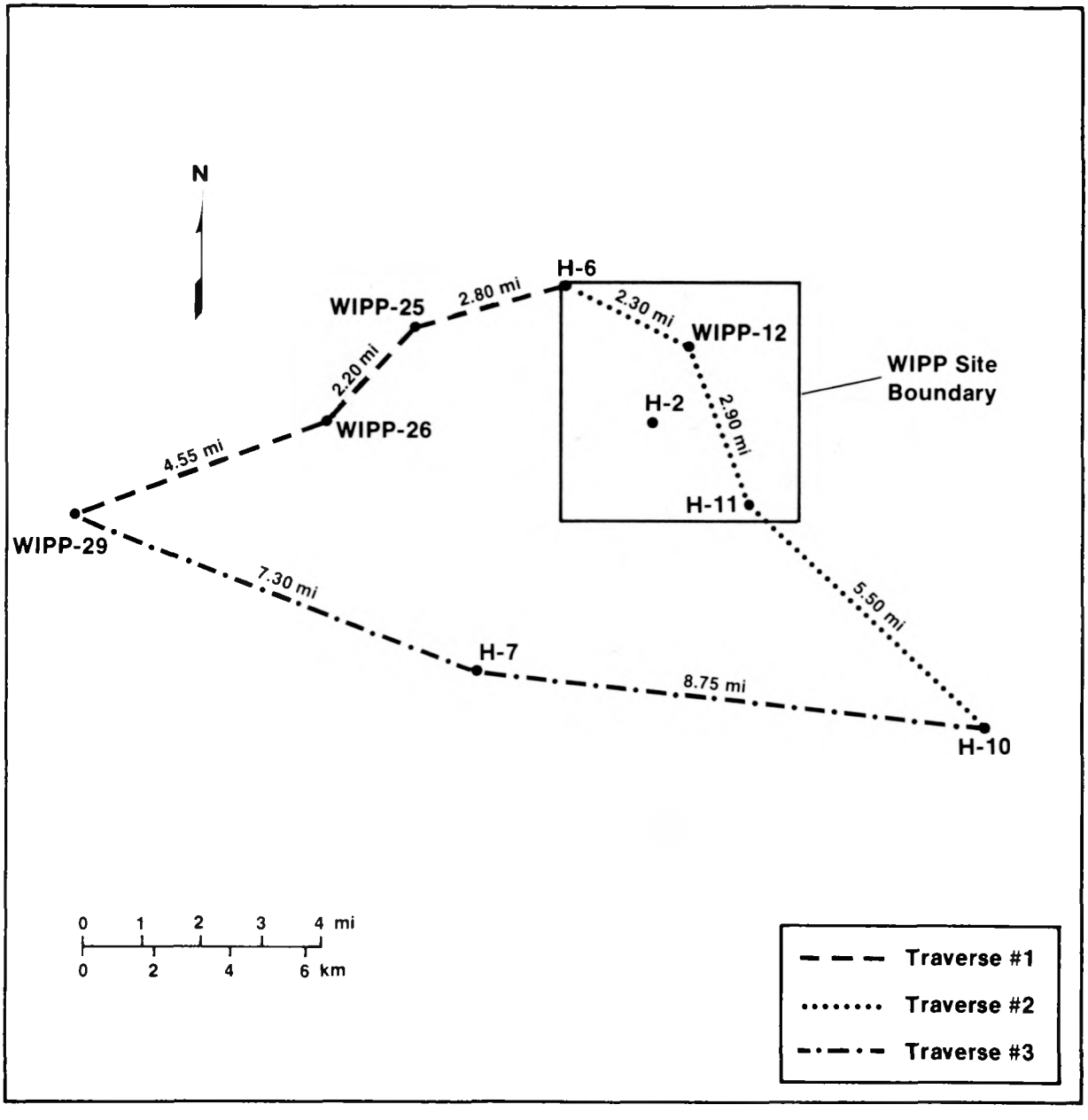

TRI-6342-485-0

Figure V-30. Fence Diagram Traverses.

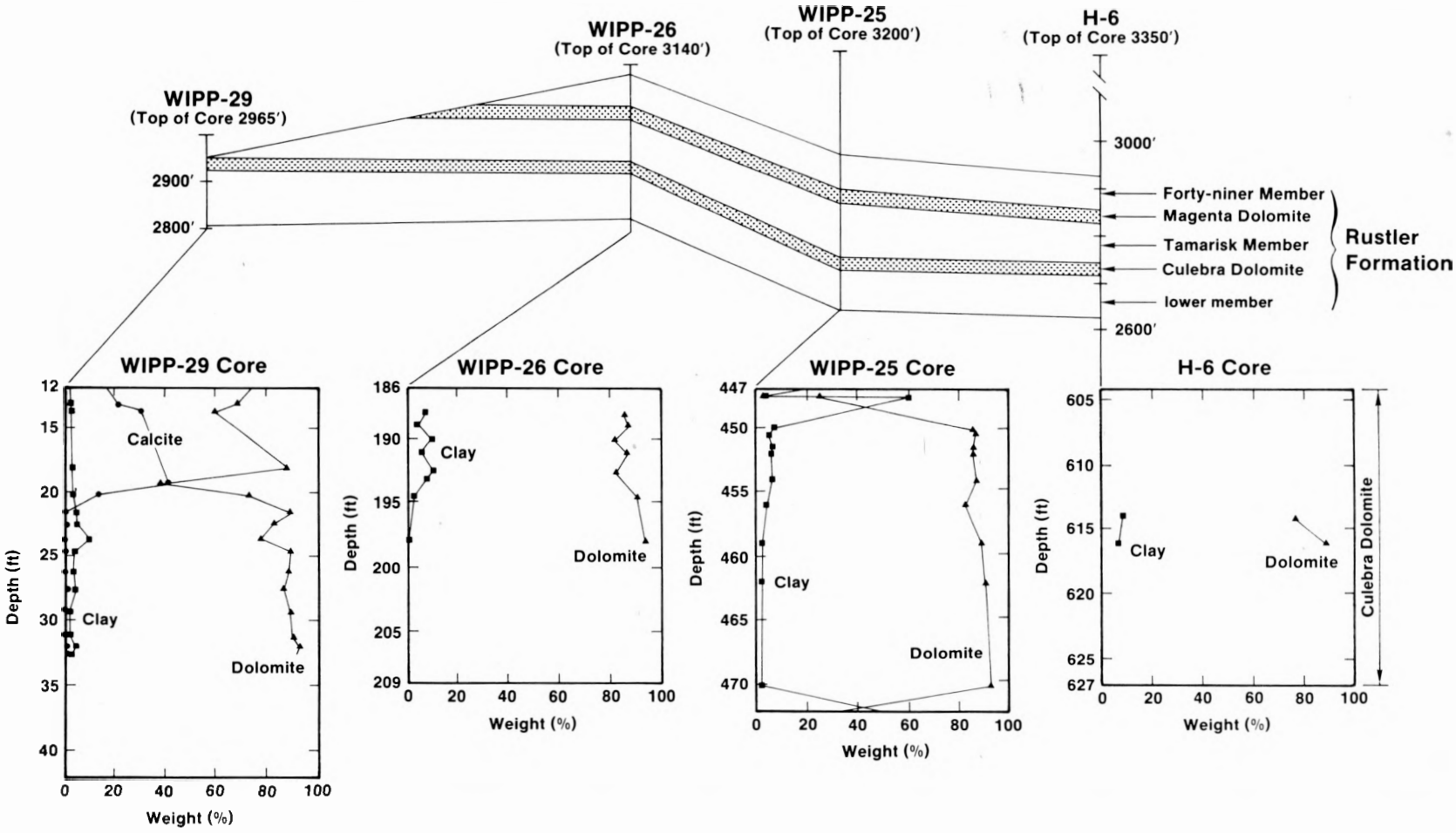

Figure V-31. Traverse Number One as Shown in Figure V-30.

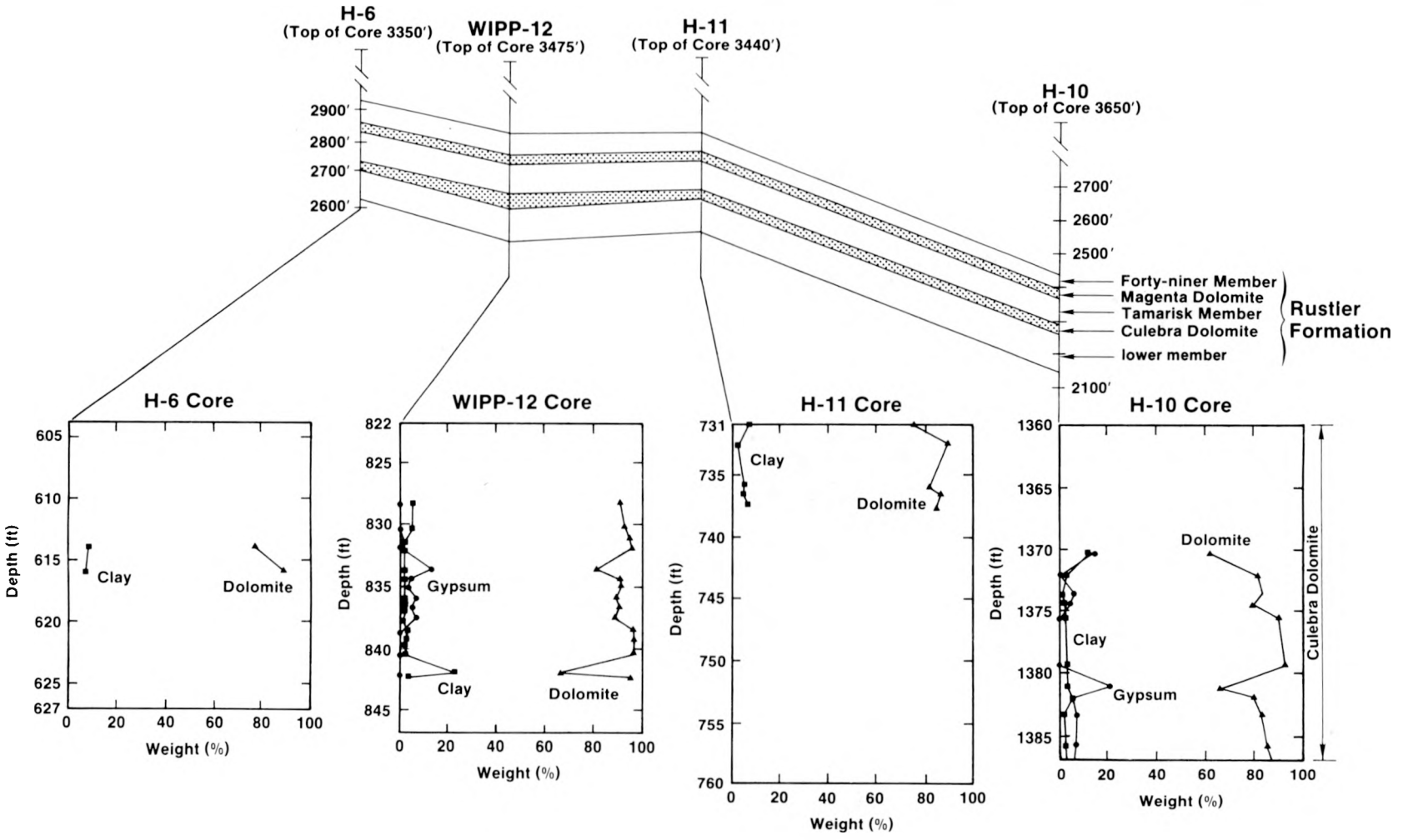

TRI-6342-492-0

Figure V-32. Traverse Number Two as Shown in Figure V-30.

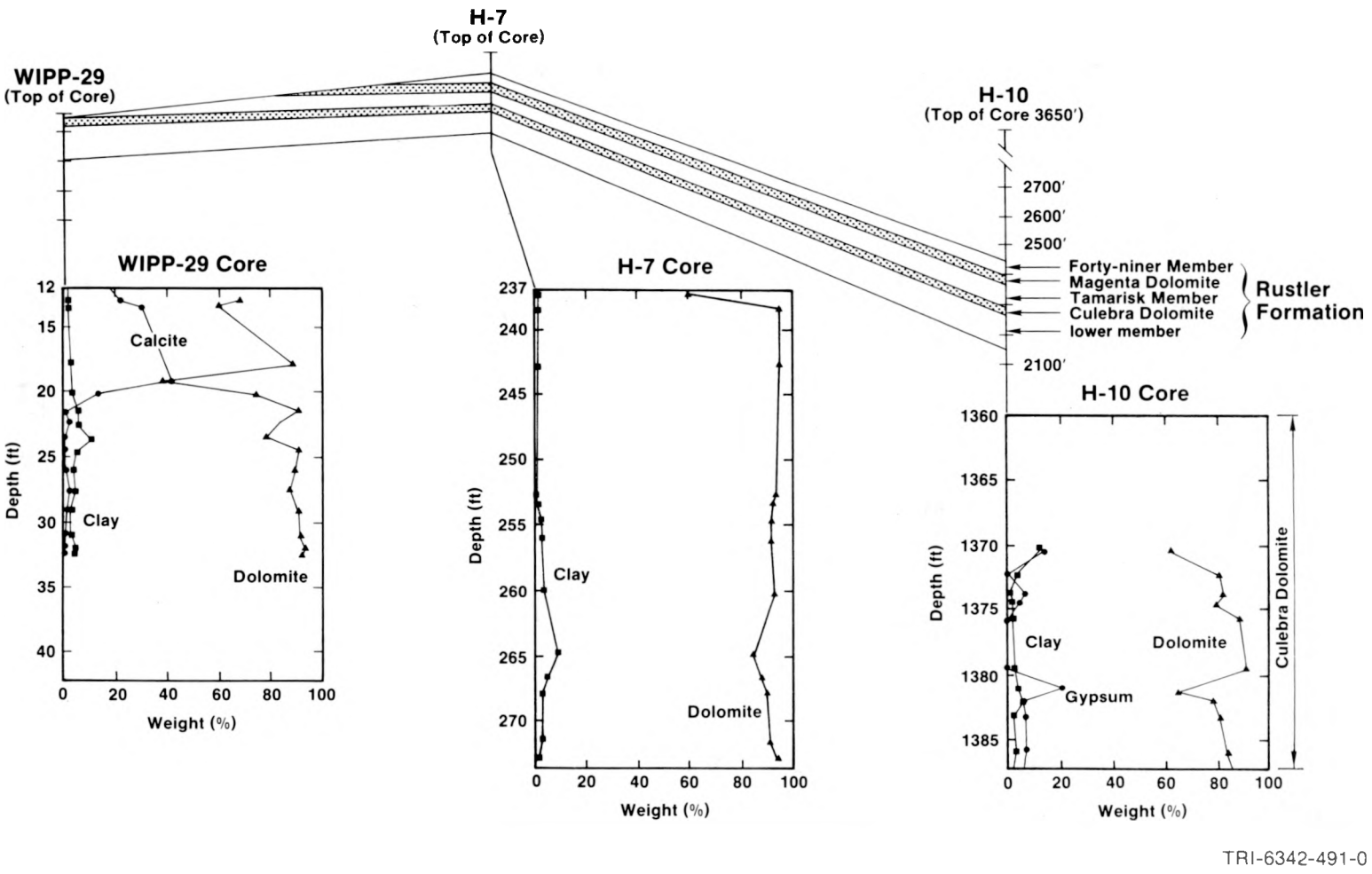

Figure V-33. Traverse Number Three as Shown in Figure V-30.

Discussion

The results of the mineralogical calculations of the previous section are rather hard to evaluate in tabular form or in the individual graphs of mineral abundance versus depth. In order to obtain a more comprehensive picture of both the vertical and horizontal variations of the major minerals in the eight cores examined in this study, three fence diagrams (Figures V-31 to V-33) of the Rustler Formation, which highlight the two dolomite members, Culebra and Magenta, were prepared, based on the three traverses indicated in Figure V-30. Within each fence diagram, the major minerals in each core are plotted beneath the location of the borehole.

Several conclusions can be drawn from the inspection of these fence diagrams. First, clay is present in all the cores, averaging around 3-5 weight percent of the total. Second, the average dolomite content of these samples is 85-90 weight percent, with the remainder usually taken up by quartz, clay, and gypsum. Third, where gypsum is present, it appears to replace dolomite, leaving the clay content constant. Fourth, several clay-rich seams are present in the Culebra.

The Culebra section of the WIPP-29 core is very shallow, and the presence of abundant calcite in the samples from this core is probably due to the calcitization ("dedolomitization") of dolomite by calcium-rich ground waters. The fact that calcite is more abundant near the top of the core adds weight to this argument. Calcite was also found in the WIPP-19 core (Sewards et al., 1991.) at the top of the Culebra unit. Small amounts of calcite may be present throughout the Culebra, principally close to water-bearing fractures. In all probability, all the calcite has formed by dedolomitization; it is unlikely that any of it is primary.

Gypsum is most abundant in the H-10 and WIPP-12 cores. There appear to be two gypsum-rich seams that correlate between these two cores. Incomplete sampling of the H-6 and H-11 cores, which lie in the vicinity of the aforementioned cores prevents confirmation of an areal trend. Gypsum is a very minor component in the remaining cores, all of which lie to the south and west of H-10 and WIPP-12.

VI. DOLOMITE COMPOSITIONS

The composition of dolomite in six different samples, five from the WIPP-12 core and one from the H6B core, was obtained using the electron microprobe (Appendix A). These compositions, listed in terms of component oxides and cations, are included in Table VI-1. The iron content in all five dolomites is quite low, the maximum being 0.23% FeO in sample WIPP-12 #1. The calcium to magnesium ratio for these samples, for six non-evaporite dolomites and for four other evaporite dolomites (Goldsmith and Graf, 1958) are plotted in Figure VI-1. It should be noted that the Ca/Mg ratios from Goldsmith and Graf (1958) were determined by X-ray diffraction methods rather than microprobe analysis; thus, any systematic error might invalidate the comparison with the Culebra samples.

Figure VI-1 shows that the Culebra Dolomite compositions have a Ca/Mg ratio that lies between that of other evaporite dolomites, which is usually less than 1.0, and that of non-evaporite dolomites, which lies above 1.1. Presumably, the brines that dolomitized the initial calcite deposits had a higher Ca/Mg ratio than is normal in an evaporitic environment; this may have been caused by the large non-marine (fluvial) water input into the Delaware Basin at the time of deposition of these sediments.

The Ca/Mg ratio in dolomites is important because, unless the assumption is made that the dolomite is ideal, the value of ΔG_f (the Gibbs free energy of formation) for dolomite depends on this ratio. Tardy and Gartner (1977) have developed an empirical method to calculate ΔG_f for carbonates based on compositional data. If order-disorder phenomena in the dolomites can be neglected, this method could be applied to calculate the free energy for the Culebra dolomites. An accurate value for the Gibbs free energy is essential for the calculation of phase equilibria in ionic solutions.

Since dolomite compositions were obtained for six samples representing only two cores, it is not really safe to assume that the compositions in other cores will be in the same range as those that were analyzed.

Table VI-1. Dolomite Compositions

No.	Sample ID	% CaO	s	% MgO	s	% FeO	s	n	Total
1	W12-1	30.66	0.27	21.09	0.59	0.23	0.09	7	51.98
2	W12-2	29.80	0.32	20.44	0.92	0.17	0.02	3	50.41
3	W12-9	28.59	0.44	20.07	0.28	0.11	0.11	29	48.77
4	W12-12	29.79	0.46	19.71	1.06	0.12	0.10	5	49.62
5	W12-16	29.83	0.51	20.78	0.53	0.23	0.06	4	50.84
6	H6B-4	30.12	0.26	20.03	0.26	0.16	0.08	5	50.41

Cations

Sample ID	Ca	Mg	Fe	Ca/Mg	Total
W12-1	1.019	0.975	0.006	1.045	2.000
W12-2	1.020	0.976	0.004	1.045	2.000
W12-9	1.010	0.987	0.003	1.023	2.000
W12-12	1.040	0.960	0.000	1.083	2.000
W12-16	1.013	0.981	0.006	1.033	2.000
H6B-4	1.037	0.959	0.004	1.081	2.000

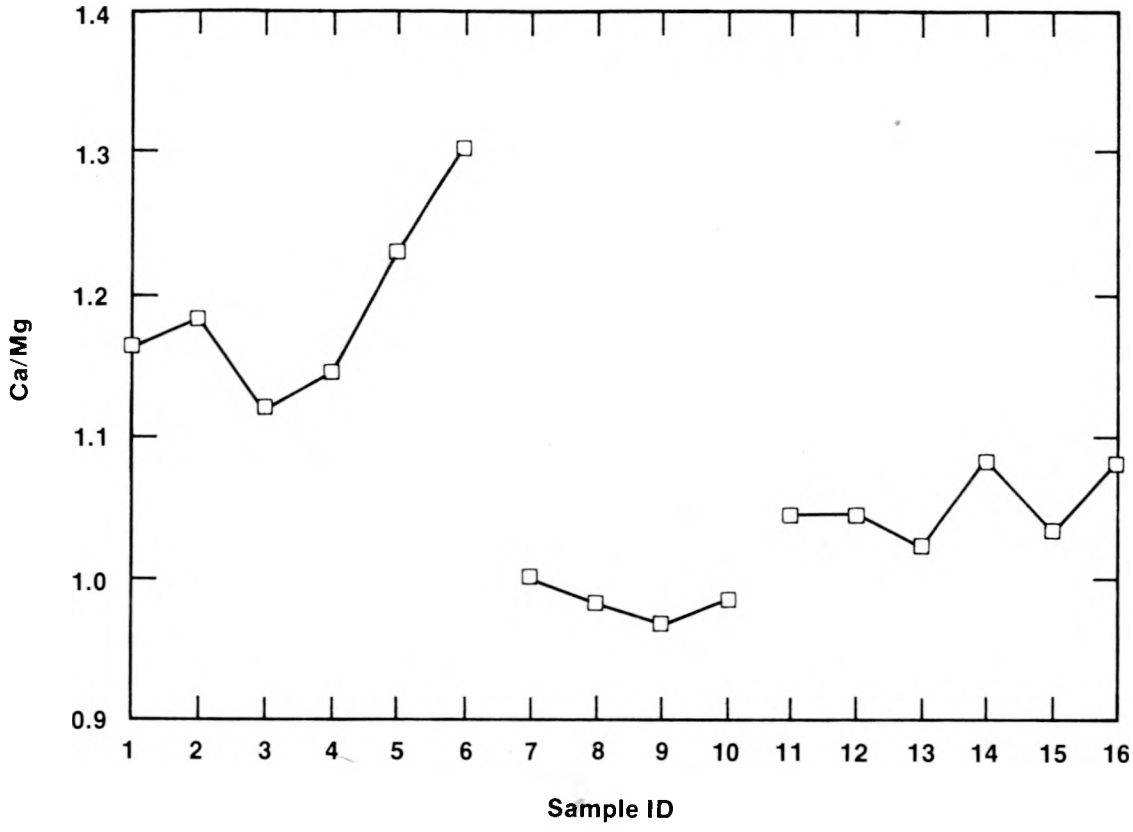

1	G-1322	Galena Platteville Formations, Ordovician, Oglesby, Illinois
2	G-1331	Edgewood Dolomite, Silurian, Pike County, Illinois
3	G-1181	Cogollo Formation, Cretaceous, Venezuela
4	G-379	Inglis Member, Moodys Branch Formation, Upper Eocene, Levy County, Florida
5	G-1055	Avon Park Formation, Middle Eocene, Levy County, Florida
6	G-1138	Funafuti (Pacific Island Core) Depth 840 Feet
7	G-1387	Anhydrite-Dolomite Rock, Permian, Yorkshire
8	G-1187	Salina Formation, Silurian, Michigan
9	G-1121	Evaporite Sequence, Saskatchewan
10	G-1374	Edwards Formation, Early Cretaceous, New Mexico
11	WIPP-12	#1
12	WIPP-12	#2
13	WIPP-12	#9
14	WIPP-12	#12
15	WIPP-12	#16
16	H-6B	#4

TRI-6342-478-0

Figure VI-1. Dolomite Compositions.

VII. CLAY MINERALOGY

Clay fraction separates (<2 micron) were obtained from three samples and analyzed by XRD using oriented mounts (Drever, 1973) to both identify the clay minerals present and determine the modes of each clay mineral. XRF analysis was used to determine the bulk composition of the clay separates. AEM was used to study the textural relationships of the clay minerals in one sample, H6B #3.

X-Ray Diffraction Analysis

X-ray diffractograms for four different treatments on oriented mounts (air-dried, glycolated, and heated to 400°C and 550°C) were obtained for the clay fractions of three samples: WIPP-12 #3, a clay-poor dolomite; WIPP-12 #16, a clay-rich dolomite; and H6B #3, a shale. These diffractograms are shown in Figures VII-1 to VII-3. In addition, the diffractogram of the glycolated (background removed) mount for sample H6B #3, which documents the presence of chlorite (Figure VII-4), and a random mount diffractogram for sample WIPP-12 #16 (Figure VII-5) are included.

CLAY MINERAL IDENTIFICATION

Since all three sets of diffractograms (Figures VII-1 to VII-3) are quite similar, and the clay minerals present are the same in all three, it is appropriate to discuss the clay minerals individually.

Illite

The presence of illite is indicated by the characteristic 001 and 002 peaks at 10.1A and 5.0A. The dioctahedral nature of this clay mineral can be inferred from the presence of a 060 peak at d=1.50A in the random mount for sample WIPP-12 #16 (Figure VII-4). The nature of the illite polytype cannot be determined from the random mount diffractogram because the presence of peaks of other clay minerals, as well as quartz, renders interpretation difficult.

The 001 peaks for this mineral are broad, indicating that the average crystallite size is small. Use of the Scherrer equation (Brindley, 1980) yields an average crystallite size of about 130A.

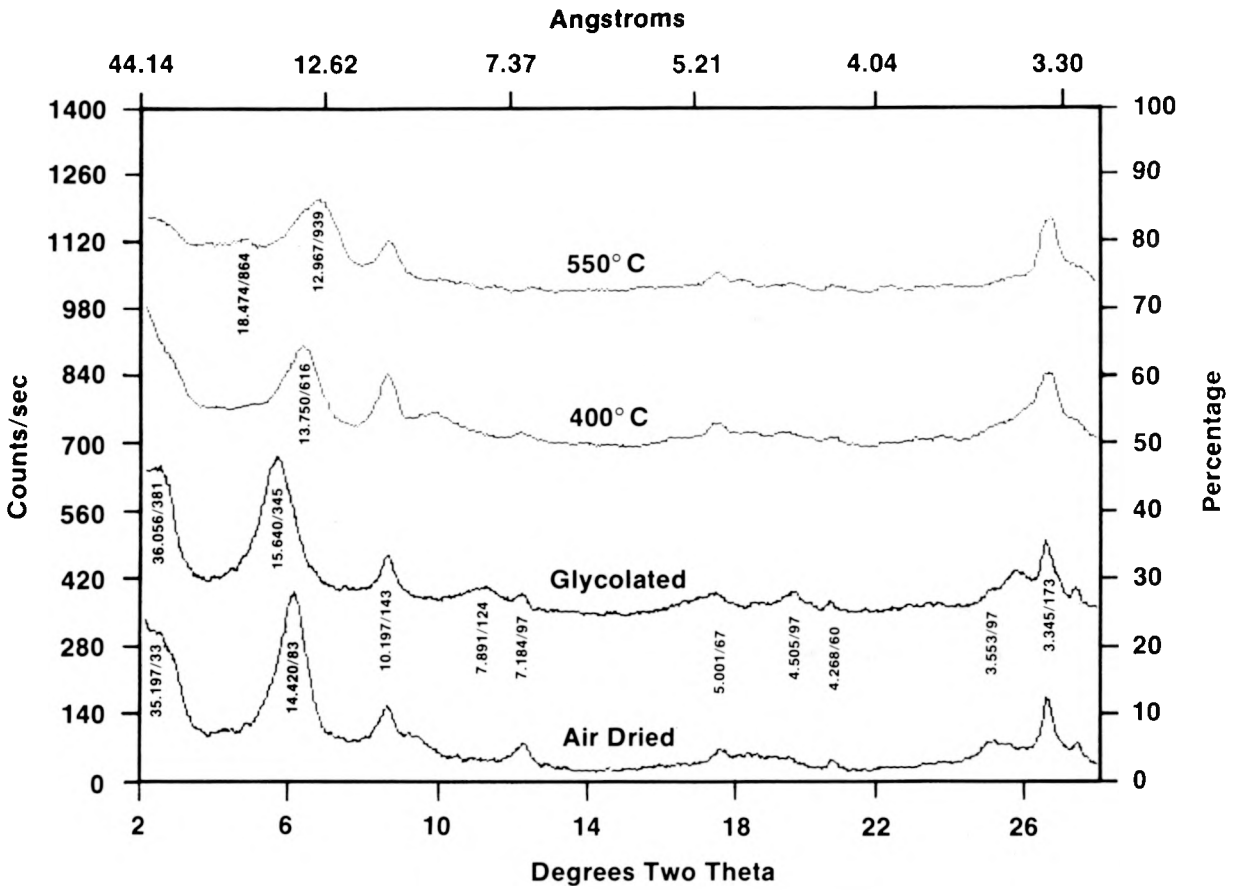

Figure VII-1. X-Ray Diffractogram for Sample WIPP-29-1. Peaks represent angstroms/counts per seconds.

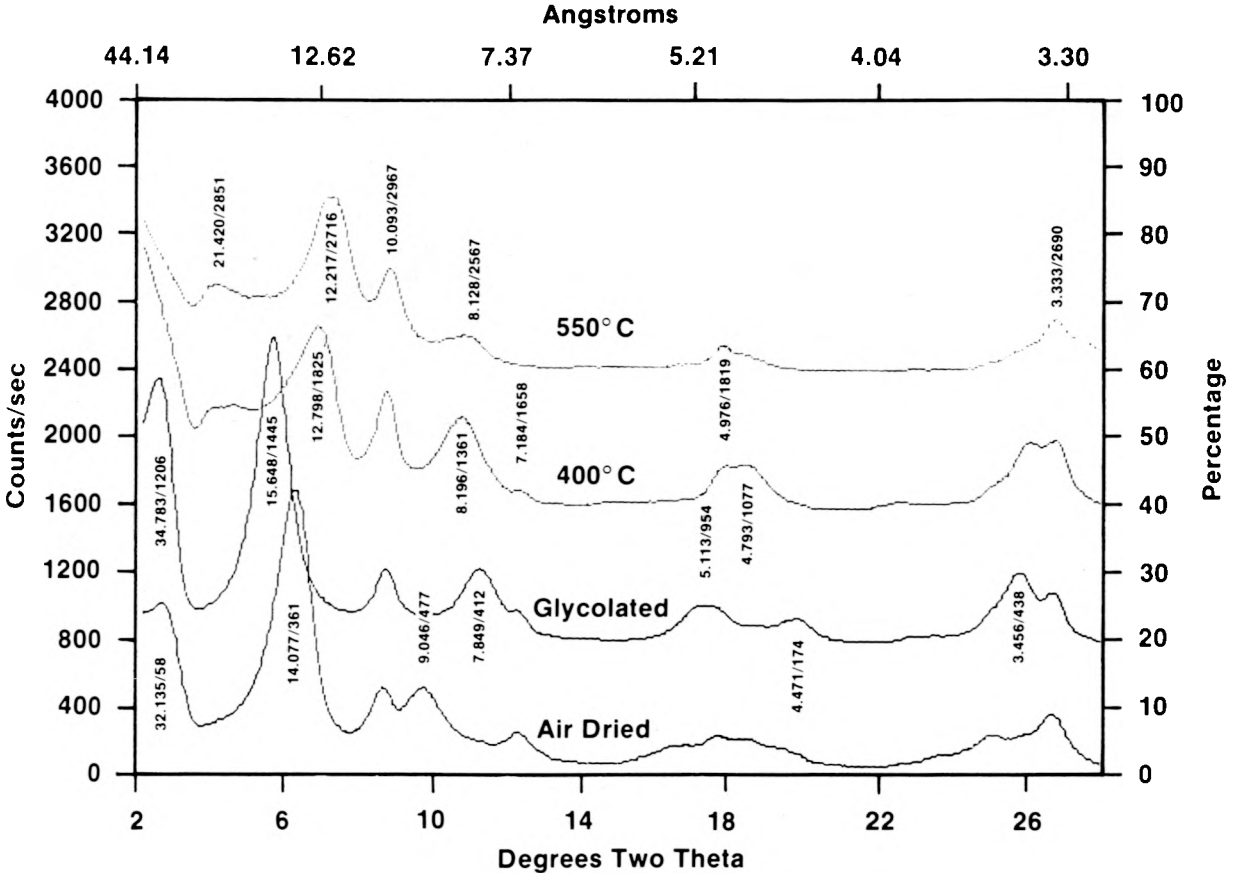

TRI-6342-498-0

Figure VII-2. X-Ray Diffractograms for Sample WIPP-12-16. Peaks represent angstroms/counts per seconds.

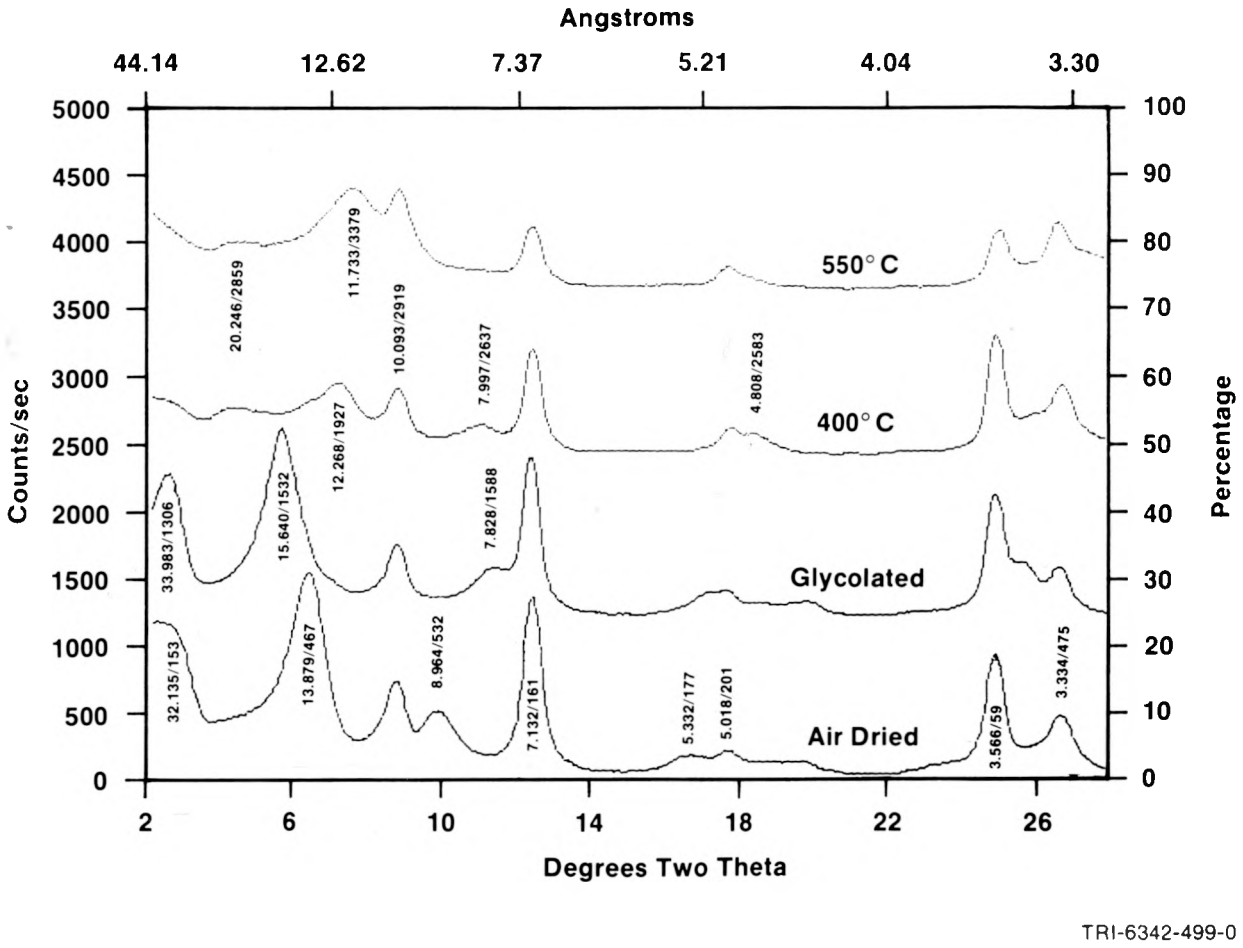

TRI-6342-499-0

Figure VII-3. X-Ray Diffractograms for Sample H6B-31. Peaks represent angstroms/counts per seconds.

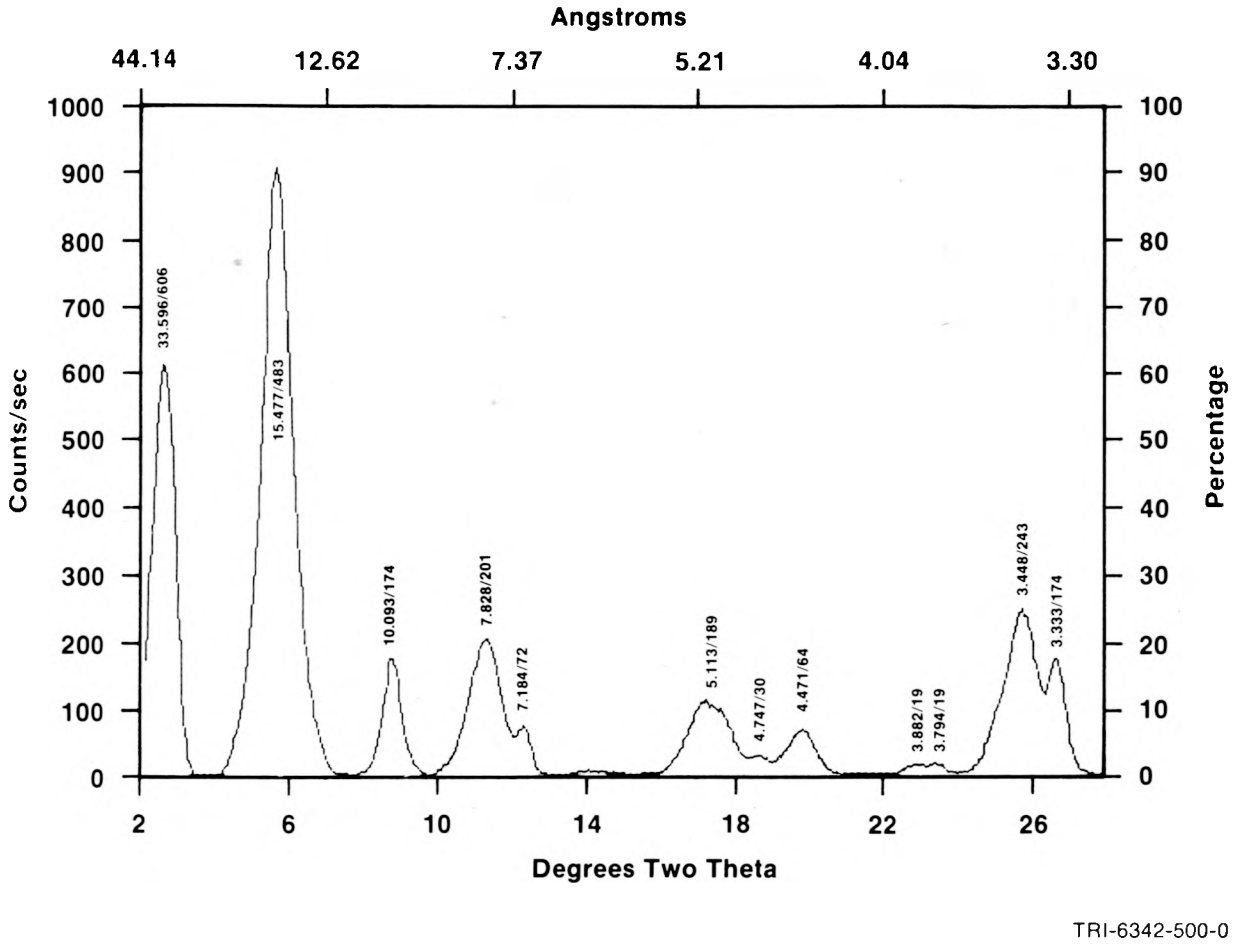

Figure VII-4. X-Ray Diffractograms of Glycolated Mount for Sample WIPP-12-16. Peaks represent angstroms/counts per seconds.

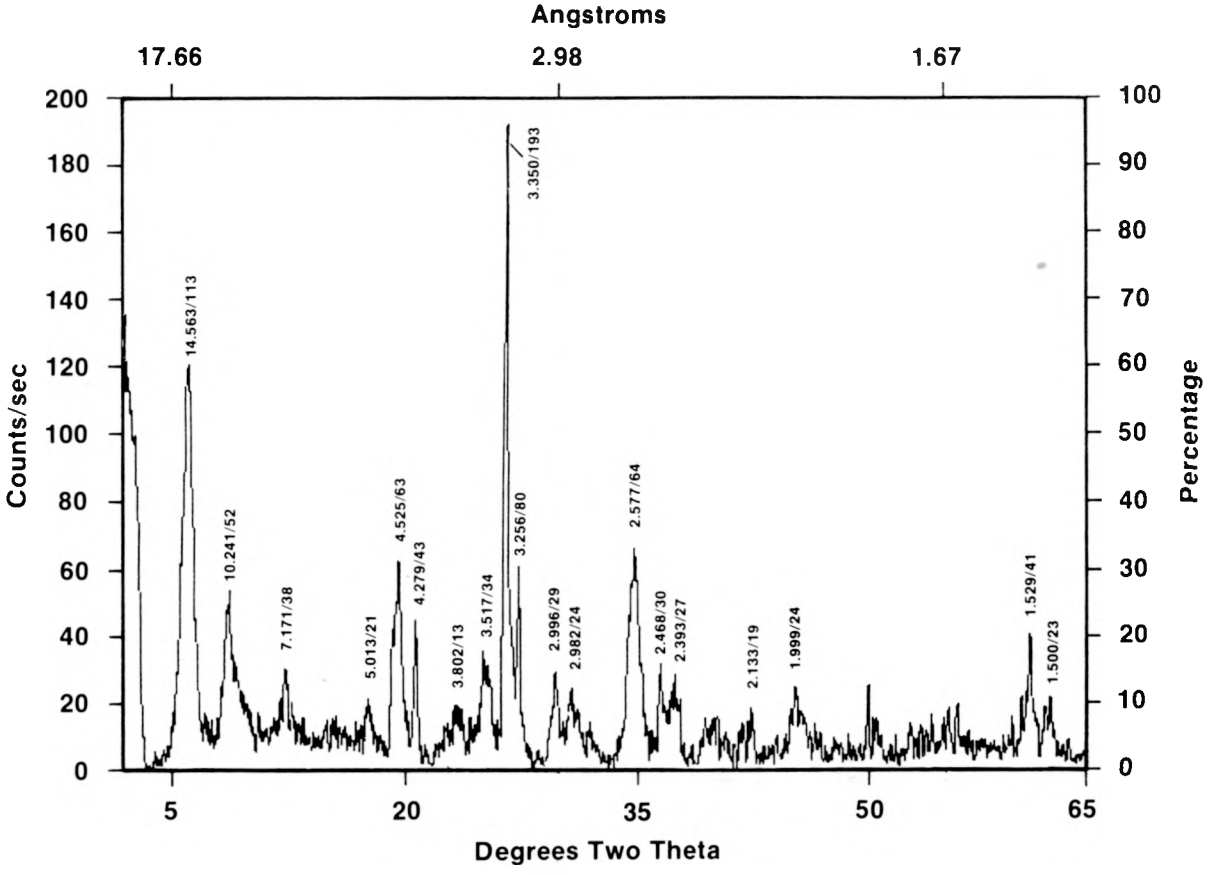

Figure VII-5. Random Mount Diffractogram for Sample WIPP-12-3. Peaks represent angstroms/counts per seconds.

Serpentine

Peaks at d=7.2A and d=3.55A indicate the presence of a 7A phase, which could be either kaolinite or serpentine. The fact that the intensities of these peaks are reduced by the 400°C treatment and destroyed by the 550°C treatment would seem to indicate that this mineral is kaolinite (Starkey et al., 1984). However, the results of analytical electron microscopy show that this is a magnesium-rich phase, which rules out kaolinite. Although exact compositional data have thus far not been obtained, it is probable that the mineral is a serpentine with a composition near that of an amesite, since this clay mineral has been found previously in evaporite clay mineral assemblages (Harville and Fritz, 1986; Braitsch, 1971). Average crystallite size, determined by the Scherrer equation, is 160A.

Corrensite

The superlattice peak at d=32.0A, which shifts to d=34.5A upon glycolation, indicates the presence of an ordered mixed-layer phase. The 002 peak (or interference peak between the 001 peaks of the two components), which has a d-spacing of 14A in the air-dried mount, shifts to 15.65A upon glycolation. This is midway between the d-spacing of 001 (glycolated) peak for a smectite (17.2A) and the d-spacing of a chlorite (14A); this suggests that the mixed-layer phase is a corrensite (ordered mixed-layer chlorite/smectite). The heat treatments collapse the smectite layers, causing the superlattice peaks to move to d=21.5A and the 002 peak to 12.2A, midway between the collapsed smectite peak (10A) and the chlorite peak.

Chlorite

The presence of chlorite in these samples is indicated by a small peak at d=4.75A. This is the 003 peak of chlorite and is best seen in the glycolated mount diffractogram for sample WIPP-12 #16 (Figure 42). The 001 chlorite peak is obscured by the broad corrensite peak at d=15.7A, although a slight asymmetry can be seen in this peak. Similarly, the 002 peak coincides with the 001 peak of serpentine, so the 003 peak is the only clue to the presence of chlorite.

Modal Analysis

Modal mineralogical calculations based on glycolated XRD patterns for clay mineral separates were performed (see Appendix B for details). The results of these calculations are listed in Table VII-1. In all these samples,

Table VII-1. Clay Mineral Modal Analysis

Sample	Corrensite	Serpentine	Illite	Chlorite
W12-3	58%	3%	34%	5%
W12-16	62%	3%	32%	3%
H6B-3	49%	28%	18%	5%

corrensite is the dominant clay mineral; illite is abundant; serpentine is abundant in one sample (H6B #3), and chlorite is a minor component in all samples.

BULK CLAY COMPOSITIONS

Clay separates (<2 micron) of the three samples listed in the previous section were analyzed by XRF to determine their compositions. These are listed in Table VII-2. It should be noted that the clay separate for sample WIPP-12 #3 has substantial amounts of quartz in it, as can be seen in the diffractograms in Figure VII-1. Thus, the value for SiO_2 is probably high with respect to the actual clay assemblage composition, and the values for the remaining oxides are correspondingly low. However, even taking this fact into account, it is hard to understand why the clay compositions of WIPP-12 #3 and WIPP-12 #16 are so different, given the fact that the clay mineral components determined by modal analysis are nearly identical. In particular, the value for MgO in sample WIPP-12 #16 is nearly twice that of WIPP-12 #3, whereas the value of K_2O in WIPP-12 #3 is twice that of WIPP-12 #16.

Analytical Electron Microscopy

Analytical Electron Microscopy was employed to examine microtomed sections of the clay fraction (air dried) of sample H6B #3 (see Appendix B for details of the methods and instrumentation used). Lattice fringe images of four clay minerals, with d-spacings of 7A, 10A, 14A and 33A, were obtained. These are shown in Figures VII-6 through VII-9; the corresponding energy dispersive spectrometer (EDS) spectra are shown in Figures VII-10 through VII-13. Figures VII-6 and VII-10 correspond to the 7A phase: the lattice fringe image shows a well-ordered basal periodicity and well defined morphology with good crystalline structure for up to 400A in basal direction. The spectrum indicates the presence of Mg, Al, and Si, which confirms the identification of the 7A phase as serpentine.

Figure VII-6. High-Resolution Lattice Fringe Image of Serpentine from Sample H6B-3.

Table VII-2. Clay Separate Compositions

Sample ID	SiO_2	Al_2O_3	MgO	FeO	CaO	K_2O	Na_2O	Total
W12-3	45.94	14.88	13.57	2.02	0.29	3.95	0.44	81.09
W12-16	42.42	14.14	24.58	2.52	0.39	2.05	0.73	86.83
H6B-3	42.79	16.27	22.83	3.03	0.09	2.19	0.72	87.92

The lattice fringe image for the 10A phase (Figure VII-7) shows the typical morphology of an illite (Ahn and Peacor, 1986). Of the three clay minerals imaged, these illites have the largest size in the basal direction (>400A). The spectrum (Figure VII-11) indicates the presence of Al, Si, and K, with minor amounts of Mg and Fe. The potassium peak is, however, somewhat low compared to that of typical illite spectra; this may be due to elemental loss (Mackinnon and Kaser, 1987) or an atypical composition.

The 14A phase (Figures VII-8 and VII-12) crystallites have smaller basal dimensions (<150A), but form well-ordered crystallites in the c-axis dimension. The spectrum suggests that the mineral is an Fe-rich chlorite.

Observations on samples intercalated with laurylamine hydrochloride (Lee and Peacor, 1986), for which mixed-layer 14A and 18A basal spacings occur in corrensite, are shown in Figure VII-9. In general, corrensite expanded layers are very difficult to image using high resolution transmission electron microscopy techniques because of rapid damage rates and poor diffraction contrast. Nevertheless, examples of image contrast consistent with intercalated corrensite are shown. Regular alteration of 14A and 18A layers is often restricted to two or three repeats, and in some instances, the variable extent of layer expansion due to intercalated laurylamine hydrochloride is readily seen. The presence of these very thin, or "fundamental," particles is evidence that interparticle diffraction may be responsible for the XRD peaks for corrensite (Nadeau et al., 1984).

A typical EDS spectrum for this phase is shown in Figure 51; it shows that the phase contains primarily Si, Al, Mg, and Fe.

Discussion

Clay minerals in evaporite environments have been discussed extensively by Bodine and coworkers (Bodine and Standaert, 1977; Bodine, 1978, 1983, 1985; Bodine and Madsen, 1985). In some ways, their work does not apply too well to

Figure VII-7. High-Resolution Lattice Fringe Image of Illite from Sample H6B-3.

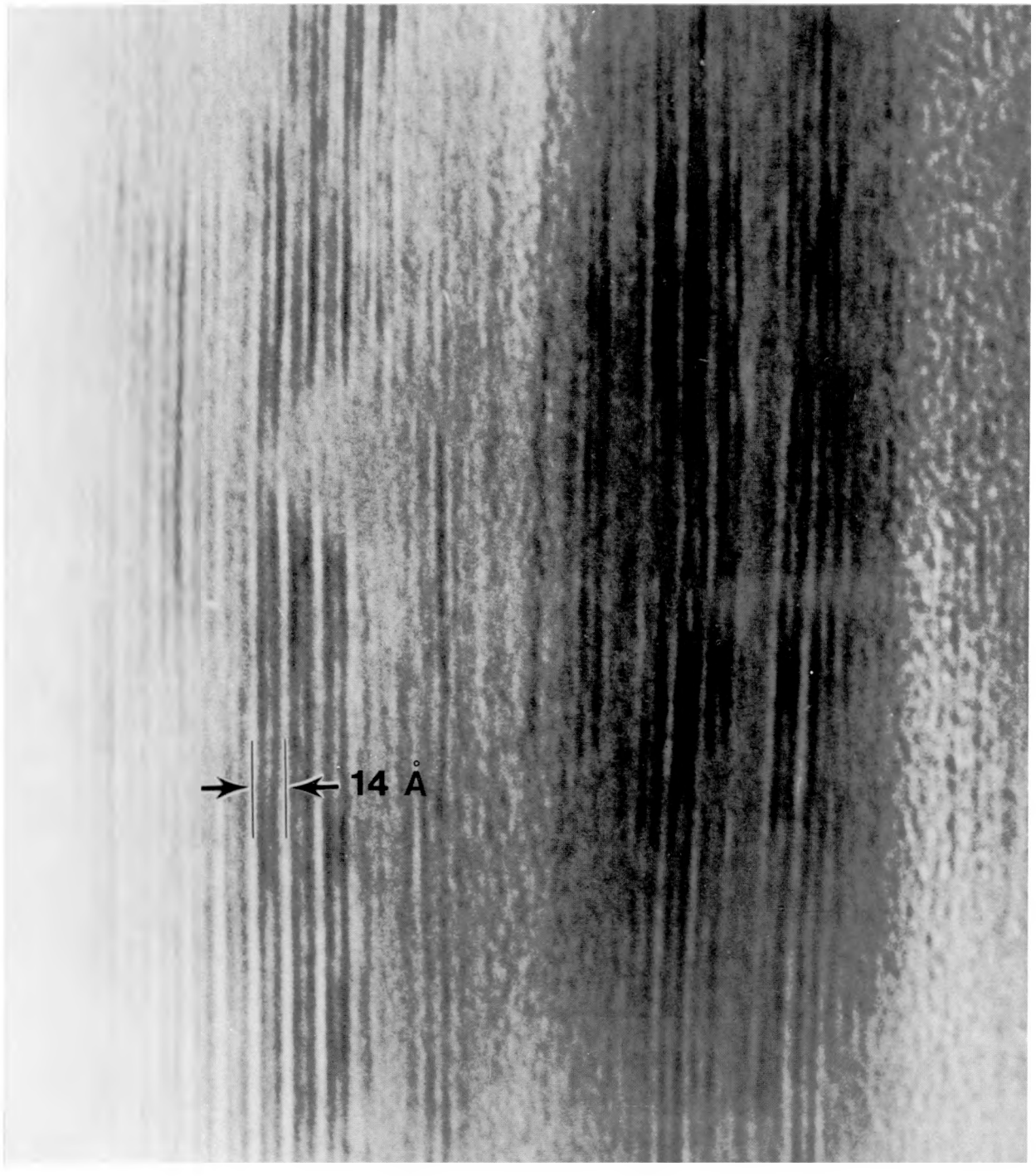

Figure VII-8. High-Resolution Lattice Fringe Image of Chlorite from Sample H6B-3.

Figure VII-9. High-Resolution Lattice Fringe Image of Corrensite from Sample H6B-3.

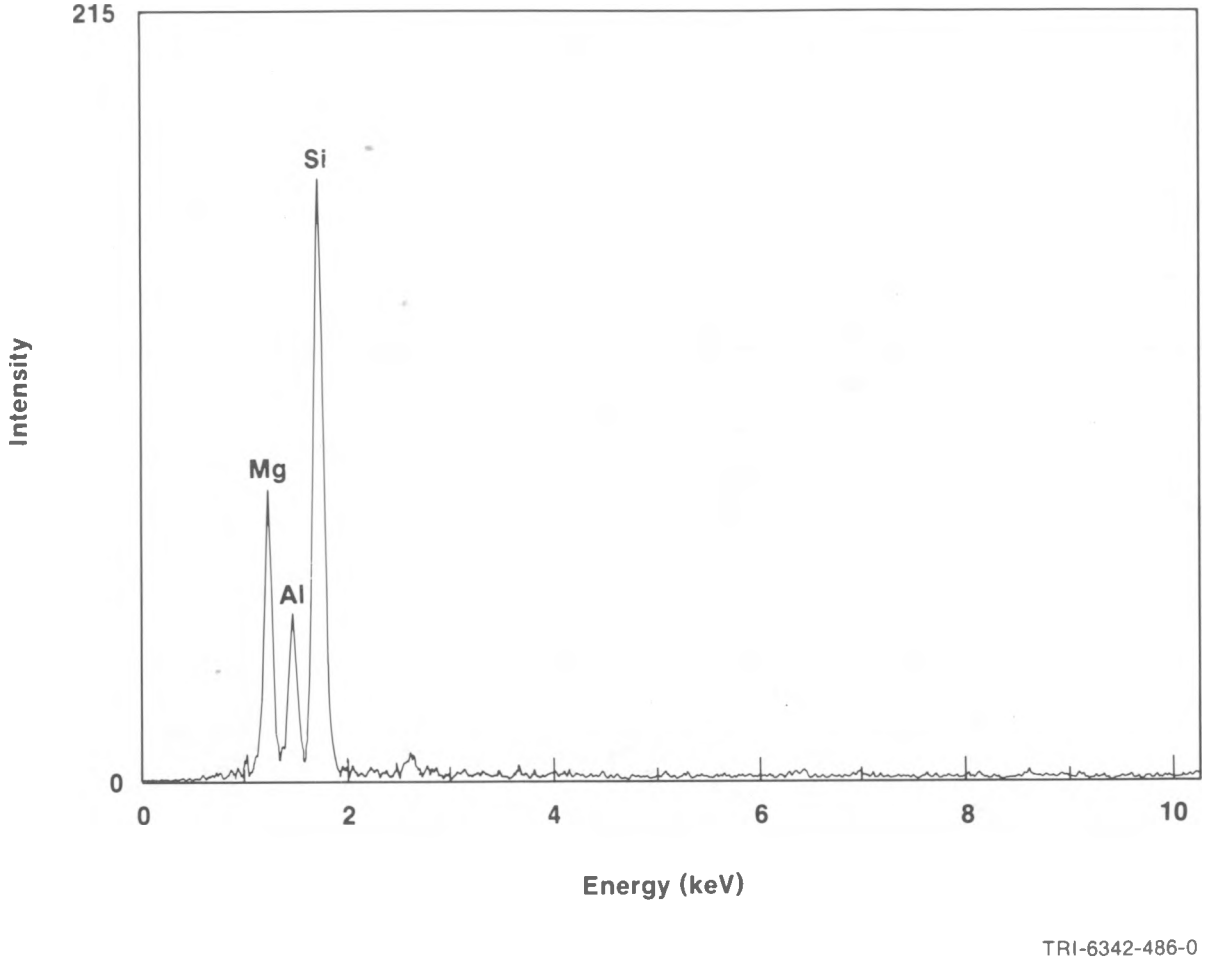

Figure VII-10. EDS Spectrum for Serpentine.

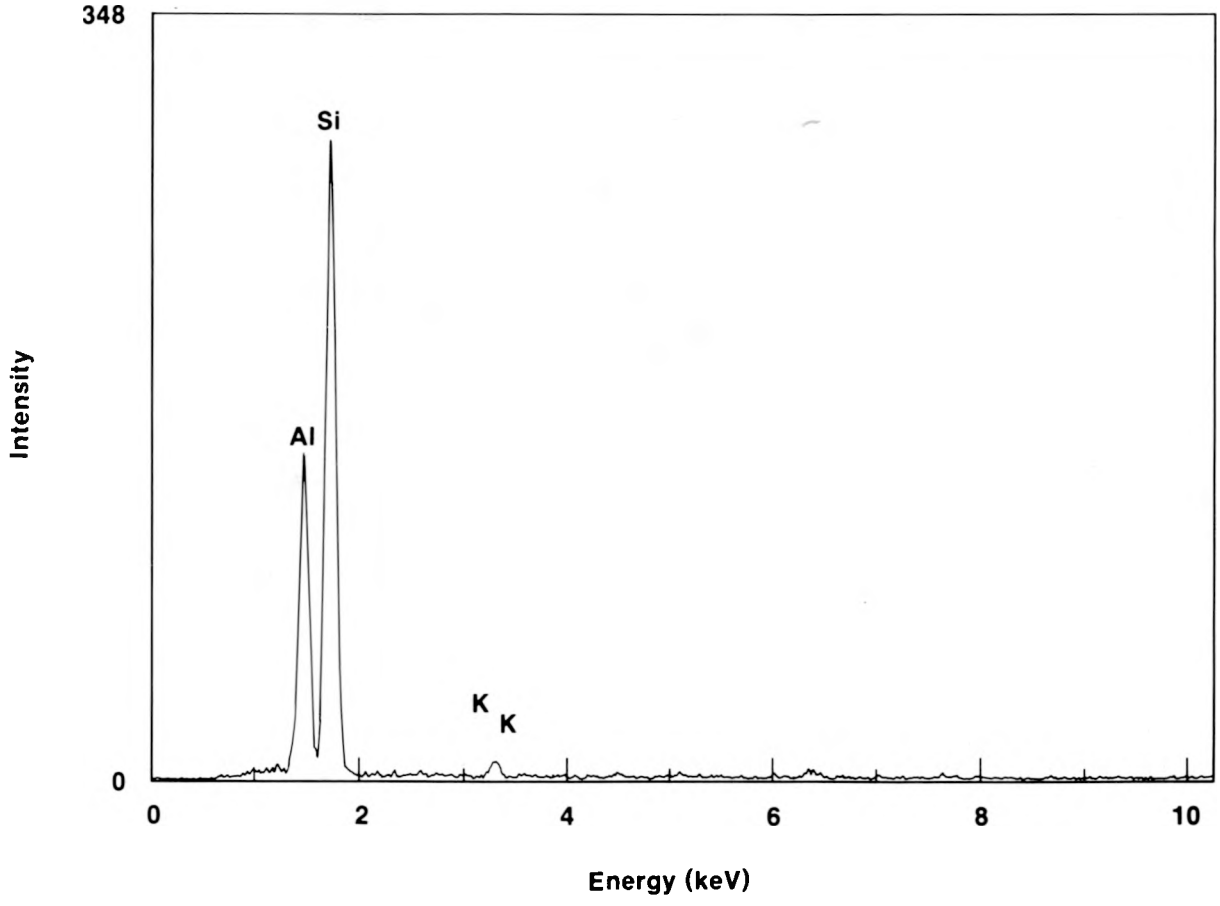

Figure VII-11. EDS Spectrum for Illite.

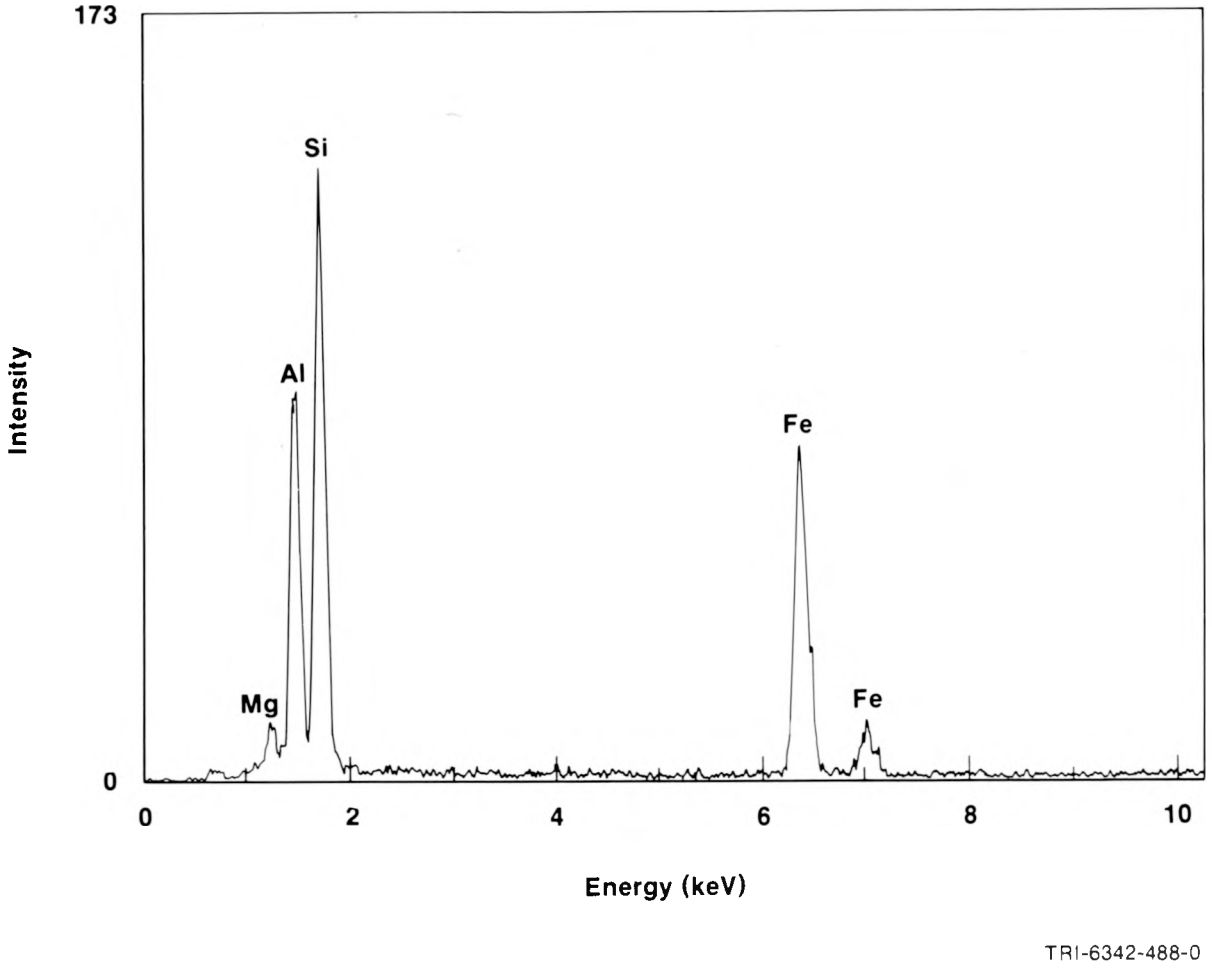

Figure VII-12. EDS Spectrum for Chlorite.

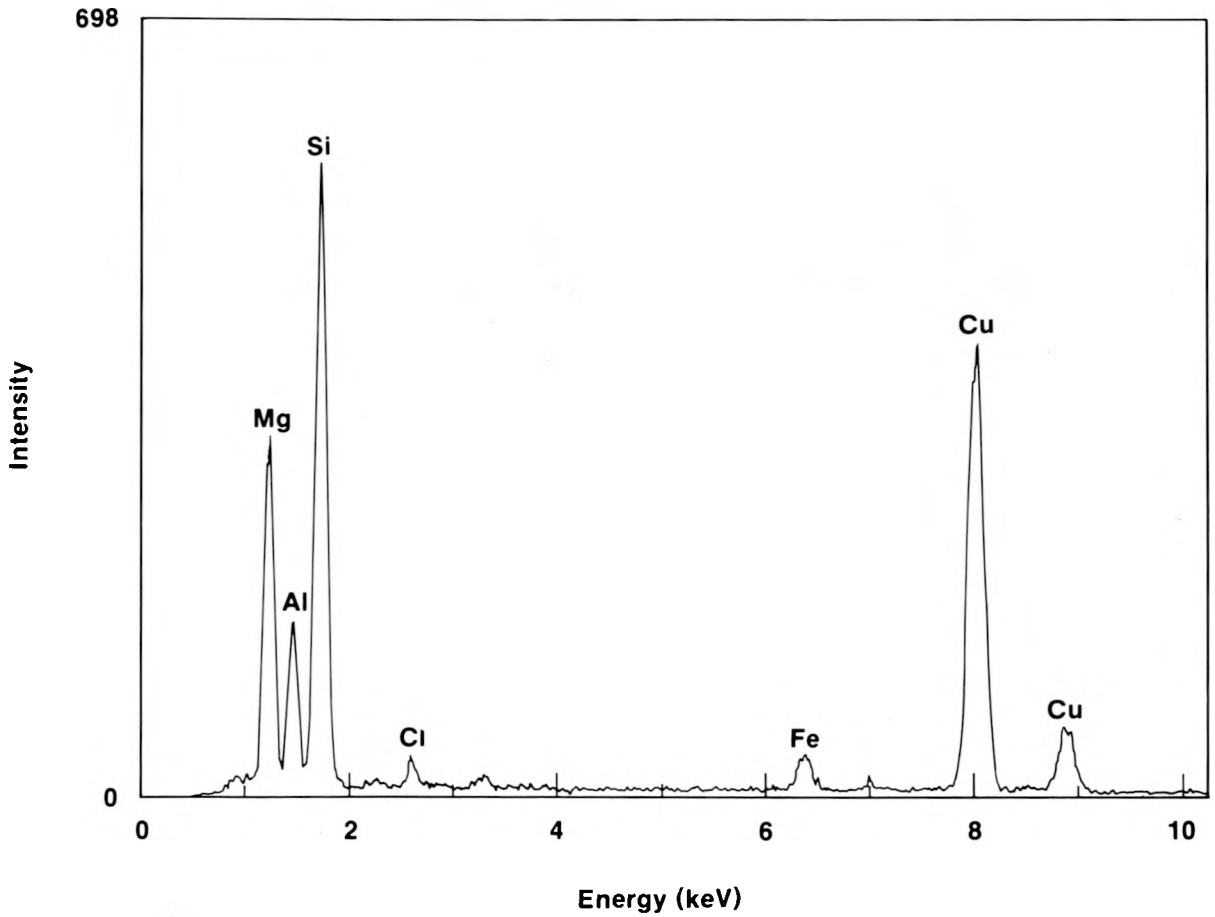

TRI-6342-489-0

Figure VII-13. EDS Spectrum for Corrensite.

the clay minerals in the Culebra Dolomite, because the Rustler Formation was never buried as deeply as the formations from which Bodine and coworkers took their samples, and temperature effects are therefore not as important. Sewards et al., 1991 studied the clay minerals of the Rustler Formation in detail, so this report merely summarizes the results of that work.

Palmer (1981) concluded that detrital clay minerals that were deposited into the Permian Delaware, Midland, and Palo Duro Basins include dioctahedral smectite, illite and mixed-layer illite/smectite, kaolinite, and clay chlorite.

Because the interlayer space of illite is fixed with potassium ions, this phase is a relatively stable one, especially at low temperatures. Even in an environment that, being very magnesium rich, is clearly out of the stability field for illite, illite crystallites apparently do not react with the pore fluid that surrounds them; the crystallites we see today are probably essentially unchanged from those that were deposited in Permian times.

Dioctahedral smectite, which is a far more reactive phase than illite, undergoes a more radical transformation: the pore fluids in these sediments constitute an "infinite reservoir" for magnesium. This magnesium replaces aluminum in the original smectite octahedral layers, while aluminum replaces silicon in the tetrahedral layers; concurrently, brucitic hydroxide layers are deposited in some of the interlayer spaces. The result is a mixed-layer chlorite/smectite; if the ratio of chlorite to smectite layers is 1:1 and stacking sequence is ordered, the result is corrensite.

Mixed-layer illite/smectite would undergo a similar transformation. Those layers not fixed by potassium (the smectite layers) would take up magnesium from the pore fluid; some of the interlayer spaces would accept brucitic hydroxide layers, while the illite layers would remain essentially unchanged. The result would be a mixed layer illite/smectite/chlorite. Reynolds (1980) has calculated theoretical diffractograms for mixed-layer illite/smectite/chlorite. These diffractograms are very similar to diffractograms of mixed-layer chlorite/smectite, provided the percentage of illite layers is small; so it would not be possible, based on XRD analysis alone, to determine whether this phase is present.

Serpentine is formed by direct transformation from kaolinite: magnesium replaces some of the aluminum in the octahedral layer, while aluminum replaces some of the silicon in the tetrahedral layer in order to maintain the charge balance. The result is a serpentine with a composition similar to that of amesite.

Clay chlorite deposited into a brine with high magnesium activity would presumably not react too extensively, since it is already a high magnesium phase.

Sewards et al., 1991 conclude, based on the presence of authigenic quartz and potassium feldspar in Rustler Formation samples, plus textural evidence from lattice fringe images obtained on the AEM, that these reactions occurred layer by layer (Bethke and Altaner, 1986): i.e., tetrahedral and octahedral layers are not destroyed; their composition is altered, but the bulk volume of clay remains essentially constant.

The fact that corrensite is the dominant phase in the Culebra samples is important. Corrensite has a high CEC and high surface area, thus it is able to sorb radionuclides very efficiently in the event of a low pressure breach in the WIPP facility. Although the clay minerals of only three samples were investigated, the results of Sewards et al., 1991 show that mixed-layer chlorite/smectite is the dominant clay phase throughout the Rustler Formation, so it is reasonable to suggest that the same is true in the Culebra unit. This is to be expected, since corrensite forms from a dioctahedral smectite precursor, and this is almost always the most abundant product of weathering (Blatt, 1982).

There is, however, a discrepancy between the results of the quantitative XRD analysis and the results of the AEM investigation of sample H6B #3. In that sample, the XRD results show that the sample contains approximately 50% corrensite. When imaging was attempted on the AEM, it was extremely difficult to find any corrensite at all; the dominant phases appeared to be serpentine, illite, and chlorite. Klimentidis and Mackinnon (1986) have noted a similar discrepancy while attempting to image mixed-layer clay minerals.

VIII. PETROGRAPHY

Most of the observations in the following section are based on samples from a single drill core, WIPP-12. This core yielded a large number of relatively massive samples that illustrate the range of mineralogical and textural characteristics typical of a vertical section through the Culebra Dolomite. Attention was primarily focused on features in the Culebra Dolomite that might preserve a record of, or ultimately control, its permeability and reactivity to past, present, and future through-going fluids.

Although most samples examined under the microscope display a fine-grained mosaic of dolomite crystals, significant variations occur in: (1) the size, shape, color, etc. of the dolomite crystals; (2) the relative abundance of quartz, clay, gypsum, and other phases in the dolomite; (3) the nature and distribution of organic material; (4) the abundance and character of fractures and fracture fillings; and, (5) the abundance, size, and textural characteristics of vugs and holes in the dolomite. Most of the heterogeneities are spatially interrelated even though they undoubtedly reflect variable amounts of primary depositional, digenetic, and postdepositional (dissolution-reprecipitation, etc.) processes.

The following discussion will be divided into two main parts. The first will be a discussion of the mineralogical and textural characteristics of "typical" massive dolomite. The second part will focus on the nature and distribution of vugs, holes, and fractures within the Culebra Dolomite.

Characteristics and Variations in "Typical" Culebra Dolomite

Typical Culebra Dolomite samples consist of domains or layers dominated by relatively pure, massive dolomite separated by domains or layers with quartz and clay-rich dolomite (Figure VIII-1). The thickness and relative purity of the layers are extremely variable. Clay-rich layers range from discontinuous lenses, less than 1 mm thick, to continuous laminae, several centimeters in thickness. Clay-rich layers typically contain from approximately 5 to 15 or 20 percent quartz and clay, whereas massive dolomite typically contains less than 3 percent quartz and clay. Both quartz/clay-rich and massive dolomite layers are cut to varying degrees by fractures and vugs (see below).

MASSIVE DOLOMITE

Massive dolomite domains in the Culebra Dolomite are characterized by nearly equigranular mosaics of dolomite crystals. Individual grain boundaries are generally not visible in transmitted light because of the fine grain size and

the high birefringence of the dolomite crystals (Figure VIII-2). Scanning electron microscope images of dolomite reveal that grains are subhedral rhombs with impurities (clay, organic matter) concentrated on the boundaries (Figure VIII-3). Even massive dolomite domains contain isolated local pods and lenses of clay minerals (Figure VIII-4). Coarse mica phases are also present and include muscovite, biotite, and iron-rich and iron-poor chlorite.

Two main textural varieties of massive dolomite domains have been identified in the Culebra samples. The first is characterized by extremely fine-grained dolomite with relatively abundant interstitial fine black material interpreted to be primarily of organic origin. At high magnification, these domains are characterized by a heterogeneous, slightly impure, appearance that is somewhat similar to the clay-rich layers (Figure VIII-5). However, XRD and electron microprobe analysis have failed to reveal any significant clay or mica component within these domains; therefore, their appearance is interpreted to reflect primarily the interstitial organic material. The second textural variety consists of slightly coarser dolomite, little or no interstitial black (organic?) material, and abundant fine vugs. These organic-poor domains are generally characterized by a homogeneous, lighter colored, cleaner appearance than the organic-rich regions (Figure VIII-6).

Boundaries between the clean dolomite and organic-rich dolomite regions are irregular. They are typically somewhat lobate in form and commonly intersect bedding at relatively high angles. Figure VIII-7, VIII-8, VIII-9 illustrates a variety of clean/organic-rich dolomite boundaries within massive dolomite.

Several lines of evidence suggest that the cleaner, vuggy dolomite domains may be secondary, perhaps representing dissolution and reprecipitation or fluid interaction with the original organic-rich dolomite. Lobes of clean, organic-poor dolomite are commonly aligned along fine fractures within the massive dolomite (Figure VIII-10). Other microfractures are surrounded by selvages of clean dolomite within a generally organic-rich subdomain (Figure VIII-11). In some cases, fractures and vugs with clean dolomite selvages are surrounded by dark halos of concentrated organic material, suggesting that the dark halos may represent a type of insoluble residue (Figure VIII-12, VIII-13).

It should be noted that dissolution experiments with a number of dolomite samples yielded a dark black, almost greasy insoluble residue. The dark black color gave way to a brown color, typical of clay-rich insoluble residues, upon prolonged heating. This dark black component of the insoluble residue is interpreted to be the organic component associated with primary dolomite and with some clay-rich layers.

Figure VIII-1. Sample W12-9. Massive, vuggy dolomite grading into a clay-rich layer at one end of section. (FOV = 12.8 x 16mm)

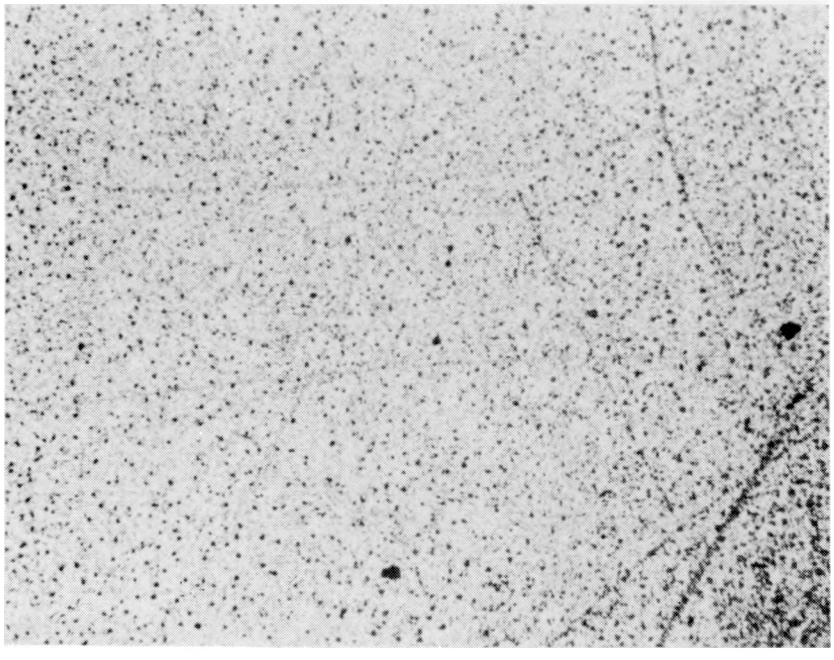

Figure VIII-2. Sample W12-4. Massive dolomite domain. (FOV = 12.8 x 16mm)

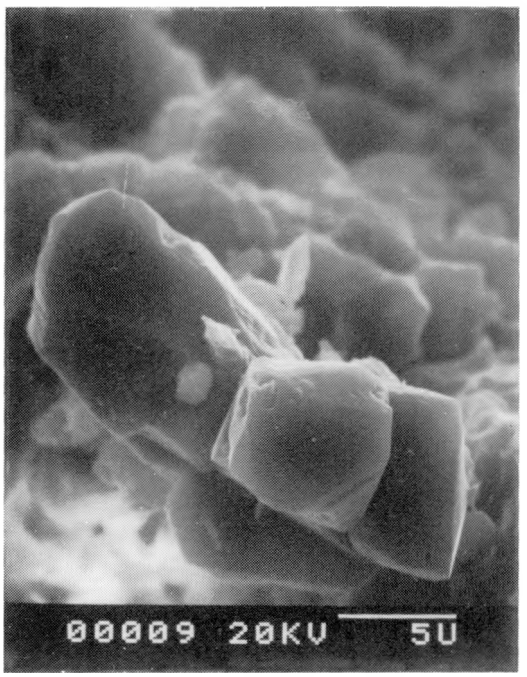

Figure VIII-3. SEM Micrograph of Dolomite Crystals.

Figure VIII-4. W12-1 Clay-rich lens in massive dolomite.

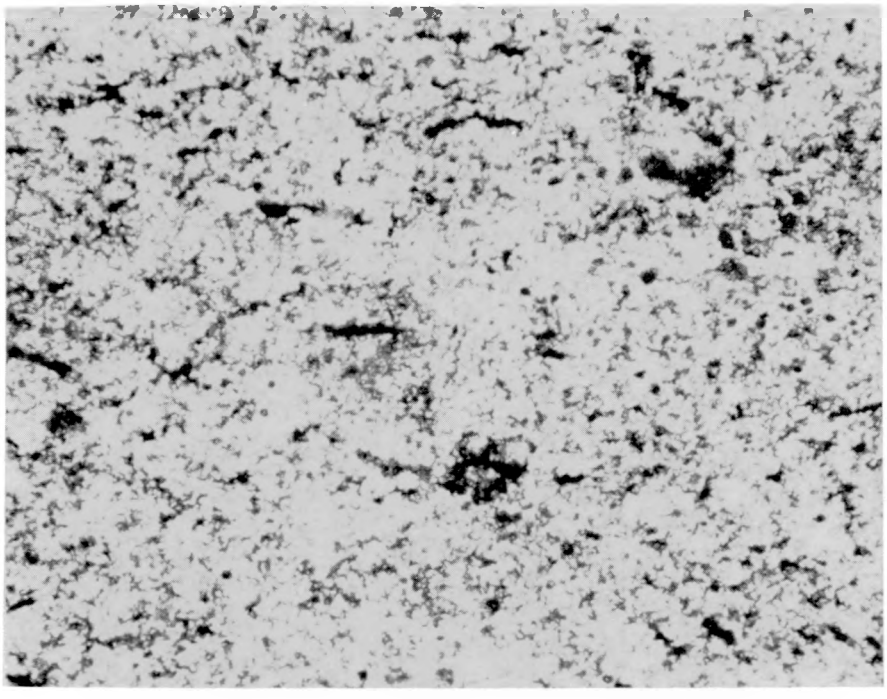

Figure VIII-5. Sample W12-2. Fine-grained massive dolomite with interstitial black material interpreted to be of organic origin. (FOV = 2.7 x 3.4mm)

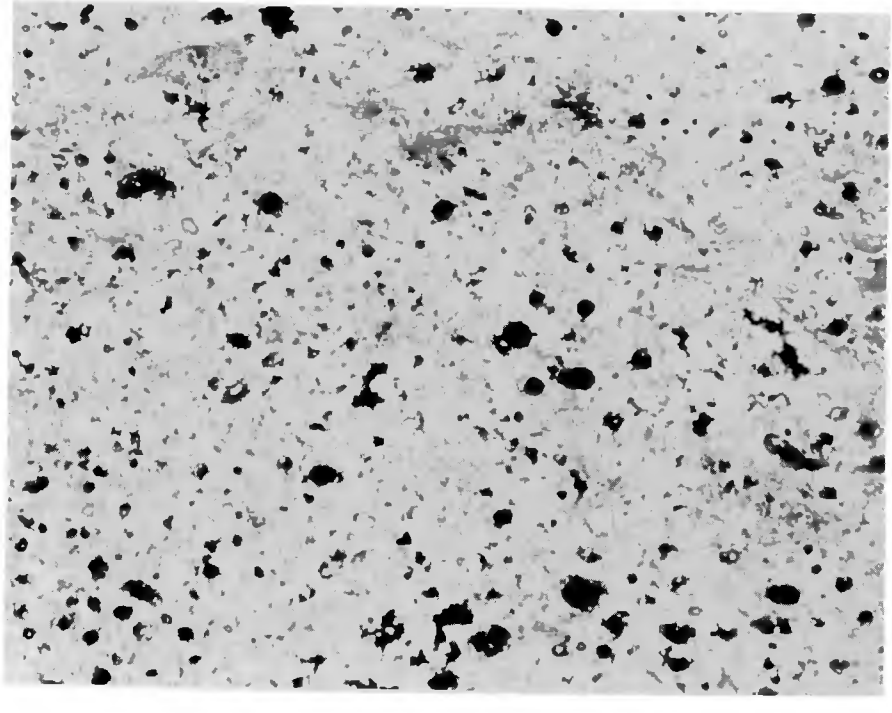

Figure VIII-6. Sample W12-2. Clean, coarse grained, vuggy dolomite. (FOV = 2.7 x 3.4mm)

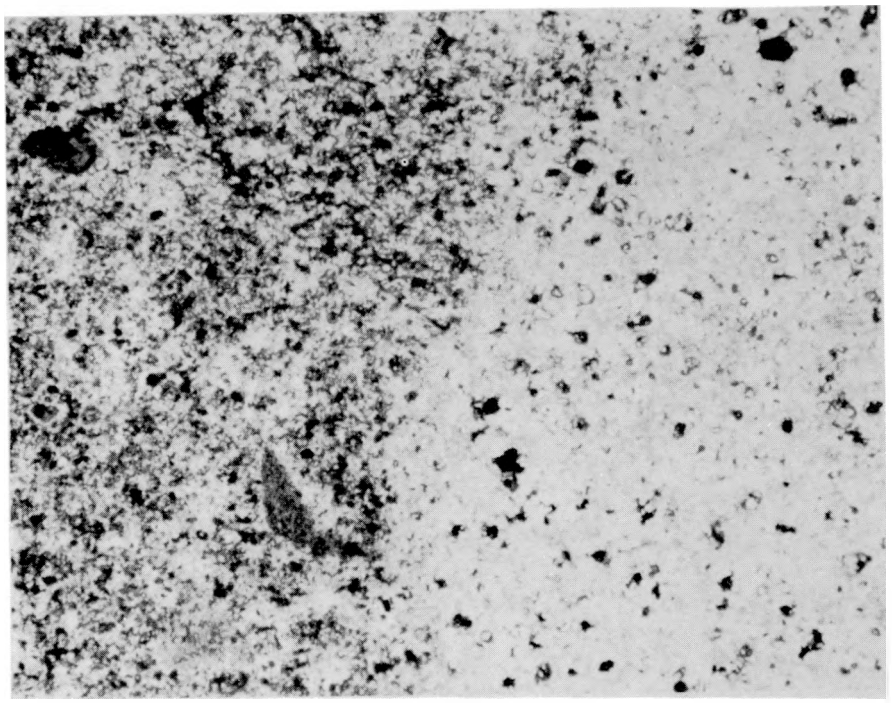

Figure VIII-7. Sample W12-2 View A. Boundary between organic-rich dolomite and clean, vuggy dolomite within a massive dolomite domain. (FOV = 2.7 x 3.4mm)

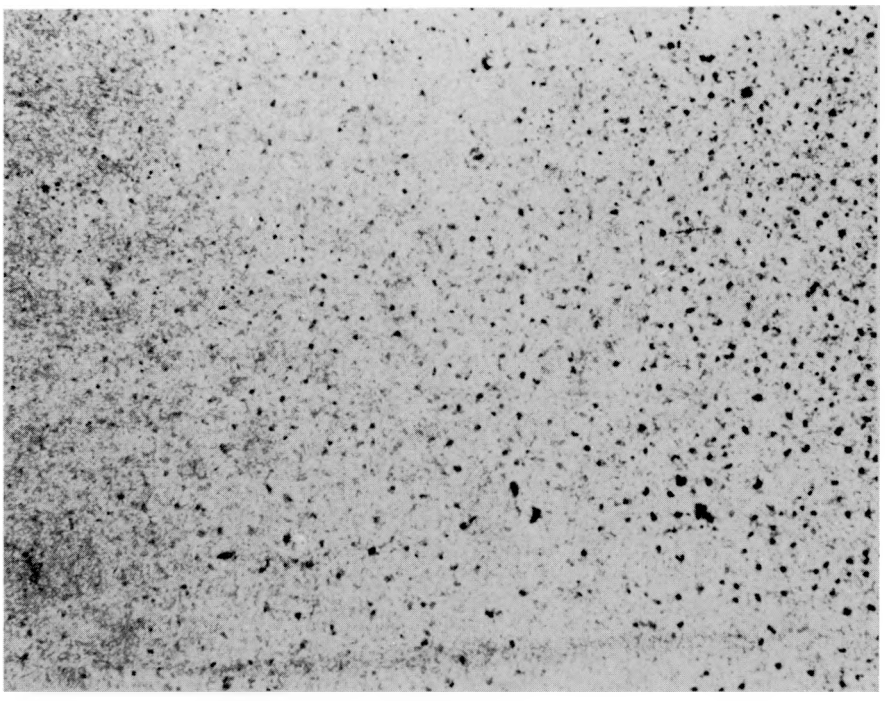

Figure VIII-8. Sample W12-2 View B. Boundary between organic-rich dolomite and clean, vuggy dolomite with a massive dolomite domain. (FOV = 12.8 x 16mm)

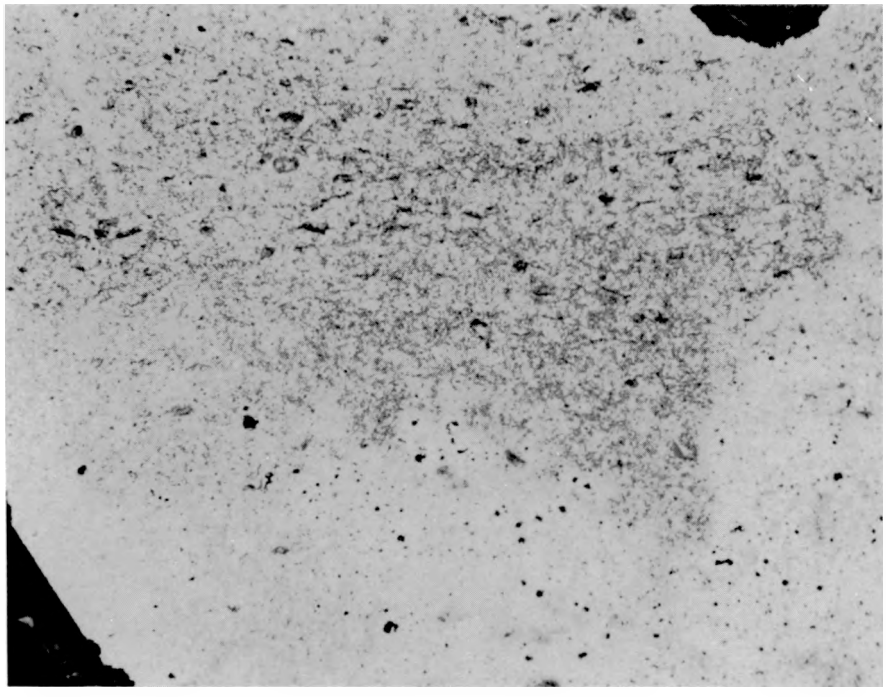

Figure VIII-9. Sample W12-2 View C. Boundary between organic-rich dolomite and clean, vuggy dolomite with a massive dolomite domain. Note lobate form of boundary that cross-cuts primary layering. (FOV = 12.8 x 16mm)

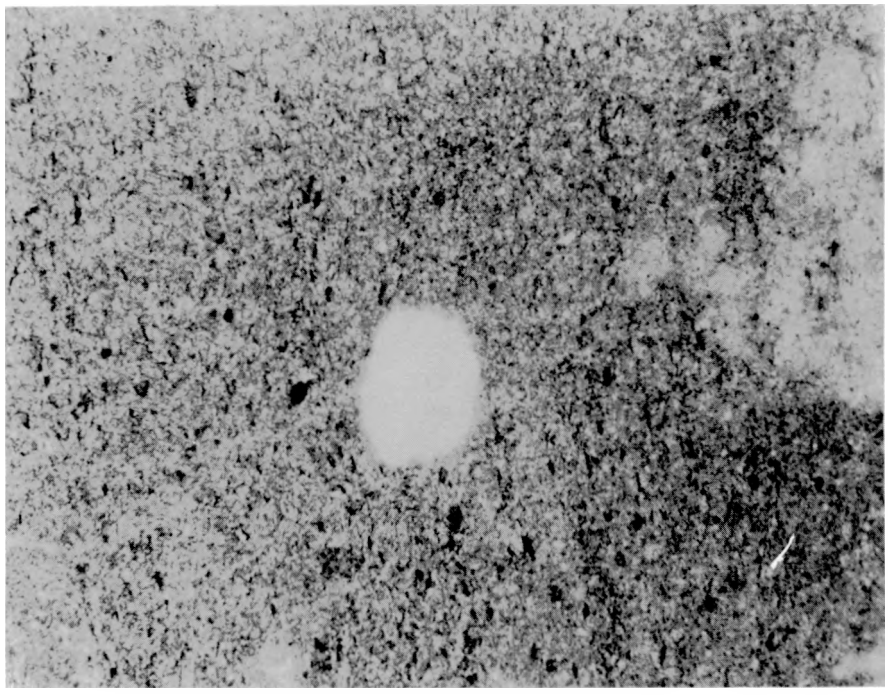

Figure VIII-10. Sample W12-2. Lobate region of a clean dolomite intruding organic-rich dolomite. The lobe of clean dolomite and the vug at center are localized along a narrow fracture. (FOV = 12.8 x 16mm)

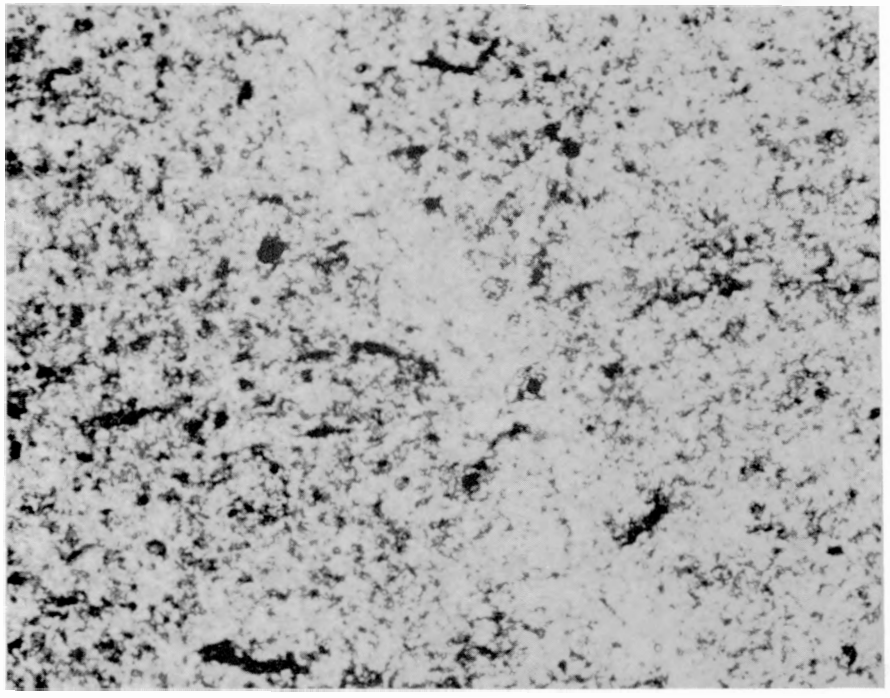

Figure VIII-11. Sample W12-2. Microfracture cutting organic-rich dolomite. Note clean dolomite selvage around microfracture. (FOV = 2.7 x 3.4mm)

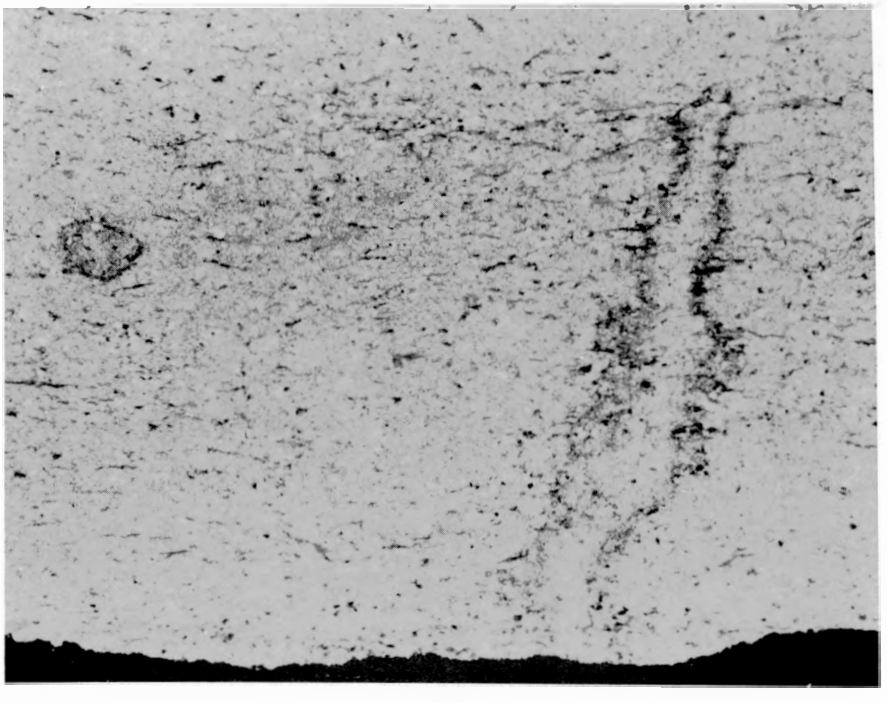

Figure VIII-12. Sample W12-1. Microfracture cutting organic-rich dolomite. Note clean dolomite selvage and dark halo around microfracture. (FOV = 7.2 x 9mm)

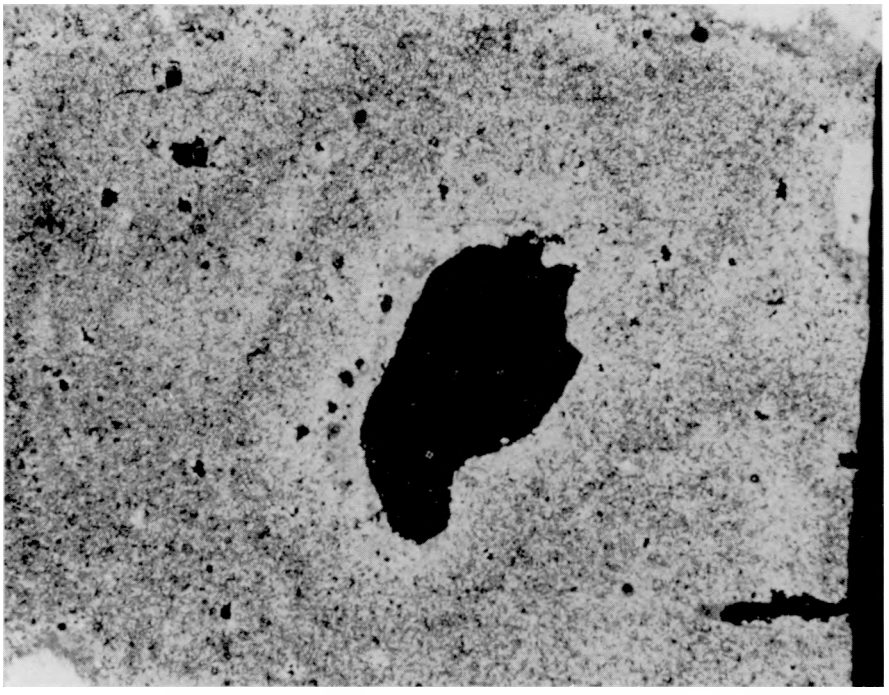

Figure VIII-13. Sample W12-8. Vug in dark organic-rich dolomite. Note clean dolomite selvage and dark halo around vug.

CLAY-RICH LAYERS

As noted above, massive dolomite domains are separated by generally concordant layers that are rich in quartz, clay, detrital mica, and other phases. These impure layers are extremely variable in thickness, lateral continuity, and in relative abundance of non-dolomite phases. Quartz/clay layers are generally most obvious in hand specimen, typically as dark brown horizons within light tan brown dolomite (Figure VIII-14). In thin section they are characterized by anastomosing pods and lenses of fine clay with disseminated quartz and mica in a matrix of fine-grained dolomite (Figure VIII-15, VIII-16, VIII-17). Some clay/quartz-rich layers are relatively thick (up to 1 cm), but are only slightly more impure than massive dolomite. Other layers are extremely thin (<0.2 mm), but contain a relatively dense concentration of non-dolomite phases (Figure 18). All samples examined to date contain some quartz/clay-rich horizons.

Many quartz/clay-rich layers are planar and generally sub-parallel to the inferred orientation of bedding in the sample. In these cases it is difficult to distinguish between an origin involving primary accumulation of detrital quartz, clay, and other phases, and an origin involving concentration of non-dolomite phases by dissolution of associated evaporite minerals. In several examples, however, clay/quartz-rich layers are distinctly non-planar (Figure VIII-19). These layers are suspected to form by the irregular dissolution of pre-existing evaporite phases and concentration of residual phases, although an interpretation involving deposition in a primary irregularity in the underlying bedding surface is also possible.

It should be noted that although the quartz/clay-rich layers account for only a small percentage of the total dolomite volume, they may be extremely important in evaluating chemical interactions with percolating fluids. As is shown below, clay-rich layers appear to preferentially localize in fractures and vugs in the Culebra Dolomite; therefore, these layers may be more likely to interact with fluids than the associated massive dolomite domains.

Characteristics of Vugs and Fractures

VUGS

Vugs are present within most, if not all, samples of the Culebra Dolomite. In general, they can be divided into two broad classes and a number of subclasses. As noted above, small vugs (<0.5 mm) are associated with the clean massive dolomite domains and probably formed during a secondary recrystallization of the primary organic-rich dolomite. These micro-vugs are extremely clean, containing no associated phases or halos (see Figure VIII-6).

Figure VIII-14. Sample W12-17. Dolomite hand specimen with clay-rich layers.

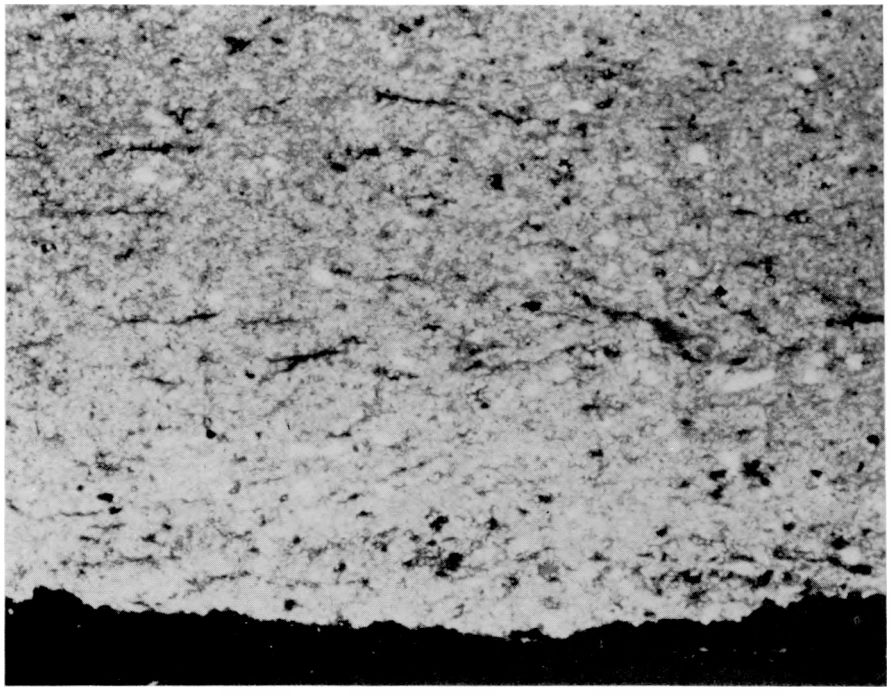

Figure VIII-15. Sample W12-1. Relatively thick clay-rich layer hear one end of sample. (FOV = 2.7 x 3.4mm)

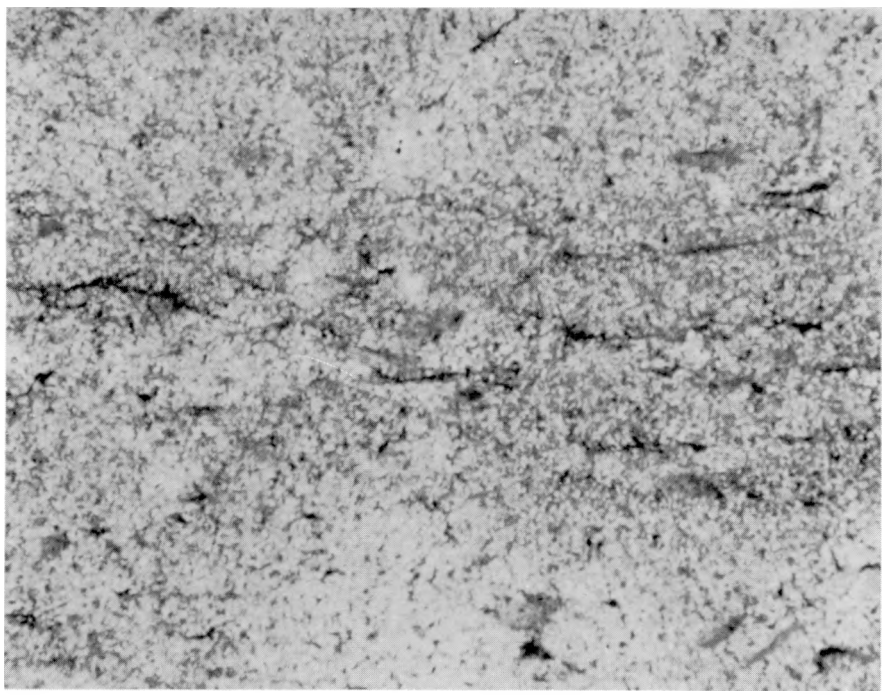

Figure VIII-16. Sample W12-5. Subtle slightly clay-rich layer. (FOV = 3.2 x 4mm)

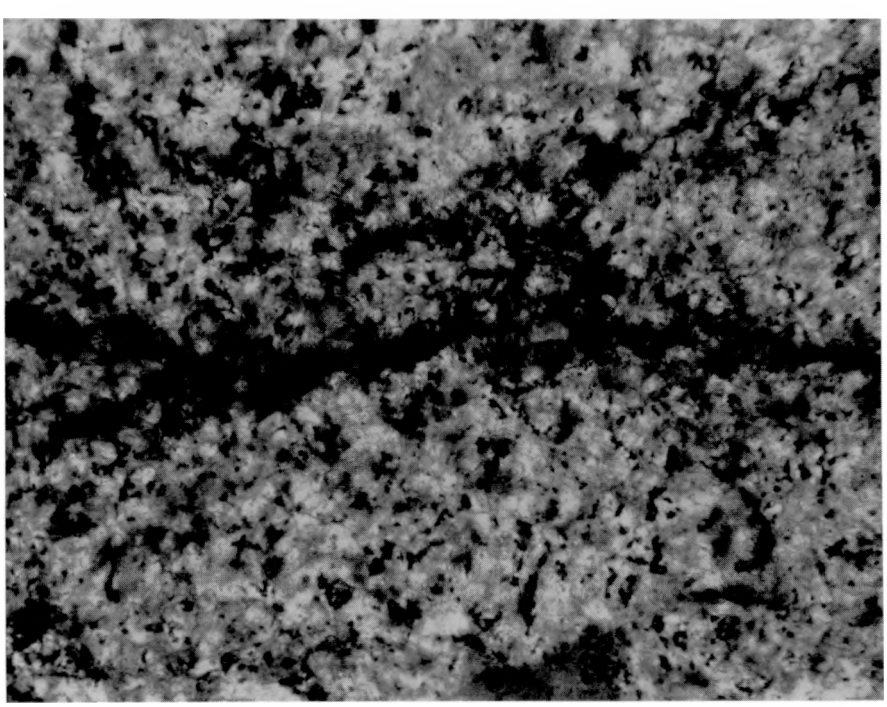

Figure VIII-17. Sample W12-5. Single clay-rich pod from layer shown in Figure VIII-16.

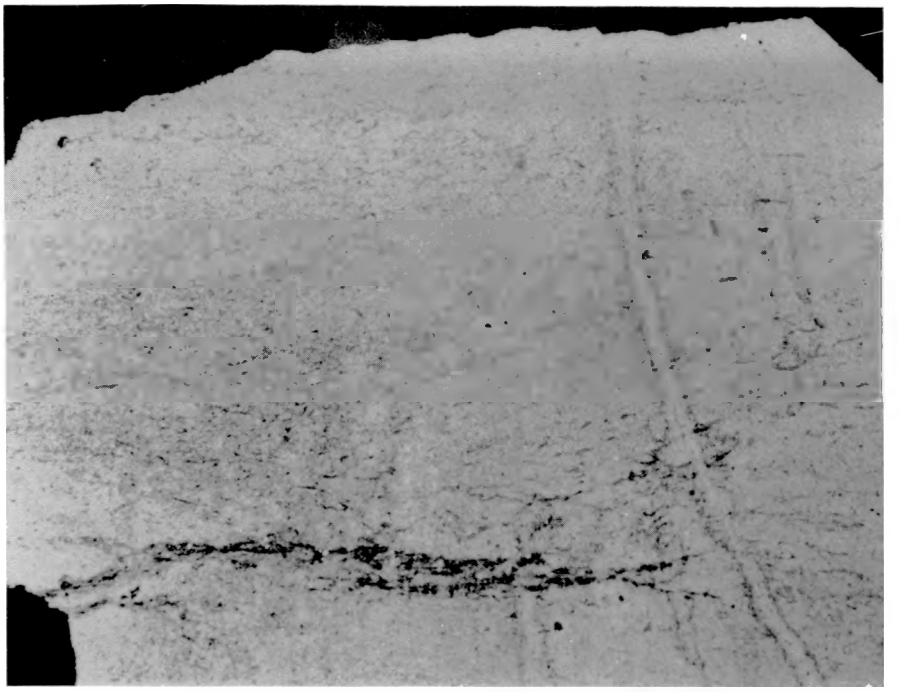

Figure VIII-18. Sample W12-1. Dense clay-rich layer. Note (1) layer pinches out along strike, (2) subtle quartz/clay-rich layers parallel to the main one, (3) cross-cutting fractures with dark halos. (FOV = 12.8 x 16mm)

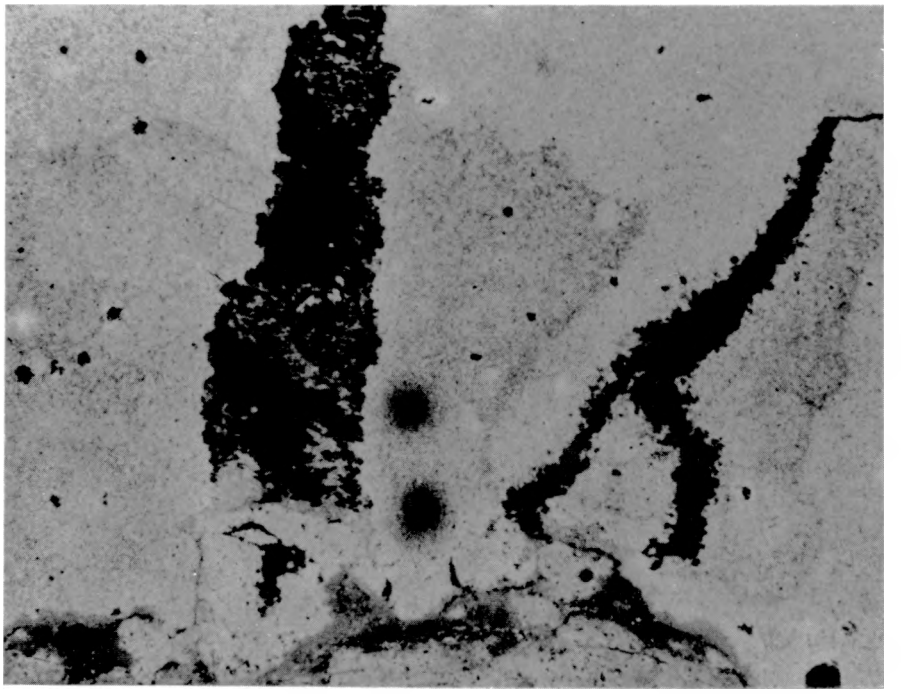

Figure VIII-19. Sample W12-9. Irregular quartz/clay-rich layer. The irregular form of the layer is suspected to result from dissolution of pre-existing evaporite minerals (FOV = 12.8 x 16mm)

The second broad class of vugs is larger (1 mm to 1 cm) and are extremely heterogeneous in appearance. These vugs are generally associated with fractures and quartz/clay-rich layers in the Culebra samples. They occur most commonly near the intersections of fractures and quartz/clay-rich horizons (Figure VIII-20, VIII-21 and VIII-22), but they are relatively common near fractures (Figure VIII-23) or quartz/clay layers alone (Figure VIII-24). The association of vugs and clay-rich layers suggests a feed-back situation in which the clay-rich layers may be characterized by increased permeability contributing to the development of vugs, which in turn may contribute to increased permeability and further vug formation. As noted above, this may indicate that the quartz/clay-rich layers are preferential localities for fluid flow and fluid interaction in the Culebra Dolomite.

Textures and mineralogical characteristics of the large vugs associated with fractures and/or quartz/clay-rich layers are extremely variable. In a single sample, W-12 #8, four distinct textural varieties have been distinguished.

Gypsum-Filled Vugs

These vugs typically contain irregular, feathery fragments of dolomite floating in gypsum. Most contain coatings, partial fillings, or adjacent domains with brown clay-rich dolomite. Most are surrounded by regions with clean massive dolomite, and many display weak black (organic-rich?) halos (Figure VIII-25).

Empty Vugs

Empty vugs typically contain no brown clay coatings or linings. They are surrounded by distinct regions of clean, coarse, vuggy dolomite, which are in turn surrounded by halos of dark (organic?) material (Figure VIII-26).

Vugs Filled with Impure Dolomite

These are typically filled with brown (clay-rich?) impure dolomite with abundant black (organic?) material (Figure VIII-27). They are commonly outlined by a ring of small holes that give them an almost fossil-looking appearance. Several have subtle black halos.

Vugs Filled with Clean Dolomite

These are somewhat similar to Type 3 vugs, but are filled with extremely fine, clean dolomite, with a small amount of fine clay (Figure VIII-28). Many are surrounded by clean dolomite regions and by very subtle dark halos.

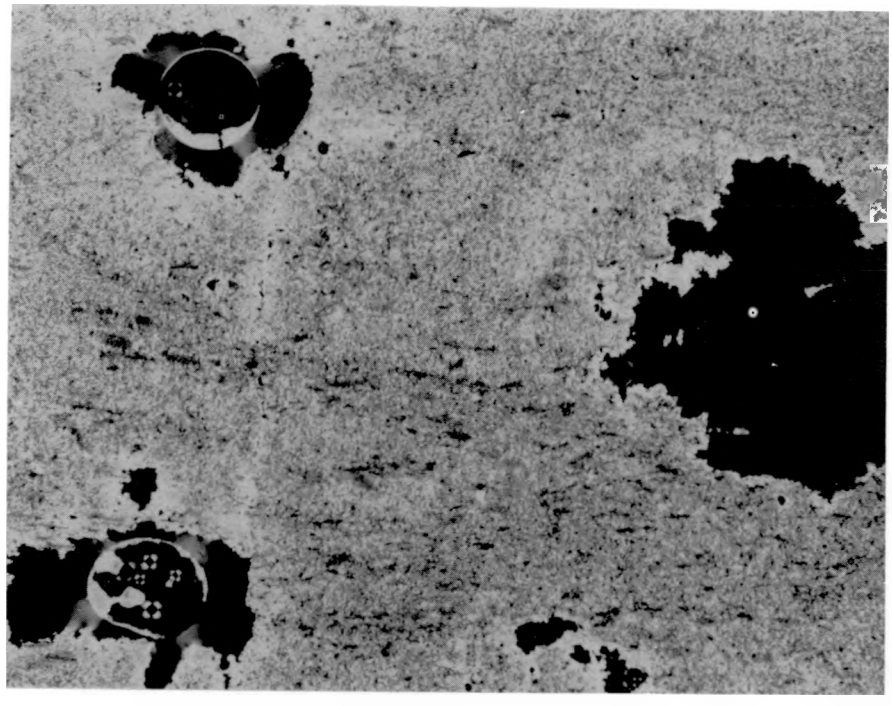

Figure VIII-20. Sample W12-5 View A. Vug located at intersection of fracture and quartz/clay-rich layer. (FOV = 8 x 10mm)

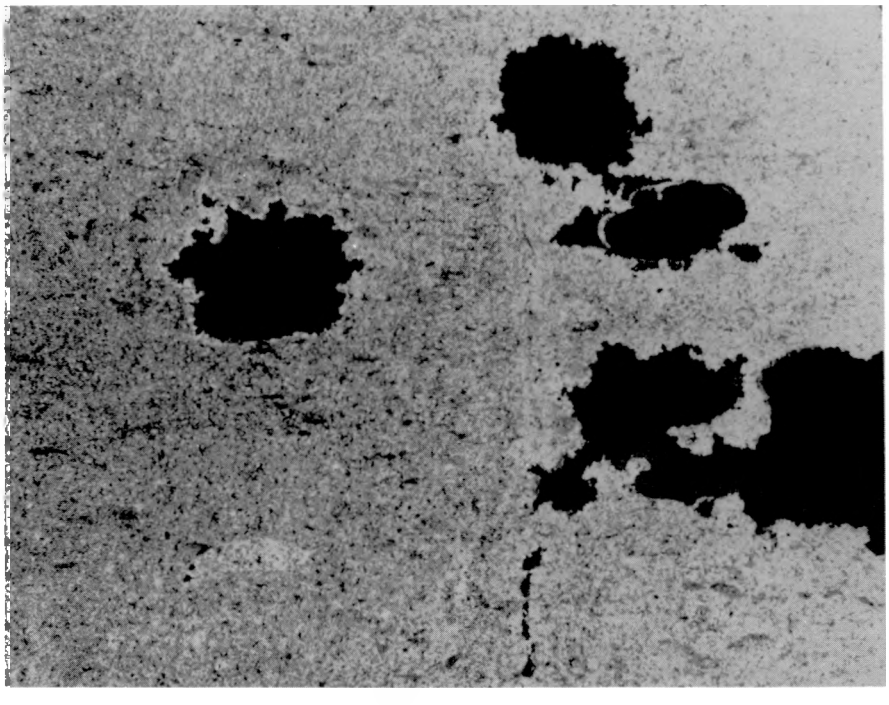

Figure VIII-21. Sample W12-5 View B. Vug located at intersection of fracture and quartz/clay-rich layer. (FOV = 8 x 10mm)

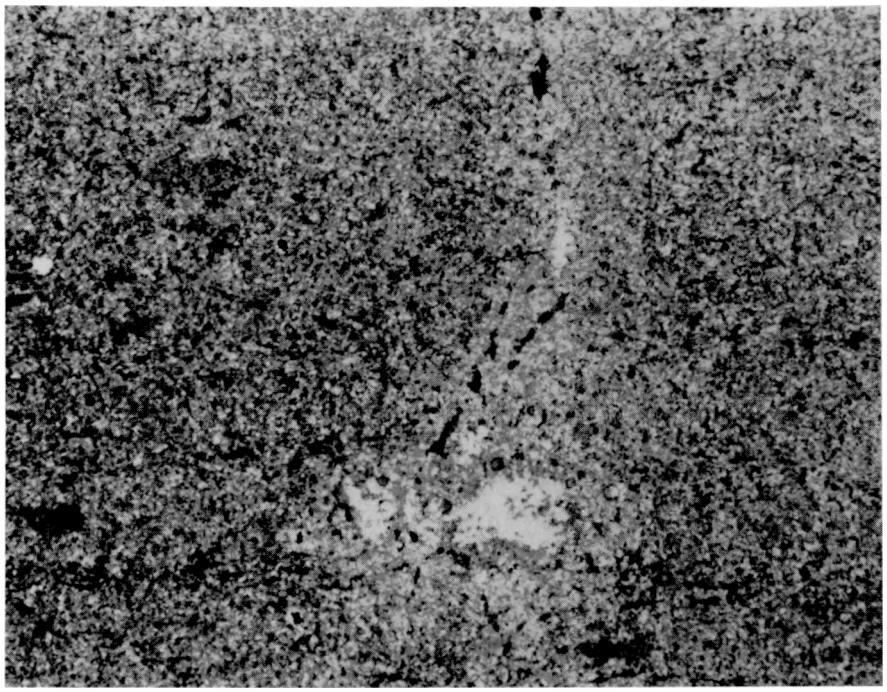

Figure VIII-22. Sample W12-5 View C. Vug located at intersection of fracture and quartz/clay-rich layer. (FOV = 12.8 x 16mm)

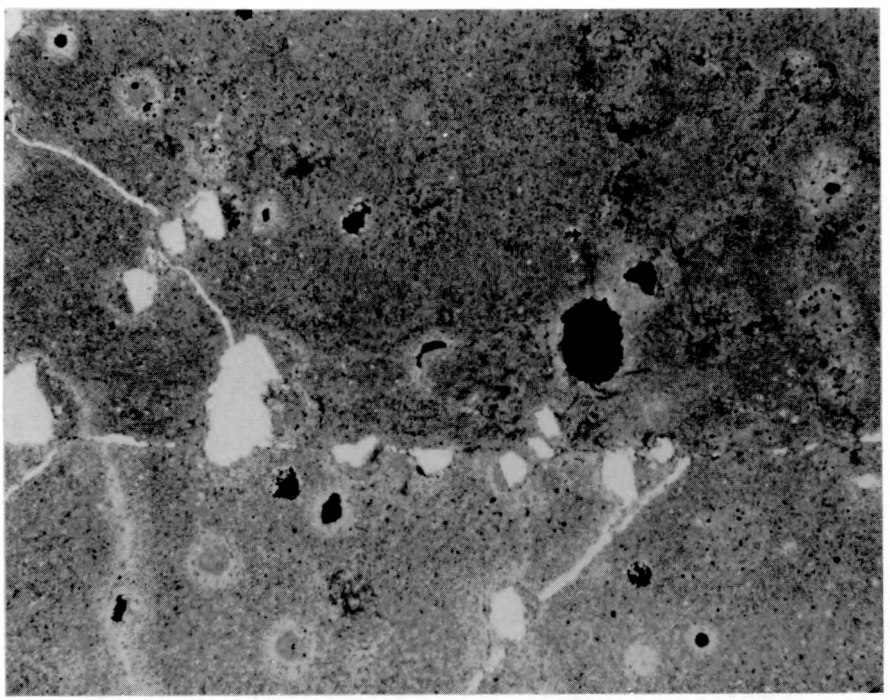

Figure VIII-23. Sample W12-8. Vugs localized along fine fractures in massive dolomite. (FOV = 12.8 x 16mm)

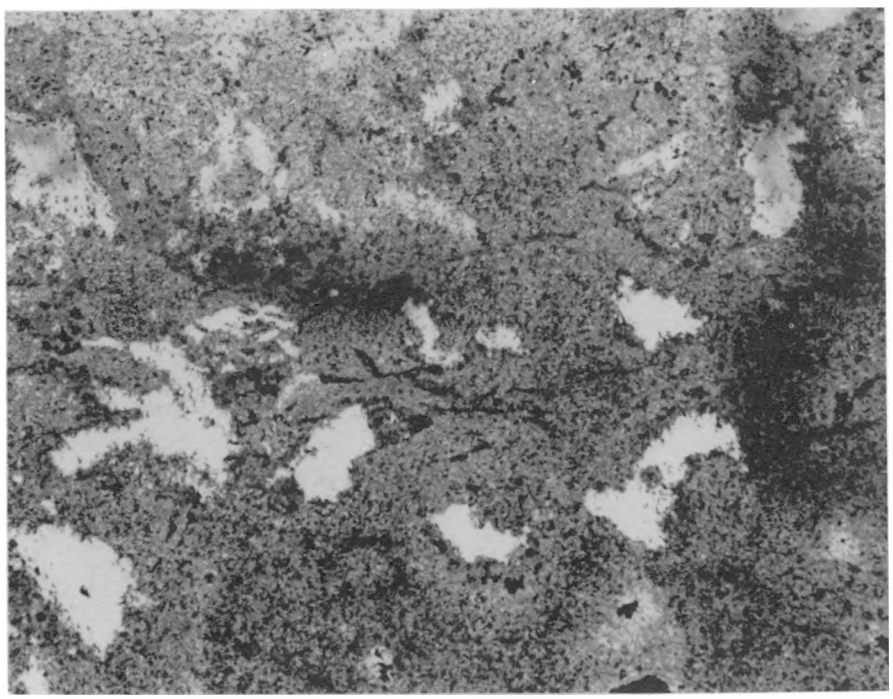

Figure VIII-24. Sample W12-8. Vugs localized along a quartz/clay-rich layer without an obvious intersecting fracture. (FOV = 4.8 x 6mm)

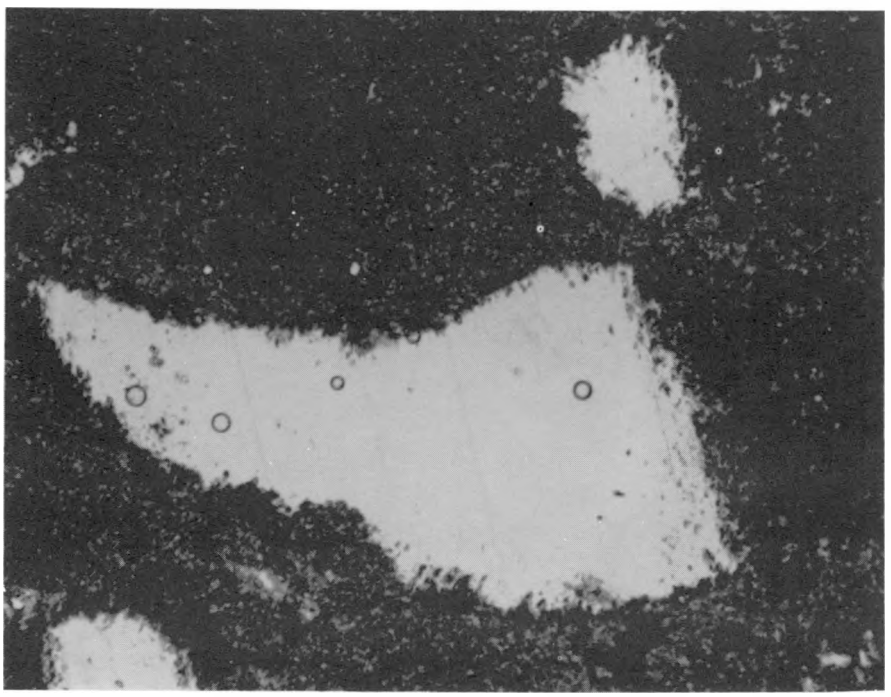

Figure VIII-25. Sample W12-8. Gypsum filled vugs.

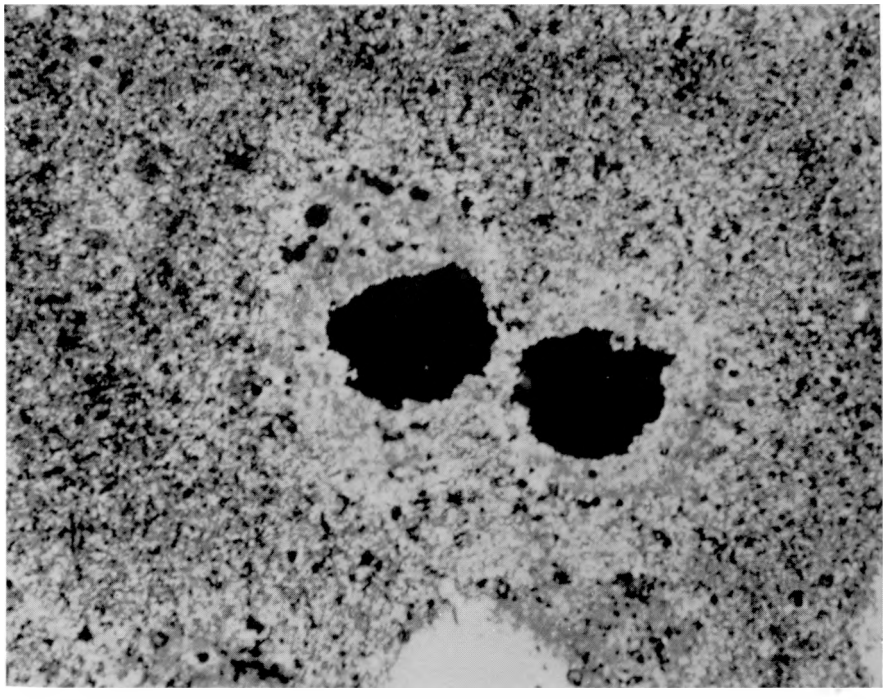

Figure VIII-26. Sample W12-8. Empty vugs. Note smooth clean edges and distinct halos.

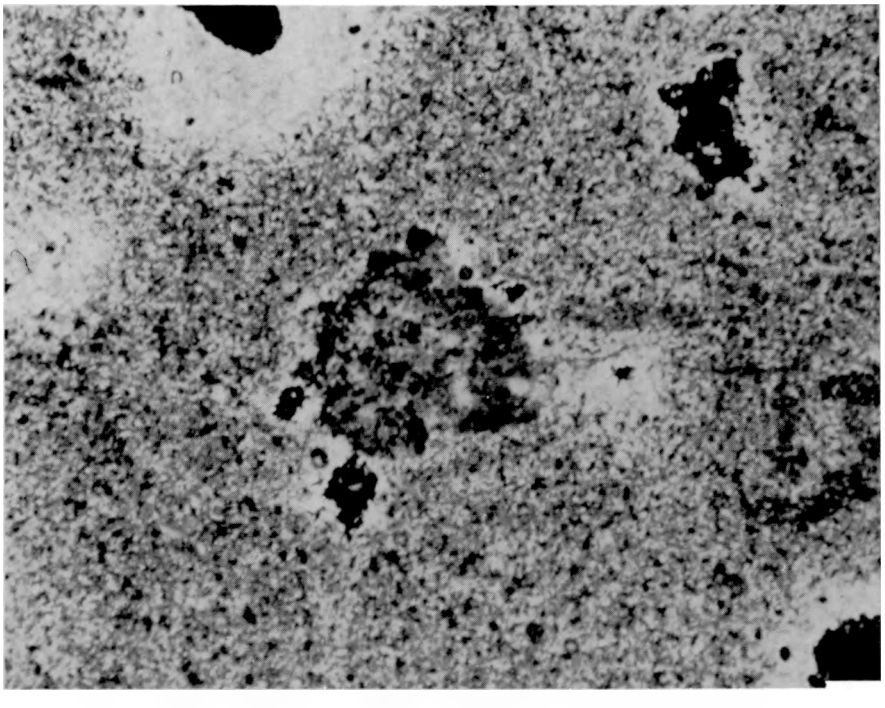

Figure VIII-27. Sample W12-8. Vugs filled with clay-rich impure dolomite. Note ring of holes at edges and lack of distinct halos.

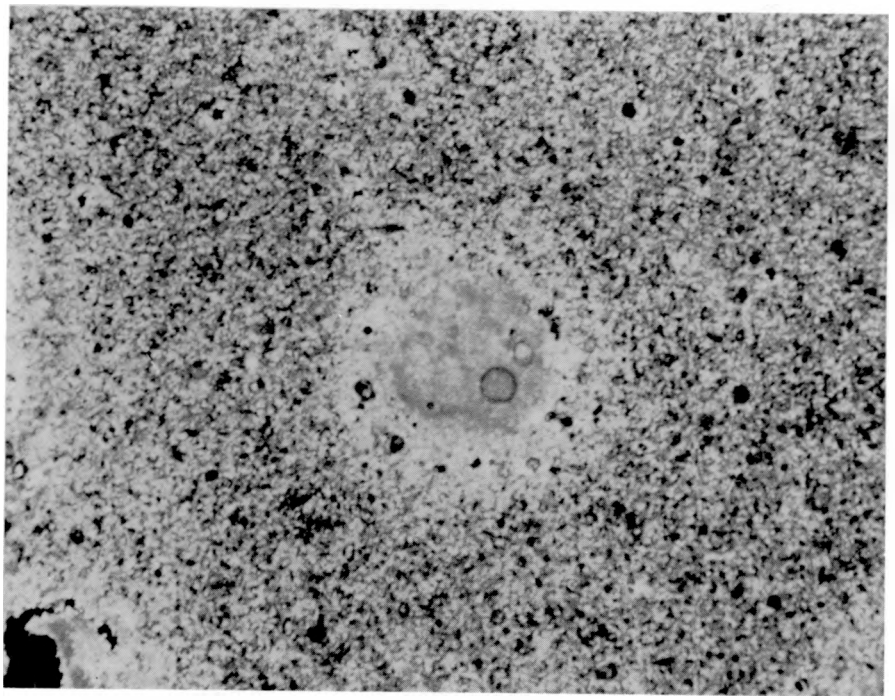

Figure VIII-28. Sample W12-8. Vugs filled with fine grained, clear dolomite.

Discussion

Each of these vug types probably represents a stage in an ongoing and evolving vug-forming process. The dolomite-filled vugs may be in the early stages of formation, or they may be relatively late-stage vugs that have been filled by secondary clay and dolomite. Because of the poorly developed halos and selvages, the former hypothesis is preferred. Gypsum-filled vugs are typically interconnected by gypsum-filled fractures, suggesting that non-gypsum bearing fractures may have lacked access to fluids during gypsum deposition (Figure VIII-29). It is interesting to note that the edges of gypsum-bearing vugs are irregular and feathery, whereas the edges of empty vugs are typically smooth and sharp. This may suggest that gypsum-bearing vugs may have formed approximately synchronously with gypsum deposition, and perhaps the gypsum-bearing solutions were partly responsible for vug development. If so, it is likely that the empty vugs represent a distinct vug-forming period, possibly with different vug-forming fluids. No consistent vug-forming paragenesis has yet been worked out for the Culebra samples, but it is suspected that such a paragenesis exists and may be resolvable with further microscopic investigations.

FRACTURES

Virtually all Culebra Dolomite samples display fractures to some extent (Figure VIII-30). Similar to the vugs and holes, a wide variety of fracture types and fracture fillings occurs, often within a single sample. Fractures range from narrow, almost imperceptible structures, defined by subtle halos or selvages, to broad, gypsum-filled structures. As noted above, fractures have probably provided an important access to a variety of fluids throughout the evolution of the dolomite.

A wide variety of fracture types has been observed in the Culebra Dolomite. The following is a summary of several of the most common varieties.

Gypsum-Filled Fractures

These are relatively through-going fractures that are completely or partly filled by gypsum. They typically have little or no edge effects or selvages. If anything, they may have minor concentrations of clay minerals along the fracture walls. Gypsum-filled fractures typically occur at relatively high angles to layering and are usually associated with gypsum-filled vugs and holes (Figure VIII-31, VIII-32).

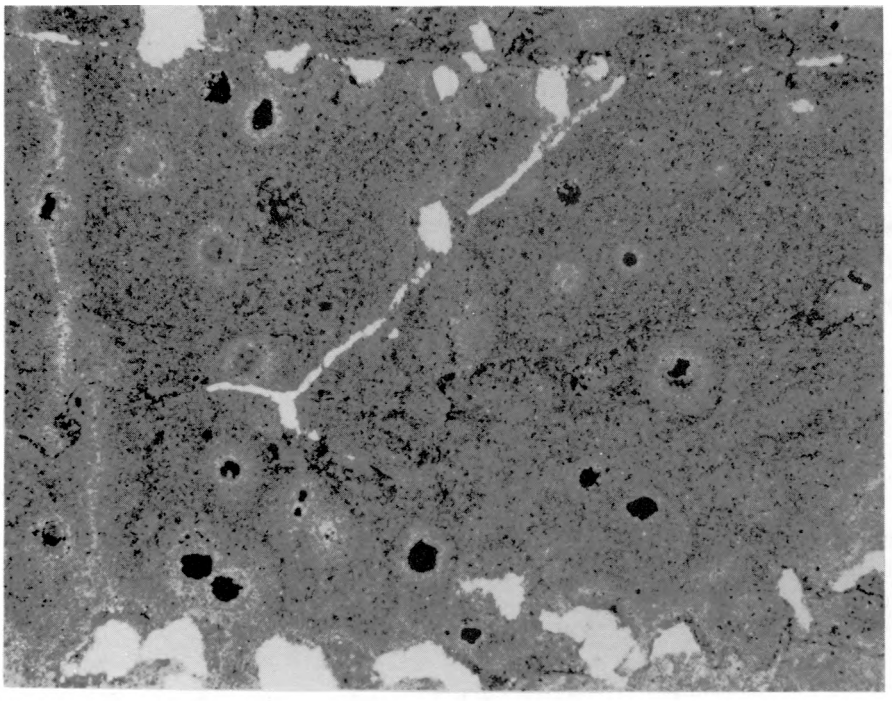

Figure VIII-29. Sample W12-8. Gypsum filled vugs with interconnecting gypsum-filled fractures and empty vugs with no connecting gypsum-filled fractures.

Figure VIII-30. Sample W12-15. Hand specimen showing various types of fractures.

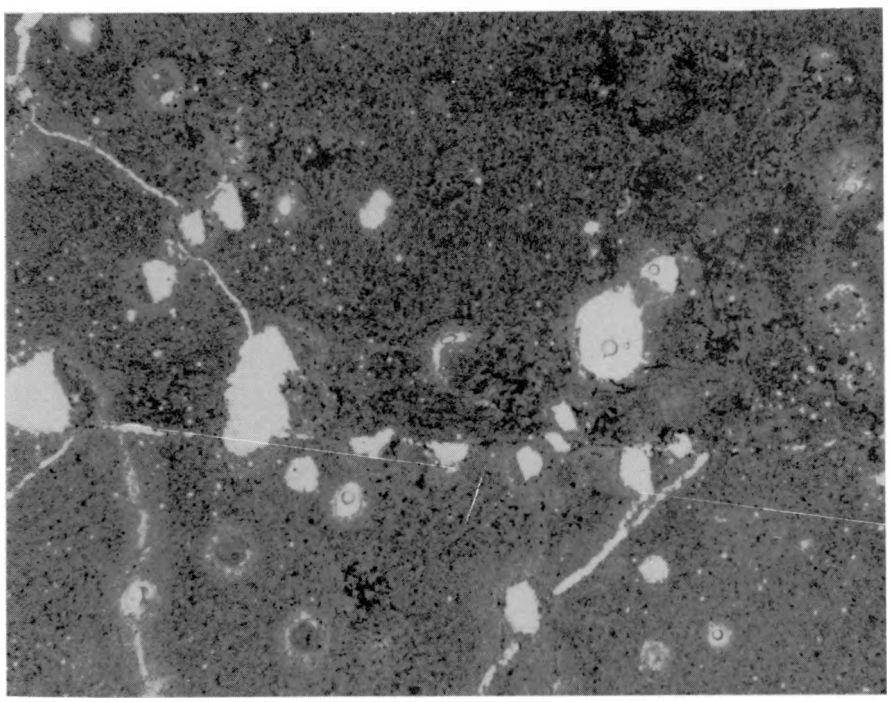

Figure VIII-31. Sample W12-8. Fine gypsum-filled fractures in massive dolomite. Note associated gypsum-filled vugs. Note also convoluted brown fracure. (FOV = 12.8 x 16mm)

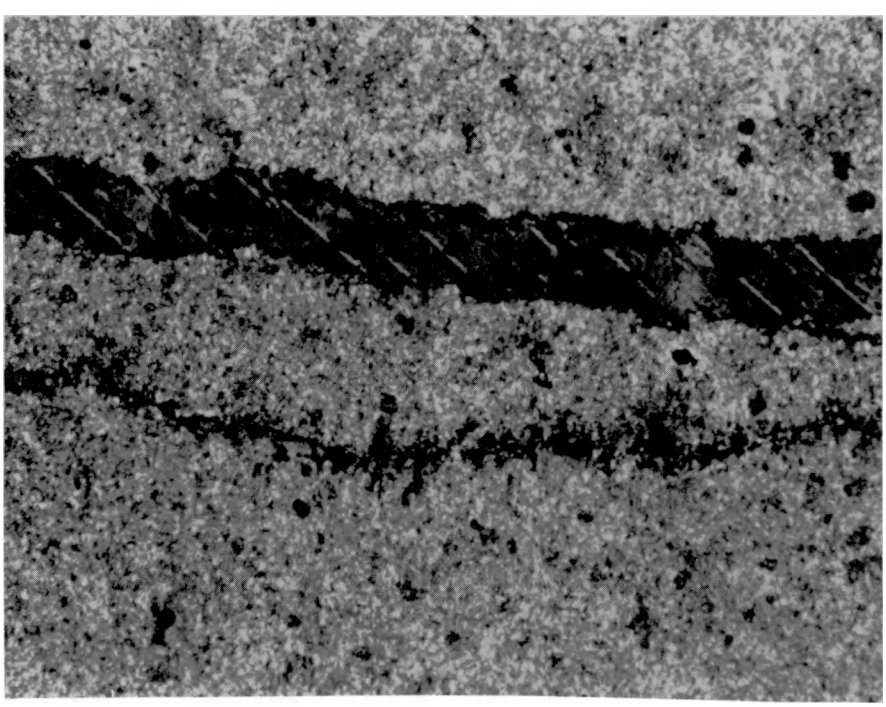

Figure VIII-32. Sample W12-7. Gypsum-filled fractures in massive dolomite. Note irregular boundary on smaller fracture (FOV = 2.7 x 3.4mm)

Clay-Lined Fractures

These fractures are defined by narrow concentrations of brown/black clay-rich material with little or no open space along the fracture. They display extremely irregular, convoluted shapes somewhat similar to carbonate stylolites. Several of these features cut, terminate against, or grade into gypsum-filled fractures; some appear to have been subsequently filled by gypsum. They are generally not associated with selvages, halos, or other edge effects (Figure VIII-33).

"Healed" Fractures

"Healed" fractures appear as a string of tiny holes within clean dolomite giving the appearance that an original fracture has been healed by secondary precipitation of dolomite. They are typically associated along their length with empty vugs. Of all fracture types, these are characterized by the most pronounced edge effects. They are surrounded by a zone of coarser, clean dolomite (that may represent secondary, reprecipitated dolomite), which is, in turn, surrounded by halos of dark (organic-rich?) material (Figure VIII-34).

Fractures Along Clay-Rich Layers

Most of the relatively thick clay-rich layers in the Culebra Dolomite are associated to some degree with fractures. These fractures are irregular, almost anastomosing, in shape, and they are somewhat intermittent along the clay-rich layer. In many cases, the fractures are associated with the darkest, clay-richest parts of the quartz/clay layers. Although some of these fractures may have formed during drilling and thin section preparation, others show evidence of having localized gypsum, clay, or clean dolomite and are, therefore, a significant feature in the dolomite. These fractures are important because they suggest that fluids may be preferentially channelled through clay-rich regions in the dolomite and, thus, may have an increased opportunity to interact with the clay minerals (Figure VIII-35).

Open (Water Bearing) Fractures

Obviously, the most important types of fractures in the Culebra Dolomite are open fractures that show evidence of fluid transport (Figure VIII-36, VIII-37). These fractures are not visible in thin section, since the core sections are invariably broken along their surfaces. The surfaces themselves are lined with powdery dolomite and calcite, clay, quartz, and gypsum, in varying proportions. The separation between adjacent surfaces is not deducible from the samples in this study, since the adjoining core sections are separated when extracted from the drill casing.

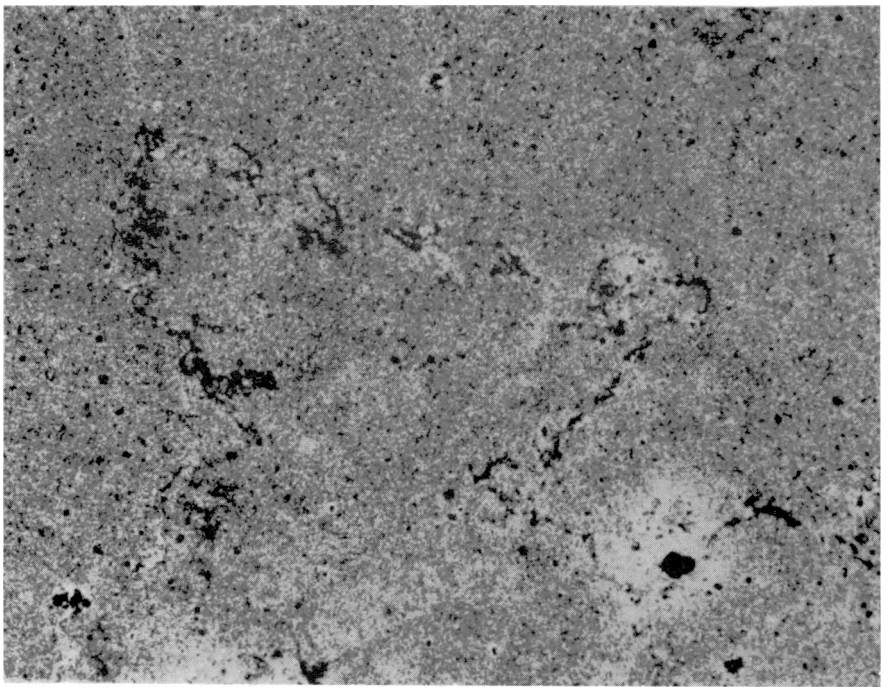

Figure VIII-33. Irregular Brown Clay-rich Fractures. Fractures are almost serrate in form and commonly curve back on themselves along strike of the fracture. (FOV = 5.6 x 7mm)

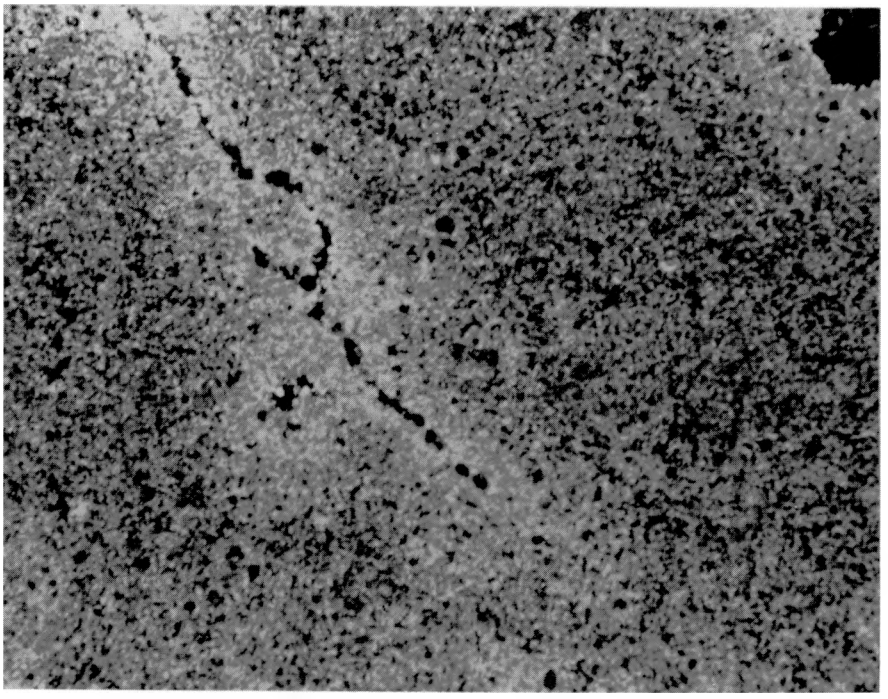

Figure VIII-34. Sample W12-8. "Healed" fractures in massive dolomite. These may represent fractures that have been sealed with secondary dolomite.

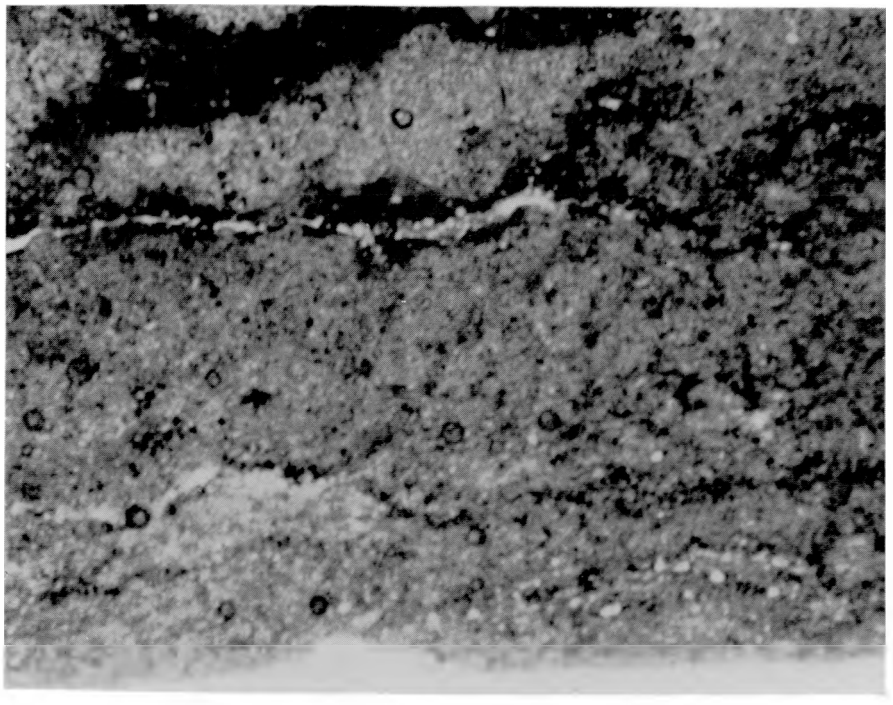

Figure VIII-35. Fractures Associated with Quartz/Clay-rich Layers. Note that the fractures have dark clay concentrations along their walls.

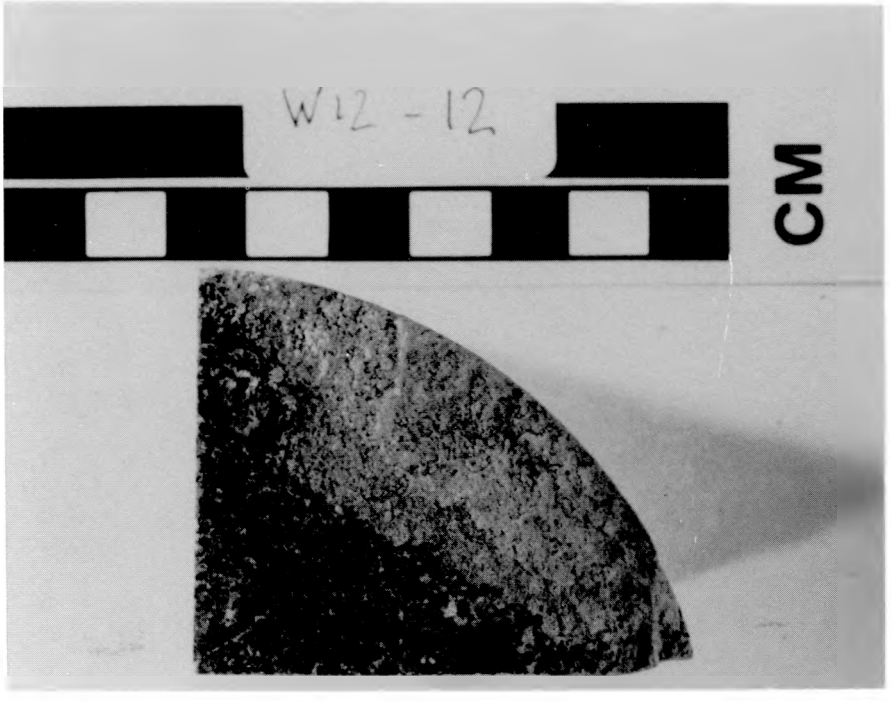

Figure VIII-36. Sample W12-12. Surface of open fracture in hand specimen.

Figure VIII-37. Sample W12-10. Surface of open fracture in hand specimen.

Discussion

Many Culebra Dolomite samples contain several fracture types within a relatively small area (Figure VIII-38). Within a single thin section, gypsum-filled fractures, clay-rich fractures, and open fractures are typically present with cross-cutting relationships. As with the vugs and holes, no paragenetic sequence has yet been worked out for the evolution of the Culebra fractures, but it is possible that such a sequence can be resolved with additional petrographic investigations.

Additional Textural Features

Several samples of Culebra Dolomite contain abundant gypsum that is not apparently related to fractures or vug-fillings. In these samples, gypsum is a major component of the matrix, typically occurring as large, irregular-shaped, gypsum-bearing patches within massive dolomite. Boundaries between gypsum-bearing and gypsum-absent domains are irregular, typically occurring at a relatively high angle to layering (Figure VIII-39).

Several pieces of evidence suggest that the gypsum-rich regions may be secondary, having replaced or intruded the original dolomite. Gypsum-rich domains often contain irregularly-shaped dolomite patches with feathery edges and shapes that suggest dissolution or reprecipitation of the dolomite patches (Figure VIII-40). Further, the boundaries of gypsum-rich regions typically display anomalous clay concentrations and dark (organic-rich?) halos similar to those associated with fractures and vugs (Figure VIII-41).

Gypsum-rich domains occur in only three of the sixteen samples taken from the WIPP-12 core. The regional abundance of these domains is not known at present, nor is the significance of these domains with respect to primary depositional or secondary processes within the Culebra Dolomite.

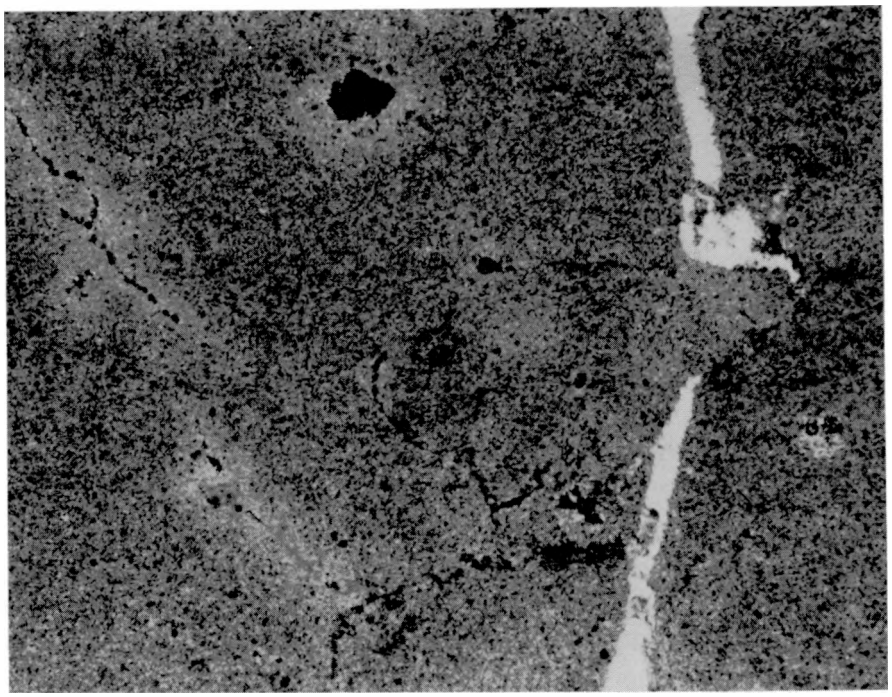

Figure VIII-38. Sample W12-8. Massive dolomite displaying various types of fractures. (FOV = 5.6 x 7mm)

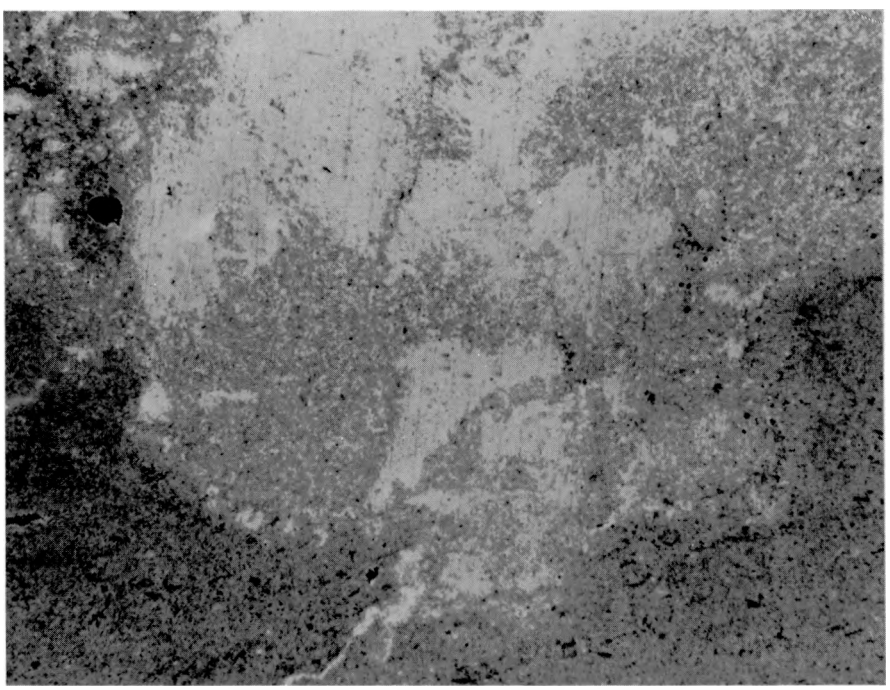

Figure VIII-39. Sample W12-6. Gypsum-rich domain within massive dolomite. Note irregular, cross-cutting nature of the domain boundary. (FOV = 12.8 x 16mm)

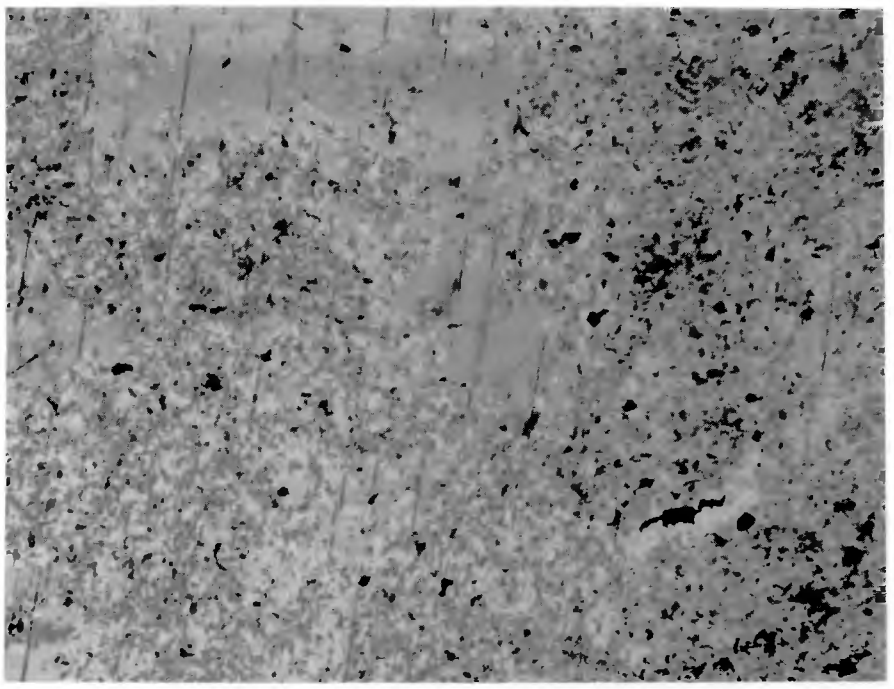

Figure VIII-40. Sample W12-6. Gypsum-rich domain showing patches of dolomite "floating" in a gypsum matrix. Note irregular, feathery edges on dolomite patches. (FOV = 2.7 x 3.4mm)

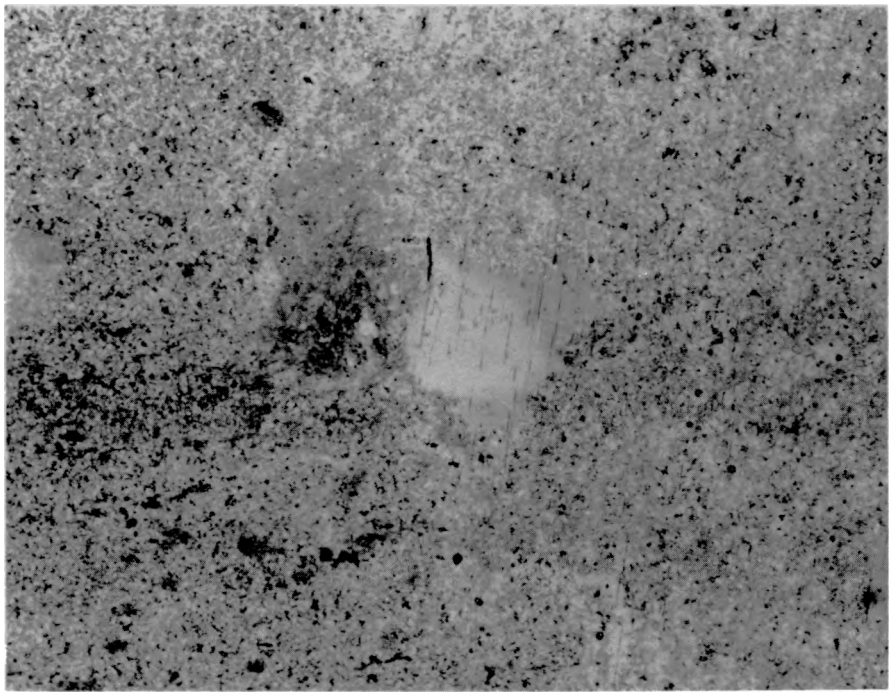

Figure VIII-41. Sample W12-6. Boundary between gypsum-rich domain and massive dolomite. Note clay concentrations near the domain boundary and generally clay-rich nature of dolomite outside of gypsum-rich region compared to dolomite within the gypsum-bearing domain.

IX. SUMMARY AND CONCLUSIONS

The Culebra Dolomite member of the Rustler Formation is mineralogically and texturally heterogeneous, both vertically and horizontally. Although the predominant mineral is dolomite, important constituents of the formation are clay, quartz, gypsum, and calcite. Trace minerals include halite, phyllosilicates of metamorphic origin, feldspar, and pyrite.

Dolomite in the samples examined in this study forms an equigranular microcrystalline mosaic in which individual grains are subhedral rhombs, typically 5 microns in equivalent diameter, but varying from 2 to 20 microns. Dolomite compositions have an average calcium to magnesium ratio of 1.05 and an average of 0.004 atoms of iron per unit cell. The origin of the dolomite is presumed to be the result of early stage dolomitization of chemically sedimented calcite, which was deposited in shallow waters; algal mats probably formed what is now interstitial organic matter that is mixed with clay. The dolomite content of the samples examined in this study ranges from a few percent to nearly 99% of the total; the majority of the samples had 80% or more dolomite.

The next most important constituent of the Culebra Dolomite is clay. Not only is clay the second most abundant mineral present, but the fact that it is concentrated along textural features, particularly the surfaces of open (fluid bearing) fractures and vugs, makes its presence of particular importance to the characterization of hydrological transport within the formation. Clay abundances range from less than 1.0% to nearly 60% of the bulk samples. Within the more typical "massive" dolomite samples, there are bedding parallel domains, which alternate between clay-rich and clay-poor compositions; these domains give the "massive" dolomite samples a laminated appearance. Organic matter is intimately associated with the clay in all the samples and gives the mixture a brown to dark black color.

The clay mineral assemblage includes four minerals: corrensite (ordered mixed-layer chlorite/smectite), illite, serpentine, and chlorite. Corrensite is the dominant clay mineral, usually constituting about 50% of the clay assemblage; illite is the next most abundant constituent, and serpentine and chlorite are relatively minor components. Because of its high CEC, the presence of corrensite is of particular importance. Corrensite will be an effective sorbent of radionuclide cations in the event of a breach in the WIPP facility. The remaining clay minerals have much lower CEC's.

Gypsum is present largely as a vein and vug-filling cement; it is probably almost entirely of secondary origin: the product of the gypsification of the anhydrite in the Tamarisk member, which overlies the Culebra Dolomite. All

fluid-bearing surfaces examined by XRD show the presence of gypsum, and it seems likely that fluids moving through the formation are saturated with respect to gypsum. Except for one sample in the WIPP-12 core, gypsum rarely exceeds 10% of the total; usually, much less than that. EMX elemental analysis of gypsum in the Culebra samples shows that it is almost pure $CaSO_4.2H_2O$; all other elements that might have been present were below detection levels.

Calcite is only present in measurable quantities in the WIPP-29 core, where it is a major component of the top part of the core. However, XRD analysis of powders obtained from scraping fluid-bearing (open) fractures shows the presence of varying amounts of calcite on the surfaces of these fractures. Calcite is interpreted to be of secondary origin, produced by dedolomitization of dolomite by calcium-rich waters of meteoric origin. Calcite in samples from the WIPP-19 core is microcrystalline; the crystals form a mosaic pattern that is very similar in appearance to the micritic dolomite of the same samples. EMX analyses of a sample from the WIPP-19 core show that calcite is nearly pure $CaCO_3$ with less that 1% total MgO+FeO.

Two texturally important features of samples from the Culebra Dolomite are vugs and fractures. Vugs appear to have been formed by dissolution of evaporitic material (presumably halite); they are sometimes filled with secondary gypsum, dolomite, and clay, although those connected with open fractures usually remain empty. The most important types of fractures in these samples are those that bear evidence of fluid movement upon their surfaces. The surfaces of these fractures are coated with clay, powdery dolomite, calcite, and gypsum. The minerals on these surfaces will interact directly with radionuclide bearing brines in the event of a low-pressure breach in the WIPP facility.

X. REFERENCES

Ahn, J.H., and D.R. Peacor. 1986. "Transmission and Analytical Electron Microscopy of the Smectite-to-illite Transition." *Clays and Clay Minerals* 34, 165-179.

Bethke, C.M., and S.P. Altaner. 1986. "Layer-by-layer Mechanism of Smectite Illitization and Application of a New Rate Law." *Clays and Clay Minerals* 34, 136-145.

Blatt, H. 1982. *Sedimentary Petrology*. W.H. Freeman and Co., San Francisco, 564p.

Bodine, M.W. Jr. 1978. "Clay Mineral Assemblages from Drill Cores of Ochoan Evaporites, Eddy County, New Mexico." *Geology and Mineral Deposits of Ochoan Rocks in Delaware Basin and Adjacent Areas: New Mexico Bureau of Mines and Mineral Resources*, Cir. 159, 21-31.

Bodine, M.W. Jr. 1983. *Trioctahedral Clay Mineral Assemblages in Paleozoic Marine Evaporite Rocks*. Sixth International Symposium on Salt, Vol. I, 267-284.

Bodine, M.W. Jr. 1985. "Clay Mineralogy of Insoluble Residues of Marine Evaporites." *Soc. of Mining Engineers of AIME, Process Mineralogy V: Application to the Mineral Industries*, 133-156.

Bodine, M.W. Jr., and T.H. Fernalld. 1973. "EDTA Dissolution of Gypsum, Anhydrite and Ca-Mg Carbonates." *Jour. Sed. Petrology* 43, 1152-1156.

Bodine, M.W., and R.R. Standaert. 1977. "Chlorite and Illite Compositions from Upper Silurian Rock Salts, Retsof, New York." *Clays and Clay Minerals* 25, 57-71.

Bodine, M.W., and B. Madsen. 1985. "Mixed-layer Chlorite/Smectite from an Evaporite Cycle in the Paradox Member of the Hermosa Formation, Grand County, Utah." *Proceedings of the 8th International Clay Conference*, 1-39.

Borns, D.J., L.J. Barrows, D.W. Powers, and R.P. Snyder. 1982. *Deformation of Evaporites Near the Waste Isolation Pilot Plant (WIPP) Site*. SAND82-1069. Albuquerque, NM: Sandia National Laboratories.

Braitsch, O. 1971. *Salt Deposits: Their Origin and Composition*. Springer-Verlag, Berlin, 297p.

Brindley, G.W. 1980. "Order-Disorder in Clay Mineral Structures." *Crystal Structures of Clay Minerals and Their X-Ray Identification*. Eds. G.W. Brindley and G. Brown. Mineralogical Society, London, 495p.

Ferrall, C.C., and J.F. Gibbons. 1979. *Core Study of the Rustler Formation Over the WIPP Site*. SAND79-7110. Albuquerque, NM: Sandia National Laboratories.

Goldsmith, J.R., and D.L. Graf. 1958. "Structural and Compositional Variations in Some Natural Dolomites." *J. Geology* 66, 678-693.

Harville, D.G., and S.J. Fritz. 1986. "Modes of Diagenesis Responsible for Observed Successions of Potash Evaporites in the Salado Formation, Delaware Basin, New Mexico." *J. Sed. Petrology* 56, 648-656.

Klimentidis, R.E., and I.D.R. Mackinnon. 1986. "High Resolution Imaging of Ordered Mixed-Layer Clays." *Clays and Clay Minerals* 34, 155-164.

Lee, J.H., and D.R. Peacor. 1986. "Expansion of Smectite by Laurylamine Hydrochloride: Ambiguities in Transmission Electron Microscope Observations." *Clays and Clay Minerals* 34, 69-73.

Mackinnon, I.D.R., and S.A. Kaser. 1987. *Microanalysis of Clays at Low Temperatures*. Microbeam Analysis - 1987. Ed. R.H. Geiss. San Francisco, 332-333.

Nadeau, P.H., J.M. Tait, W.J. McHardy, and M.J. Wilson. 1984. "Interstratified XRD Characteristics of Physical Mixtures of Elementary Clay Particles." *Clay Minerals* 19, 67-76.

Palmer, D.P. 1981. "Clay Mineralogy of Permian Sabkha Sequences, Palo Duro Basin, Texas." Unpublished M.S. thesis, University of Texas, Austin.

Reynolds, R.C. Jr. 1980. "Interstratified Clay Minerals." *Crystal Structures of Clay Minerals and Their X-Ray Identification*. Eds. G.W. Brindley and G. Brown. Mineralogical Society, London, 495p.

Sewards, T., R. Glenn, and K. Keil. 1991. *Mineralogy of the Rustler Formation in the WIPP-19 Core*. SAND87-7036. Albuquerque, NM: Sandia National Laboratories.

Starkey, H.C., P.D. Blackmon, and P.L. Hauff. 1984. "The Systematics of Clay Mineral Identification." *U.S. Geol. Survey Bull.* 1563, 1p.

Tardy, Y., and L. Gartner. 1977. "Relationships Among Gibbs Energies of Formation of Sulfides, Nitrates, Carbonates, Oxides and Aqueous Ions." *Contrib. Mineral. Petrol.* 63, 89-102.

APPENDIX A:
ANALYTICAL PROCEDURES

X-Ray Fluorescence Spectroscopy

Whole rock samples were ground up in a ballmill and/or with a mortar and pestle and then passed through a 100 mesh sieve. Samples were then thoroughly mixed; an 8.5 gr. portion was weighed out and placed in a clean plastic vial. 1.5 gr. of boric acid (H_3BO_4) was added. A clean styrene ball was then placed in the vial, and the mixture was blended in a ball mill shaker for ten minutes. The styrene ball was removed from the mixture, and the powder was placed in an aluminum pellet container and pressed to 20 Kb in a hand press. The pellets were then analyzed in a Rigaku 3064M x-ray fluorescence (XRF) spectrometer for eight component oxides: SiO_2, Al_2O_3, CaO, MgO, FeO, Na_2O, K_2O, and SO_3. For the first seven oxides, standard 88b, a natural dolomite NBS (National Bureau of Standards) was used; for sulfide, standard R2, a sample from the Lower Member of the Rustler Formation, for which sulfate content was determined gravimetrically, was used.

In order to obtain compositional data for the clay mineral separates, fused disks of the three separates were made. Dried separates were ground with a mortar and pestle, passed through a 100 mesh sieve, and thoroughly mixed. A 1.0 gr. portion was then weighed out and placed in a clean plastic vial; 9.1 gr. of flux (9.0 gr. of lithium tetraborate mixed with 0.1 gr. of ammonium nitrate) were added. The mixture was placed in a plastic vial and a styrene ball added; the contents were thoroughly blended in a ball mill shaker for ten minutes. The styrene ball was removed, and the contents were placed in a platinum crucible and heated in a furnace to 1000°C for about five minutes, until the mixture was completely fluid and had a reddish glow. A platinum mold was then placed in the furnace and left to equilibrate for five minutes. The fluid was poured into the mold within the furnace; the mold was then removed from the furnace and held over a hot plate to prevent it from cooling too rapidly. After one minute, the mold was set on the hot plate, and the hot plate was cooled down slowly. When completely cool, the fused glass disk was removed from the mold. The disks were analyzed on the Rigaku XRF spectrometer for seven component oxides: SiO_2, Al_2O_3, CaO, MgO, FeO, Na_2O, and K_2O using standard AGV-1, a USGS (United States Geological Survey) standard.

X-Ray Diffraction Analysis

Portions of the ground and sieved whole rock powders retained from the XRF pressed pellet preparation were placed in Plexiglas containers (2.5 cm. x 2.5 cm. x 0.4 cm.), which have a 2 mm deep hollowed-out compartment that holds the powder. The surface of the powder was then scraped off so that it was level with the top surface of the Plexiglas holder. The Plexiglas container was then placed in the sample holder of Scintag PAD-V automated diffractometer and analyzed from 2° 2-θ to 60° 2-θ at a scanning rate of 3 degrees per minute, using a 0.03 degree chopper increment.

Oriented mounts of the clay fractions of three samples were analyzed from 2° 2-θ to 30° 2-θ at a scanning rate of 3° 2-θ, using a 0.03 degree chopper increment.

Electron Microprobe Elemental Analysis

Polished thin sections of the rock samples were prepared using no water and maintaining a temperature below 60°C. The thin sections were coated with carbon in a vacuum evaporator. Minerals were analyzed with a JEOL 733 electron microprobe using an acceleration potential of 15 KV, a beam current of 2 nanoamps, a beam diameter of 1.5 microns, for a period of 124 seconds per analysis. Minerals were analyzed for SiO_2, Al_2O_3, CaO, MgO, FeO, Na_2O, and K_2O. Analyses were corrected according to standard Bence-Albee procedures. The microprobe is equipped with an energy dispersive spectrometer (EDS), which allows quick, qualitative identification of minerals from their EDS spectra.

Clay Fraction Separation

To obtain the clay fraction of the samples, the dolomite in the samples was dissolved using disodium ethylenediaminetetraacetic acid (EDTA) (Bodine and Fernalld, 1973). In this procedure, powdered and sieved whole rock samples were placed in a stainless steel container and boiled in a 0.25 molar disodium EDTA solution for four hours, or until the dolomite was completely dissolved. The residue was then passed through a filter to separate the insolubles from the fluid. The residue was dried, ground, and sieved (100 mesh), mixed with water, and left overnight. A portion of the dried and sieved powder was retained to obtain a random mount x-ray diffraction (XRD) pattern. The mixture was disaggregated using a sonic dismembrator and the <2 micron fraction was separated by centrifugation (Hauff, 1982). Oriented diffractometer mounts were prepared by the method of Drever (1973).

Analytical Electron Microscopy

A small portion of the <2 micron powder fraction of sample H6B #3 was embedded in Spurrs epoxy and sectioned to thicknesses of less than 900A using a diamond knife on a Reichert-Jung ultramicrotome. The microtomed sections were mounted on a copper grid and examined using a JEOL 2000FX AEM. High-resolution images and selected area diffraction patterns for several microtomed sections were obtained.

Appendix A References

Drever, J.I. 1973. "The Preparation of Oriented Clay Mineral Specimens for X-ray Diffraction Analysis by a Filter-Membrane Peel Technique." *Am. Mineralogist* 58, 533-554.

Hauff, P.L. 1982. "Sample Preparation Procedures for the Analysis of Clay Minerals by X-ray Diffraction." Workshop syllabus, USGS O.F.R. 82-934, 37p.

APPENDIX B:
MODAL MINERALOGICAL CALCULATIONS

Whole Rock Modal Analysis

Modes for the minerals identified by x-ray diffraction (XRD) were determined from the compositional data obtained by x-ray fluorescence spectroscopy (XRF). Based on the compositions of the individual minerals, either ideal or determined by electron microprobe analysis (EMX), a particular element, when present in only one mineral, was used to determine the mode of that mineral. For example, the only phase containing aluminum in these samples is clay and the EMX and XRF compositions of the clay fraction show that the clay fraction has an average of 15% Al_2O_3; thus, the weight percent of clay was calculated using the formula:

$$Clay(wt\%) = Al_2O_3 / 0.15$$

Quartz, since it contains only SiO_2, was determined by:

$$Quartz(wt\%) = SiO_2 - Clay(wt\%) \times 0.46$$

since the average SiO_2 content of the clay fraction is 46%.

The remaining mineral modes were determined by the following formulae:

$$Gypsum(wt\%) = SO_3 / 0.465$$

$$Halite(wt\%) = Na_2O / 1.886$$

$$Dolomite(wt\%) = (CaO - Gypsum \times 0.326) / 0.304$$

or

$$Dolomite(wt\%) = (MgO - Clay \times 0.15) / 0.19$$

$$Calcite\ (wt\%) = (CaO - Dolomite \times 0.304) / 0.56$$

The mineral modes determined by this method result in totals that typically lie between 90% and 100%, which suggests that the method has an accuracy of about + or -10% of the amount present.

Clay Mineral Modal Analysis

Modes for the component of the clay mineral assemblages in these samples were determined by quantitative X-ray diffraction analysis (Reynolds, 1985). Theoretical oriented (glycolated) diffractograms for the individual clay minerals present in the samples were calculated using the NEWMOD program. These were compared with the diffraction patterns of the glycolated mounts for the samples in this study. The following peaks were selected for quantitative analysis:

Corrensite:	d=3.46A
Chlorite (003):	d=4.73A
Illite (002):	d=5.00A
Serpentine (002):	d=3.51A

The integrated areas of the peaks in the sample diffractograms were divided by the corresponding integrated areas of the peaks in the calculated diffractograms for each mineral; the ratios were summed, and the individual ratios were normalized to 100% to obtain the mode for each clay mineral.

Appendix B References

Reynolds, R.C. Jr. 1985. "Principles and Techniques of Quantitative Analysis of Clay Minerals by X-ray Diffraction Methods." *Clay Mineral Identification*, a Short Course. University of Denver, July 15-19, 1985.

FEDERAL AGENCIES

U. S. Department of Energy, (5)
Office of Civilian Radioactive Waste
Management
Attn: Deputy Director, RW-2
Associate Director, RW-10
Office of Program Administration
and Resources Management
Associate Director, RW-20
Office of Facilities Siting
and Development
Associate Director, RW-30
Office of Systems Integration
and Regulations
Associate Director, RW-40
Office of External Relations
and Policy
Forrestal Building
Washington, DC 20585

U. S. Department of Energy (3)
Albuquerque Operations Office
Attn: J. E. Bickel
R. Marquez, Director
Public Affairs Division
P.O. Box 5400
Albuquerque, NM 87185

U. S. Department of Energy
Attn: National Atomic Museum Library
Albuquerque Operations Office
P. O. Box 5400
Albuquerque, NM 87185

U. S. Department of Energy (4)
WIPP Project Office (Carlsbad)
Attn: Vernon Daub
J. A. Mewhinney
P.O. Box 3090
Carlsbad, NM 88221

U. S. Department of Energy
Research & Waste Management Division
Attn: Director
P. O. Box E
Oak Ridge, TN 37831

U.S. Department of Energy
Richland Operations Office
Nuclear Fuel Cycle & Production Division
Attn: R. E. Gerton
P.O. Box 500
Richland, WA 99352

U. S. Department of Energy (1)
Attn: Edward Young
Room E-178
GAO/RCED/GTN
Washington, DC 20545

U. S. Department of Energy (6)
Office of Environmental Restoration
and Waste Management
Attn: Jill Lytle, EM30
Mark Frei, EM-34 (3)
Mark Duff, EM-34
Clyde Frank, EM-50
Washington, DC 20585

U. S. Department of Energy (3)
Office of Environment, Safety and Health
Attn: Ray Pelletier, EH-231
Kathleen Taimi, EH-232
Carol Borgstrom, EH-25
Washington, DC 20585

U. S. Department of Energy
Ecological Research Division, ER-75
Office of Health and Environmental Research
Office of Energy Research
Attn: F. J. Wobber
Washington, DC 20545

U. S. Department of Energy (2)
Idaho Operations Office
Fuel Processing and Waste
Management Division
785 DOE Place
Idaho Falls, ID 83402

U.S. Department of Energy
Savannah River Operations Office
Defense Waste Processing
Facility Project Office
Attn: W. D. Pearson
P.O. Box A
Aiken, SC 29802

U. S. Department of the Interior (5)
Attn: N. Trask (MS 410)
T. Coplen (MS 431)
B. F. Jones (MS 432)
L. N. Plummer (MS 432)
I. J. Winograd (MS 432)
Geological Survey
National Center
Reston, VA 22092

U. S. Department of the Interior
Attn: J. S. McLean
Geological Survey
Box 25046, MS406
Denver, CO 80225

U. S. Department of the Interior
Attn: J. Thomas
Geological Survey
705 N. Plaza Street
Carson City, NV 89701

U. S. Department of the Interior
Attn: Librarian
National Park Service
Carlsbad Caverns National Park
3225 National Parks Highway
Carlsbad, NM 88220

U. S. Environmental Protection Agency (4)
Attn: Ray Clark (2)
Mark Cotton (2)
Office of Radiation Programs (ANR-460)
Washington, DC 20460

U.S. Geological Survey
Branch of Regional Geology
Attn: R. Snyder
MS913, Box 25046
Denver Federal Center
Denver, CO 80225

U.S. Geological Survey
Conservation Division
Attn: W. Melton
P.O. Box 1857
Roswell, NM 88201

U.S. Geological Survey (4)
Water Resources Division
Attn: Kathy Peter (2)
Roger Ferriera
Scott Anderholm
Suite 200
4501 Indian School NE
Albuquerque, NM 87110

U.S. Nuclear Regulatory Commission (8)
Attn: Joseph Bunting, HLEN 4H3 OWFN
Ron Ballard, HLGP 4H3 OWFN
Michael Bell
David Brooks
Tin Mo
Jacob Philip
John Randall
NRC Library
Mail Stop 623SS
Washington, DC 20555

Office of Nuclear Regulatory Research (4)
U. S. Nuclear Regulatory Commission
MS: NL-005
Washington, DC 20555
Attn: G. F. Birchard
L. A. Kovach
T. J. Nicholson
J. D. Randall

Boards

Defense Nuclear Facilities Safety Board
Attn: Dermot Winters
Suite 675
600 E Street, NW
Washington, DC 20004

U. S. Department of Energy
Advisory Committee on Nuclear
Facility Safety
Attn: Merritt E. Langston, AC21
Washington, DC 20585

Nuclear Waste Technical
Review Board (2)
Attn: Dr. Don A. Deere
Dr. Sidney J. S. Parry
Suite 910
1100 Wilson Blvd.
Arlington, VA 22209-2297

Richard Major
Advisory Committee on Nuclear Waste
Nuclear Regulatory Commission
7920 Norfolk Avenue
Bethesda, MD 20814

STATE AGENCIES

Environmental Evaluation Group (3)
Attn: Library
Suite F-2
7007 Wyoming Blvd., N.E.
Albuquerque, NM 87109

New Mexico Bureau of Mines
and Mineral Resources (2)
Attn: F. E. Kottolowski, Director
J. Hawley
Socorro, NM 87801

NM Department of Energy & Minerals
Attn: Librarian
2040 S. Pacheco
Santa Fe, NM 87505

NM Environmental Improvement Division
Attn: Deputy Director
1190 St. Francis Drive
Santa Fe, NM 87503

LABORATORIES/CORPORATIONS

Battelle Pacific Northwest Laboratories (7)
Attn: D. J. Bradley, K6-24
J. Relyea, H4-54
R. E. Westerman, P8-37
K. Krupa, K2-57
H. C. Burkholder, P7-41
L. Pederson, K6-47
J. Serne
Battelle Boulevard
Richland, WA 99352

Geohydrology Associates
Attn: T. E. Kelly
4015 Carlisle Blvd NE
Albquerque, NM 87110

Savannah River Laboratory (6)
Attn: N. Bibler
E. L. Albenisius
M. J. Plodinec
G. G. Wicks
C. Jantzen
J. A. Stone
Aiken, SC 29801

George Dymmel
SAIC
101 Convention Center Dr.
Las Vegas, NV 89109

INTERA Inc. (3)
Attn: G. E. Grisak
J. F. Pickens
A. Haug
Suite #300
6850 Austin Center Blvd.
Austin, TX 78731

INTERA Inc.
Attn: Wayne Stensrud
P.O. Box 2123
Carlsbad, NM 88221

INTERA Inc.
Attn: A. Marsh LaVenue
8100 Mountain Road
Suite #204D
Albuquerque, NM 87110

IT Corporation (3)
Attn: R. F. McKinney
J. Myers
R. Holt
Regional Office - Suite 700
5301 Central Avenue, NE
Albuquerque, NM 87108

IT Corporation (2)
Attn: D. E. Deal
P.O. Box 2078
Carlsbad, NM 88221

Arthur D. Little, Inc. (3)
Attn: C. R. Hadlock
Scot Foster
Philip Rury
Acorn Park
Cambridge, MA 02140-2390

Los Alamos National Laboratory (10)
Attn: A. Meijer
D. Broxton
B. Carlos
D. Eggert
D. Hobart
E. Springer
I. Triay
J. F. Kerrisk
D. T. Vaniman
K. Wolfsberg
P. O. Box 1663
Los Alamos, NM 87545

Lawrence Berkeley Laboratory (3)
Attn: F. Hale
S. L. Phillips
H. Nitsche
University of California
Berkeley, CA 94720

Martin Marietta Energy Systems, Inc.
Attn: C. S. Fore
Ecological Sciences Information Center
Oak Ridge National Laboratory - Bldg. 2001
P. O. Box X
Oak Ridge, TN 37830

Oak Ridge National Laboratory (4)
Attn: J. A. Carter
G. Jacobs
G. H. Jenks
R. Meyer
Box 2009
Oak Ridge, TN 37831

RE/SPEC, Inc.
Attn: W. Coons
P. F. Gnirk
P.O. Box 14984
Albuquerque NM 87191

RE/SPEC, Inc. (7)
Attn: L. L. Van Sambeek
G. Callahan
T. Pfeifle
J. L. Ratigan
P. O. Box 725
Rapid City, SD 57709

Center for Nuclear Waste Regulatory Analysis (6)
Attn: J. L. Russell (3)
W. Murphy
R. Pabalan
Library
Southwest Research Institute
6220 Culebra Road
San Antonio, TX 78228-0510

Environmental Engineering and Science (2)
Attn: J. O. Leckie
S. W. Park
Department of Civil Engineering
Stanford University
Stanford, CA 94305

Science Applications
International Corporation
Attn: Howard R. Pratt,
Senior Vice President
10260 Campus Point Drive
San Diego, CA 92121

Science Applications
International Corporation
Attn: Michael B. Gross
Ass't. Vice President
Suite 1250
160 Spear Street
San Francisco, CA 94105

Serata Geomechanics
Attn: Dr. Shosei Serata
4124 Lackside Drive
Richmond, CA 94806-1941

Systems, Science, and Software (2)
Attn: E. Peterson
P. Lagus
Box 1620
La Jolla, CA 92038

Westinghouse Electric Corporation (7)
Attn: Library
Lamar Trego
W. P. Poirer
W. R. Chiquelin
V. F.Likar
D. J. Moak
R. F. Kehrman
P. O. Box 2078
Carlsbad, NM 88221

Weston Corporation (1)
Attn: David Lechel
Suite 1000
5301 Central Avenue, NE
Albuquerque, NM 87108

UNIVERSITIES

Arizona State University
Attn: L. P. Knauth
Department of Geology
Tempe, AZ 85287-1404

University of Arizona
Attn: J. G. McCray
Department of Nuclear Engineering
Tucson, AZ 85721

Cornell University
Department of Physics
Attn: Dr. R. O. Pohl
Clark Hall
Ithaca, NY 14853

Florida State University (2)
Attn: J. B. Cowart
J. K. Osmond
Department of Geology
Tallahassee, FL 32308

University of Minnesota
Department of Energy and Materials Science
Attn: R. Oriani
151 Amundson Hall
421 Washington Ave SE
Minneapolis, MN 55455

University of New Mexico (3)
Geology Department
Attn: D. G. Brookins
C. J. Yapp
Library
Albuquerque, NM 87131

New Mexico Institute of Mining and Technology (3)
Attn: L. Brandvold
G. W. Gross
F. Phillips
Socorro, NM 87801

Pennsylvania State University
Materials Research Laboratory
Attn: Della Roy
University Park, PA 16802

Princeton University
Department of Civil Engineering
Attn: George Pinder
Princeton, NJ 08540

Texas A&M University
Center of Tectonophysics
College Station, TX 77840

University of Texas at Austin
Attn: Edward C. Bingler
Deputy Director
Texas Bureau of Economic Geology
Austin, TX 78712

Environmental Engineering and Science (2)
Attn: J. O. Leckie
S. W. Park
Department of Civil Engineering
Stanford University
Stanford, CA 94305

INDIVIDUALS

G. O. Bachman
4008 Hannett Avenue NE
Albuquerque, NM 87110

Carol A. Hill
Box 5444A
Route 5
Albuquerque, NM 87123

Harry Legrand
331 Yadkin Drive
Raleigh, NC 27609

Dennis W. Powers
Star Route Box 87
Anthony, TX 79821

Bob E. Watt
1447 45th St.
Los Alamos, NM 87544

LIBRARIES

Thomas Brannigan Library
Attn: Don Dresp, Head Librarian
106 W. Hadley St.
Las Cruces, NM 88001

Hobbs Public Library
Attn: Ms. Marcia Lewis, Librarian
509 N. Ship Street
Hobbs, NM 88248

New Mexico State Library
Attn: Ms. Ingrid Vollenhofer
P.O. Box 1629
Santa Fe, NM 87503

New Mexico Tech
Martin Speere Memorial Library
Campus Street
Socorro, NM 87810

Pannell Library
Attn: Ms. Ruth Hill
New Mexico Junior College
Lovington Highway
Hobbs, NM 88240

WIPP Public Reading Room
Attn: Director
Carlsbad Public Library
101 S. Halagueno St.
Carlsbad, NM 88220

Government Publications Department
General Library
University of New Mexico
Albuquerque, NM 87131

WIPP PEER PANEL

G. Ross Heath, Chairman
College of Ocean & Fishery Sciences
University of Washington
Seattle, WA 98185

Robert J. Budnitz
President, Future Resources Associates, Inc.
Suite 418
2000 Center Street
Berkeley, CA 94704

Thomas A. Cotton
4429 Butterworth Place NW
Washington, DC 20016

Patrick A. Domenico
Geology Department
Texas A&M
College Station, TX 77843-3115

Charles D. Hollister
Dean for Studies
Woods Hole Oceanographic Institute
Woods Hole, MA 02543

Thomas H. Pigford
Department of Nuclear Engineering
4153 Etcheverry Hall
University of California
Berkeley, CA 94270

Benjamin Ross
Disposal Safety Incorporated
Suite 600
1629 K Street NW
Washington, DC 20006

John Mann
Department of Geology
245 Natural History Building
1301 West Green Street
University of Illinois
Urbana, IL 61801

THE SECRETARY'S BLUE RIBBON PANEL ON WIPP

Dr. Thomas Bahr
New Mexico Water Resources Institute
New Mexico State University
Box 3167
Las Cruces, NM 88003-3167

Mr. Leonard Slosky
Slosky and Associates
Suite 1400
Bank Western Tower
1675 Tower
Denver, Colorado 80202

Mr. Newal Squyres
Eberle and Berlin
P. O. Box 1368
Boise, Idaho 83701

Dr. Arthur Kubo
Vice President
BDM International, Inc.
7915 Jones Branch Drive
McLean, VA 22102

Mr. Robert Bishop
Nuclear Management Resources Council
Suite 300
1776 I Street, NW
Washington, DC 20006-2496

NATIONAL ACADEMY OF SCIENCES, WIPP PANEL

Dr. Charles Fairhurst, Chairman
Department of Civil and
Mineral Engineering
University of Minnesota
500 Pillsbury Dr. SE
Minneapolis, MN 55455

Dr. John O. Blomeke
Route 3
Sandy Shore Drive
Lenoir City, TN 37771

Dr. John D. Bredehoeft
Western Region Hydrologist
Water Resources Division
U.S. Geological Survey (M/S 439)
345 Middlefield Road
Menlo Park, CA 94025

Dr. Karl P. Cohen
928 N. California Avenue
Palo Alto, CA 94303

Dr. Fred M. Ernsberger
250 Old Mill Road
Pittsburgh, PA 15238

Dr. Rodney C. Ewing
Department of Geology
University of New Mexico
200 Yale, NE
Albuquerque, NM 87131

B. John Garrick
Pickard, Lowe & Garrick, Inc.
2260 University Drive
Newport Beach, CA 92660

John W. Healy
51 Grand Canyon Drive
Los Alamos, NM 87544

Leonard F. Konikow
U.S. Geological Survey
431 National Center
Reston, VA 22092

Jeremiah O'Driscoll
505 Valley Hill Drive
Atlanta, GA 30350

Dr. D'Arcy A. Shock
233 Virginia
Ponca City, OK 74601

Dr. Christopher G. Whipple
Electric Power Research Institute
3412 Hillview Avenue
Palo Alto, CA 94303

Dr. Peter B. Myers, Staff
Director
National Academy of Sciences
Committee on Radioactive
Waste Management
2101 Constitution Avenue
Washington, DC 20418

Dr. Geraldine Grube
Board on Radioactive
Waste Management
GF462
2101 Constitution Avenue
Washington, DC 20418

Dr. Ina Alterman
Board on Radioactive Waste
Management
GF462
2101 Constitution Avenue
Washington, DC 20418

FOREIGN ADDRESSES

Studiecentrum Voor Kernenergie
Centre D'Energie Nucleaire
Attn: Mr. A. Bonne
SCK/CEN
Boeretang 200
B-2400 Mol
BELGIUM

Atomic Energy of Canada, Ltd. (2)
Whiteshell Research Estab.
Attn: Peter Haywood
John Tait
Pinewa, Manitoba, CANADA
R0E 1L0

Dr. D. K. Mukerjee
Ontario Hydro Research Lab
800 Kipling Avenue
Toronto, Ontario, CANADA
M8Z 5S4

Department of Earth Sciences and
Quaternary Sciences Institute
Attn: T. W. D. Edwards
University of Waterloo
Waterloo, Ontario
CANADA N2L 3Gl

Mr. Francois Chenevier, Director (2)
ANDRA
Route du Panorama Robert Schumann
B.P.38
92266 Fontenay-aux-Roses Cedex
FRANCE

Mr. Jean-Pierre Olivier
OECD Nuclear Energy Agency
Division of Radiation Protection
and Waste Management
38, Boulevard Suchet
75016 Paris, FRANCE

Claude Sombret
Centre D'Etudes Nucleaires
De La Vallee Rhone
CEN/VALRHO
S.D.H.A. BP 171
30205 Bagnols-Sur-Ceze
FRANCE

Bundesministerium fur Forschung und
Technologie
Postfach 200 706
5300 Bonn 2
FEDERAL REPUBLIC OF GERMANY

Bundesanstalt fur Geowissenschaften
und Rohstoffe
Attn: Michael Langer
Postfach 510 153
3000 Hannover 51
FEDERAL REPUBLIC OF GERMANY

Hahn-Meitner-Institut fur Kernforschung
Attn: Werner Lutze
Glienicker Strasse 100
100 Berlin 39
FEDERAL REPUBLIC OF GERMANY

Institut fur Tieflagerung (4)
Attn: K. Kuhn
Theodor-Heuss-Strasse 4
D-3300 Braunschweig
FEDERAL REPUPLIC OF GERMANY

Kernforschug Karlsruhe
Attn: K. D. Closs
Postfach 3640
7500 Karlsruhe
FEDERAL REPUBLIC OF GERMANY

Physikalisch-Technische Bundesanstalt
Attn: Peter Brenneke
Postfach 33 45
D-3300 Braunschweig
FEDERAL REPUBLIC OF GERMANY

Hermann Gies
Institut fur Tieflagerung, Gruppe Geochemie
Gesellschaft fur Strahlen und Umweltforschung mbH
Theodor-Heuss-Strasse 4
D-3300 Braunschweig
FEDERAL REPUBLIC OF GERMANY

British Geological Survey (3)
Hydrogeology Group
Attn: G. Darling
R. A. Downing
R. L. F. Kay
Maclean Building
Crowmarsh Gifford
Wallingford
Oxfordshire OX10 8BB
GREAT BRITAIN

U. K. Atomic Energy Authority (3)
Attn: M. Ivanovich
R. Otlet
A. J. Walker
Centre for Nuclear Applications
Isotope Measurement Laboratory
Harwell
Oxfordshire OX11 ORA
GREAT BRITAIN

D. R. Knowles
British Nuclear Fuels, plc
Risley, Warrington, Cheshire WA3 6AS
1002607 GREAT BRITAIN

Shingo Tashiro
Japan Atomic Energy Research Institute
Tokai-Mura, Ibaraki-Ken
319-11 JAPAN

Netherlands Energy Research Foundation
ECN (2)
Attn: Tuen Deboer, Mgr.
L. H. Vons
3 Westerduinweg
P.O. Box 1
1755 ZG Petten, THE NETHERLANDS

Svensk Karnbransleforsorjning AB
Attn: Fred Karlsson
Project KBS
Karnbranslesakerhet
Box 5864
10248 Stockholm, SWEDEN

SANDIA INTERNAL

400 L. D. Tyler
1510 J. C. Cummings
1512 K. L. Erickson
1520 C. W. Peterson
1521 J. G. Arguello
1521 H. S. Morgan
3141 S. A. Landenberger (5)
3151 Supervisor (3)
3154-1 C. L. Ward, (10) for DOE/OSTI
6000 V. L. Dugan, Acting
6230 R. K. Traeger
6232 W. R. Wawersik
6233 D. J. Borns
6233 J. C. Eichelberger
6233 J. L. Krumhansl
6233 S. J. Lambert
6233 C. L. Stein
6300 T. O. Hunter, Acting
6310 T. E. Blejwas, Acting
6313 L. E. Shephard
6315 F. B. Nimick, Acting
6315 R. J. Glass
6315 M. D. Siegel (5)
6340 W. D. Weart
6340A A. R. Lappin
6340 S. Y. Pickering
6341 R. C. Lincoln
6341 Staff (9)
6341 Sandia WIPP Central Files (10)

6342 D. R. Anderson
6342 Staff (11)
6343 T. M. Schultheis
6343 Staff (2)
6344 E. Gorham
6344 Staff (10)
6345 B. M. Butcher, Acting
6345 Staff (9)
6346 J. R. Tillerson
6346 Staff (7)
8524 J. A. Wackerly (SNLL Library)
9300 J. E. Powell
9310 J. D. Plimpton
9320 M. J. Navratil
9325 L. J. Keck (2)
9330 J. D. Kennedy
9333 O. Burchett
9333 J. W. Mercer
9334 P. D. Seward

*U.S. GOVERNMENT PRINTING OFFICE 1991-0-573-038/44022